Alma Mater Studiorum - Università di Bologna

DOTTORATO DI RICERCA IN

BIOLOGIA CELLULARE E MOLECOLARE

Ciclo 36

Settore Concorsuale: 05/E2 - BIOLOGIA MOLECOLARE

Settore Scientifico Disciplinare: BIO/11 - BIOLOGIA MOLECOLARE

MOLECULAR ENGINEERING OF THE M13 PHAGE FOR TARGETED PHOTODYNAMIC CANCER TREATMENT

Presentata da: Luca Ulfo

Coordinatore Dottorato

Vincenzo Scarlato

Supervisore

Alberto Danielli

Co-supervisore

Matteo Calvaresi

Esame finale anno 2024

Abstract

Photodynamic therapy (PDT) is an emerging strategy in cancer treatment. This thesis focuses on the development and application of targeted PDT using bioengineered phages. The primary objective was to exploit the specificity of phages to target key cancer-related receptors, like EGFR and HER2. These receptors, critical in various malignancies, are overexpressed in many cancers and are often associated with aggressive disease progression and poor prognosis. Selective targeting of EGFR and HER2 offers a promising strategy for therapeutic intervention, with the aim of improving treatment outcomes and reducing side effects.

Initially, the research was carried out using the $M13_{EGFR}$ phage, retargeted via pIII-display of an EGFR-binding peptide, highlighting its potential for EGFR receptor targeting and subsequent PDT applications. When the $M13_{EGFR}$ phage was effectively conjugated with the Rose Bengal photosensitizer (RB), a significant increase in killing efficiency compared to RB alone was observed at pico-molar concentrations of the phage vector. This discovery phase provided insight into the capabilities of phages in the targeted PDT field.

Eventually, a significant advance was the introduction of the $M13_{7D12}$ phage, which was engineered to display the 7D12 nanobody, known for its specificity to the EGFR outer membrane domain. The evolution from peptide-based to nanobody-based targeting led to improved specificity and therapeutic outcomes. To emphasise the translational potential of the developed platform, in vitro assays were performed using a therapeutic laser instead of a led light lamp to achieve selective specific killing with the $M13_{7D12}$ phage. The same laser setting was subsequently used in a in vivo setting in mice. The killing mechanism was consistent with a necrotic mode of cell death. These combined findings further support the therapeutic promise of this bioengineered nanovector.

This research focused also on the interaction of a $M13_{CC}$ phage with colon-cancer cell lines and spheroids. $M13_{CC}$ was shown to deeply penetrate the cancer spheroid core triggering spheroid desegregation and cell death only upon irradiation, underscoring its potential to effectively target cancer cells within a complex tumour microenvironment. Such capabilities are paramount, especially

given the challenges of reaching and targeting cells within densely packed tumour regions. This distinctive behaviour of the $M13_{CC}$ phage, reported for the first time, offers a promising avenue for improved therapeutic interventions in oncology.

In conclusion, this research provides a comprehensive analysis of the efficacy and modularity of the phage platform for targeted PDT. The encouraging results, particularly with the $M13_{7D12}$ phage, together with preliminary findings on a HER2 targeted phage ($M13_{HER2}$), predict a promising horizon for targeted antitumoral approaches mediated by phage nanovectors rigged with PS for PDT.

INTRODUCTION

1. Photodynamic Therapy: A Comprehensive Insight

Photodynamic therapy (PDT) stands as a clinical minimally intrusive modality for cancer treatment. This therapeutic approach hinges on the synergistic interaction of a photosensitizer (PS), light with a specific wavelength, and the presence of in situ molecular oxygen (O_2), culminating in localized photodamage and subsequently instigating cellular killing with an apoptosis/necrosis mechanism.

The operative modality of PDT is dual. Initially, a PS is administered; following a predetermined drug-light interval, this sensitizer is subjected to activation via a light source, harmonized with its absorption spectrum. Given the ambient oxygen, a sequence of biochemical reactions ensues, leading to direct neoplastic cell apoptosis, microvascular impairment, and the onset of localized inflammatory cascades [1].

In comparison with traditional therapeutic treatments, PDT has numerous advantages. It's minimal invasive, has a low cumulative toxicity, precise spatial-temporal modulation, diminished long-term damages, and an enhanced patient life quality expectation. While conventional chemotherapeutics might have systemic toxicity and the ionizing radiation in radiotherapy might inadvertently harm adjacent healthy tissues, the constituents of PDT are typically harmless to biological systems [2]. A salient feature of PDT is its capacity for targeted irradiation, thereby mitigating involuntary damage to healthy tissues. Furthermore, PDT can be integrated with chemotherapy or radiotherapy, either as a complementary modality or as a subsequent post-surgical intervention to mitigate the residual neoplastic load [2].

However, the clinical adoption of PDT in oncology remains circumscribed to superficial lesions or those accessible via endoscopy or surgical means. This constraint predominantly stems from the restricted penetration depth of light within tissues. The interplay of reflection, refraction, scattering, and absorption in

tissues attenuates light intensity, and as tissue depth increases, there's a precipitous decline in effective light dosage, compromising treatment efficacy [3]. A potential solution lies in harnessing near-infrared radiation (NIR), which exhibits diminished absorption and scattering. The spectral range spanning 600 to 1300 nm is recognized as the biological tissue's "optical window," facilitating enhanced light penetration exceeding 6 mm. The predominant therapeutic window for PDT applications is demarcated between 600 and 800 nm [4].

Recent advancements, such as multi-photon lasers, have paved the way for exploring two-photon excitation in PDT. This dual photon absorption proffers two distinct advantages: (i)it facilitates the spatially refined activation of photosensitizers within tissues, and (ii) it engenders an excited state analogous to a one-photon excitation but necessitating double the energy input [5]. Other promising avenues include molecular antennae, serving as energy donor entities for the PS [6], [7], [8], and the utilization of upconverting nanoparticles [9].

1.2 Photophysical and Photochemical Dynamics in Photodynamic Therapy

Upon irradiation with a specific wavelength, a photosensitizer undergoes photon absorption, transitioning from its fundamental state (S^0) to either the primary singlet excited state (S^1) or elevated singlet excited states (S^n). The S^n states undergo swift decay, on the order of femtoseconds, reverting to S^1 via internal conversion (IC). The S^1 excited state, inherently unstable with a nanosecond-scale lifetime, reverts to the ground state S^0 through either (i) radiative (manifested as fluorescence) or (ii) non-radiative processes (heat-dissipation). A tertiary pathway, intersystem crossing (ISC), becomes viable when the energy differential between singlet and triplet states is minimal, facilitating a transition from S^1 to the triplet state T^1 [10]. The T^1 state, characterized by its extended lifetime ranging from microseconds to seconds, can undergo various photophysical and photochemical transformations, including (i) phosphorescent emission and (ii) generation of ROS. These ROS can originate from two distinct mechanisms: a type I electron-transfer mechanism or a type II energy transfer process [11], [12]. In the type I pathway, T^1 interacts directly with cellular biomolecules, procuring a hydrogen atom or electron, forming a radical. This radical subsequently interacts with water or molecular oxygen ($^3O_2$), yielding

various radical oxygen species, including superoxide anion ($O_2^{\bullet-}$), hydroxyl ($^{\bullet}OH$) radicals, and hydrogen peroxide (H_2O_2). Conversely, the type II pathway involves energy transfer from the T^1 state of the PS to $^3O_2$, generating the highly reactive singlet oxygen excited state ($^1O_2$) [13], [14]. Notably, type I and II reactions are interdependent, potentially augmenting each other. Both reactions can transpire concurrently, with their relative contributions modulated by factors intrinsic to the biological environment (e.g., substrates, medium composition, local polarity, oxygen concentration) and the physicochemical attributes of the PS. ROS primarily target electron-rich biomolecules, leading to their irreversible degradation. Among these, •OH stands out as the most deleterious ROS due to its potential to attack a plethora of organic biomolecules, encompassing lipids, carbohydrates, proteins, amino acids, nucleic acids, and DNA [15]. Additionally, $^1O_2$ can inflict irreversible bio tissue damage, culminating in membrane degradation and oxidation. Conversely, while $O_2^{\bullet-}$ is not a potent oxidant, it plays a pivotal role in modulating ROS homeostasis, stress signaling pathways, and serves as a precursor to •OH and $^1O_2$. In essence, the oxidative stress in physiological processes predominantly stems from •OH and $^1O_2$ (Figure1).

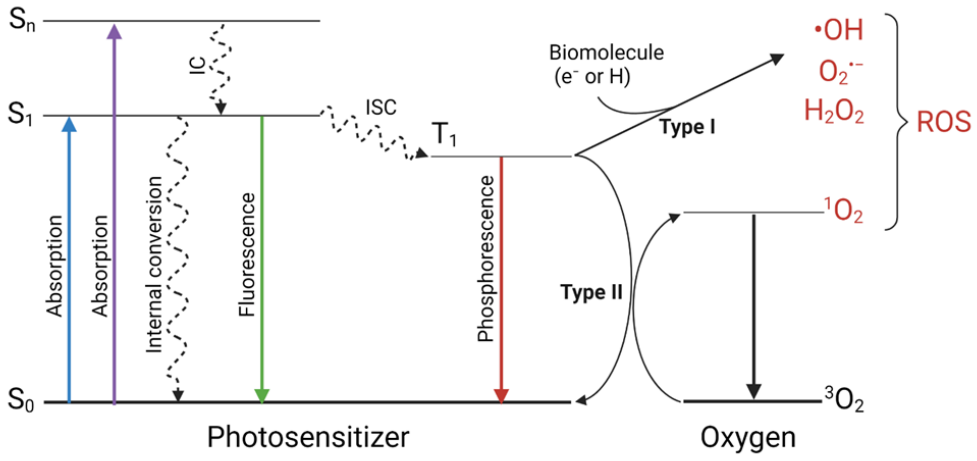

Figure 1 -Jablonski diagram of photosensitizer (PS) excited states showing the photochemical mechanisms operating in photodynamic anticancer therapy[1].

1.3. Mechanistic basis of PDT-Driven Oncolytic Efficacy

The potency of PDT in tumor eradication depends on some interrelated parameters, including the nature, concentration, and intracellular distribution of the PS; the tumour's typology and oxygenation status; and the light's fluence rate and cumulative fluence [16]. Upon optimal activation, PSs generate a neoplastic damage via three synergistic mechanisms: (i) direct cytotoxic impact on neoplastic cells; (ii) disruption of the Neoplastic Vascular Framework; and (iii) inflammatory responses.

- **Direct Cytotoxic Impact on Neoplastic Cells**: ROS, produced from photoactivated photosensitizers (PSs), engage with, and modify a diverse array of biomolecules, encompassing proteins, lipids, nucleic acids, and amino acids. This interaction culminates in irreversible photodamage across various cellular domains. Given the half-life of ROS (ranging from 10 to 320 ns for $^1O_2$), their cellular diffusion is confined to a span of 10–55 nm [17]. Consequently, the intracellular disposition of the activated PS delineates the subcellular region susceptible to photodamage, profoundly influencing cellular outcomes. Predominantly, PDT-driven oncolysis transpires via three pivotal mechanisms: apoptosis, necrosis, and autophagy. Photodamage localized to the mitochondrial outer membrane provokes its permeabilization, thereby activating proapoptotic entities like AIF (apoptotic-inducing factor) or caspase activators (e.g., Smac/DIABLO, cytochrome c), instigating programmed cellular death. Additionally, apoptosis can be triggered when proteases (such as cathepsins) are liberated into the cytosol due to the photodynamic-related lysosomes disruption [18]. In scenarios of excessive cellular trauma or inhibition of apoptotic pathways, the cellular trajectory shifts from apoptosis to necrosis. Necrosis is characterised by the disintegration of organelles, nuclei, and cell membranes, leading to leakage of cellular contents, triggering a robust inflammatory cascade and subsequent tissue damage. Autophagy, or macro-autophagy, represents a regulated lysosomal conduit dedicated to the recycling of compromised proteins or organelles, activated by diverse stressors, inclusive of PDT-induced oxidative stress. While autophagy can lead to cell death, it has also been implicated in enhancing cancer cell resistance to PDT by protecting against photodamage and facilitating the recycling of damaged organelles. [19].

- **Disruption of the Neoplastic Vascular Framework**: Vascularization is pivotal for the proliferation of solid tumors, facilitating the delivery of essential nutrients to malignant cells. This vascularization, often primed by the tumor, is characterized by rapid angiogenesis and incomplete cellular boundaries, leading to the genesis of permeable blood and lymphatic vessels, which augment the delivery and accumulation of PSs to target cells [2]. Empirical evidence underscores the profound impairment of tumor vascularization post-PDT, manifesting as heightened hypoxia and attenuated tumor growth. Specifically, the photoactivation of PSs situated on or proximal to endothelial cells instigates endothelial detachment from the vascular basement membrane. This phenomenon profoundly compromises vascular stability, generating thrombogenic zones marked by platelet aggregation, vasoactive molecule production, and augmented vessel permeability and constriction.
- **Inflammatory responses**: The amplification of both innate and adaptive immune responses significantly augments PDT efficacy, generates a secondary cytotoxic attack on malignant cells and provide durable tumour protection. The localized oxidative stress elicited by PDT, in conjunction with its direct cytotoxicity and vascular impairment, induces an acute inflammatory cascade. Neutrophils, drawn by signaling entities DAMPs (damage-associated molecular patterns) and CDAMPs (cell death-associated molecular patterns), swiftly infiltrate tumors, subsequently recruiting mast cells and macrophages [20]. Macrophages and dendritic cells present tumor-derived antigens to CD4 helper lymphocytes, which subsequently activate CD8 T lymphocytes capable of inducing apoptosis or necrosis in other malignant cells. This ensuing inflammatory process is modulated by cytokines, with IL-1β and IL-6 emerging as pivotal entities for PDT . The immunomodulatory ramifications of PDT are influenced by factors such as the PS variant, anatomical site, and tumor typology. Notably, while most PDT interventions yield an immunostimulatory outcome, epidermal and trans epidermal PDT treatments spanning extensive surfaces correlate with immunosuppression [20].

1.4. Photosensitizers in Photodynamic Therapy: Evolution and Characteristics

For successful integration into photodynamic cancer therapy, a photosensitizer, must adhere to stringent criteria. It is essential that the photosensitiser accumulates predominantly in malignant tissues, while being rapidly cleared from healthy tissues. The singlet excited state should efficiently transition via intersystem crossing, exhibiting a high quantum yield, to form a durable triplet excited state. This facilitates a robust interaction with molecular oxygen and cellular biomolecules. Depending on the biological milieu, the photosensitiser should be able to generate ROS by either of the following mechanisms. To have a high treatment specificity, the PS should exhibit negligible dark toxicity. An absorption coefficient exceeding 700 nm is desirable to activate the PS embedded within deeper tissue structures . The conceptualization of novel photosensitizing agents should prioritize amphiphilicity. A modicum of hydrophilicity is essential to prevent aggregation and facilitate transport to the target tissue, while its lipophilic facet enhances diffusion across cellular membranes. Notably, most PSs predominantly reside extra-nuclearly, thereby reducing the genotoxic and mutagenic implications of PDT .

1. **First-Generation Photosensitizers:** The pioneering generation of PSs predominantly comprised hematoporphyrin derivatives (HpD), conceptualized during the 1970s and early 1980s. Photofrin®, an amalgamation of HpD entities (encompassing monomers, dimers, and oligomers), earned the distinction of being the inaugural clinically authorized PS in 1993, specifically for bladder cancer treatment [21]. A significant limitation of HpD is their suboptimal light absorption within the spectral transparency window, which is pivotal for maximizing tissue penetration during PDT. Their diminished absorption coefficients necessitate the administration of elevated PS dosages to attain a therapeutic response. Initial clinical trials of first-generation PSs were impeded by challenges such as subpar accumulation within malignant

tissues, limited bioavailability, suboptimal pharmacokinetics, and protracted photosensitivity in healthy tissues, including ocular and dermal regions.

2. **Second-Generation Photosensitizers:** In response to these limitations, a second generation of PSs was developed. This cohort predominantly includes porphyrinoid entities like chlorins (e.g., temoporfin, Foscan®), bacteriochlorins, phthalocyanines (e.g., Photosens), and texaphyrins. Concurrently, non-porphyrinoid compounds such as anthraquinones, phenothiazines, xanthenes, and cyanines [22], among others, have garnered clinical attention. Their hallmark is the extended absorption wavelengths, exceeding 600 nm, accompanied by a substantial extinction coefficient [>5 × 104 M^{-1} cm^{-1}]. These PSs exhibit increased ROS production rates, superior tumour cell accumulation and overall enhanced antitumour efficacy compared to their first-generation counterparts. Their accelerated accumulation in malignant cells and rapid clearance from healthy tissues have streamlined the drug-light interval and mitigated post-treatment photosensitivity, making second-generation PSs more clinically viable.
3. **Third-Generation photosensitizers:** Third generation PSs emerged as a strategic effort to synthesise compounds with enhanced tumour targeting and delivery capabilities. This was achieved by conjugating first or second-generation PSs with specific targeting agents. The geometric configuration of the linker requires careful selection to simultaneously preserve the recognition capacity of the targeting moiety and the inherent photodynamic efficacy of the unbound photosensitiser. The selection of the targeting moieties, linker, and PS is paramount, especially since PDT can provoke the re-localization of the PS to alternate subcellular regions or even the extracellular matrix. Such re-localization could stem from the degradation of the photosensitizer, the biomolecular carrier, the chemical linker, or surrounding biomolecules (e.g., lipids or proteins) [23], attributable to the ensuing oxidative stress.

Despite the inherent local selectivity conferred by PS light activation and the benign nature of the excitation light, traditional PDT is not devoid of challenges:

- **Phototoxicity and Photosensitivity**: A significant fraction of PSs exhibit poor selectivity, binding indiscriminately to both malignant and normal cells. This can result in unintended phototoxic effects and photosensitivity, particularly in the skin and eyes. However, when juxtaposed with chemotherapeutics, the localized light activation requisite for photodynamic activity curtails off-target implications.
- **Biodistribution Challenges**: PSs share biodistribution challenges analogous to conventional cancer chemotherapeutics. Direct intravenous administration can culminate in irregular biodistribution, leading to significant drug wastage and suboptimal PS concentrations at the intended target.
- **Hydrophobicity and Formulation Necessities**: The highly hydrophobic nature of many PSs necessitates their administration via intravenous formulations, which often rely on excipients such as Cremophor or ethanol. This can lead to uncontrolled redistribution of photosensitiser molecules, potential hypersensitivity reactions and excipient-induced toxicity, especially during repeated therapeutic sessions.

1.4.4. Receptor-Targeted Photosensitizers: Enhancing Precision in Photodynamic Therapy

To address the inherent challenges associated with traditional PSs, an innovative approach involves conjugating PSs with specific targeting moieties. These moieties are meticulously designed to bind with high specificity to receptors that are overexpressed on the surface of tumor cells, a strategy commonly referred to as active targeting. This receptor-mediated targeting augments the internalization of the PS at the desired tumor site, thereby substantially mitigating off-target interactions and potential side effects. When administered systemically, these receptor-targeted PSs exhibit a pronounced affinity for malignant cells while demonstrating minimal interaction with healthy tissues. Such specificity not only amplifies the therapeutic efficacy of PDT but

also holds significant clinical implications. By enhancing tumor-specific accumulation, the systemic toxicity associated with PSs is markedly reduced, allowing for the administration of optimal therapeutic dosages essential for effective photodynamic activation. Furthermore, the strategic conjugation with biologically relevant targeting agents inherently enhances the solubility profile of the photosensitizer. This obviates the need for additional formulation agents, streamlining the therapeutic regimen and potentially reducing associated complications.

2. EGFR

The identification of specific surface receptors and endogenous signaling molecules that are uniquely expressed or activated in tumor cells offers a promising avenue for the advancement of targeted cancer therapies. Such targeted approaches significantly reduce the potential side effects commonly associated with non-specific treatments [24]. Among the myriad of identified onco-targets, the Epidermal Growth Factor Receptor (EGFR) family, a subset of tyrosine kinase receptors, stands out due to its frequent amplification, overexpression, and functional gain observed across a diverse range of tumors.

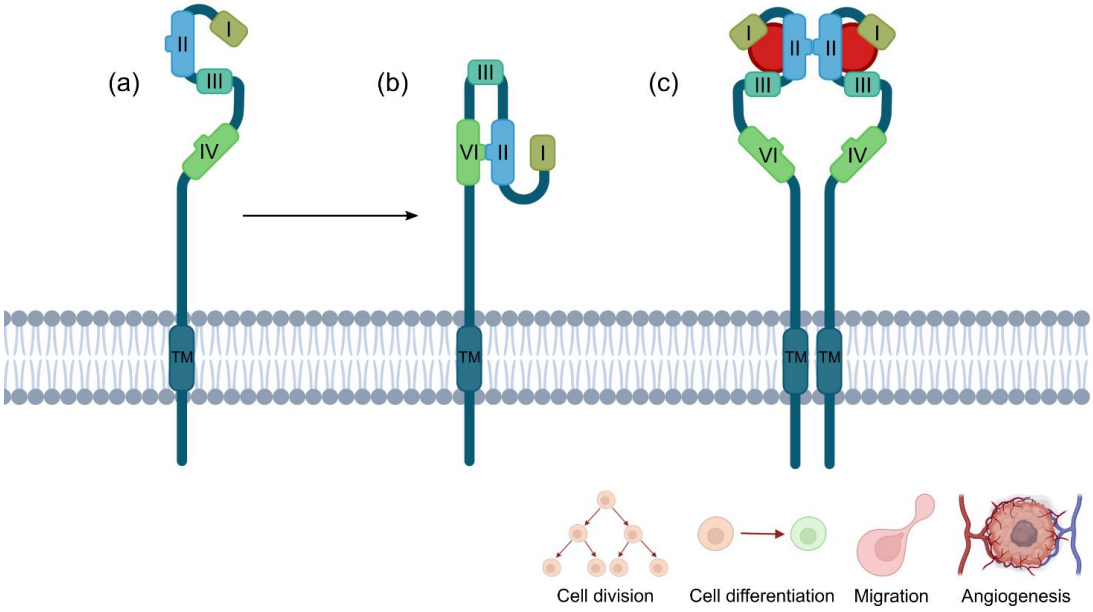

Figure 2 - EGFR structure and conformation: (a) open conformation (active) and (b) closed conformation(inactive); (c) when a ligand binds to EGFR, it promotes the pairing of EGFR molecules, triggering a series of cellular responses. This leads to the promotion of cell growth, differentiation, movement, and blood vessel formation. Created using BioRender.com.

2.1. EGFR Biology and Its Implications in Cancer

EGFR, also denoted as ERBB1 or HER1, is a transmembrane tyrosine kinase receptor that plays pivotal roles in regulating epithelial cell functions including growth, differentiation, and motility. It is a member of the ErbB family of receptor tyrosine kinases, which also encompasses HER2 (ERBB2), HER3 (ERBB3), and HER4 (ERBB4) [25]. The EGFR gene, responsible for encoding this receptor, is situated on the p-arm of chromosome 7, translating into a 170 kDa transmembrane glycoprotein consisting of 1186 amino acids. Notably, aberrations such as gene amplification, mutations, deletions, or other alterations leading to increased EGFR expression or gain-of-function are prevalent in various human malignancies, correlating with poor clinical outcomes. Such overexpression has been documented in cancers of the colorectal, lung, breast, ovarian, cervical, bladder, esophageal, stomach, brain, neck, and endometrial regions [26].

The extracellular domain of EGFR, spanning residues 25–641, comprises four distinct subdomains (I-IV). These can adopt either an active (open) or inactive (closed) conformation. Subdomains I and III, which share structural similarities, are crucial for EGF binding, while subdomains II and IV, rich in cysteine residues, facilitate receptor dimerization [27]. The inactive state is characterized by interactions between subdomains II and IV, inhibiting ligand binding. Conversely, in its active state, EGFR adopts a C-shaped conformation, making subdomains I and III accessible for EGF binding [28]. This binding instigates structural changes in the receptor, promoting homodimerization. Detailed structural analyses have elucidated the specific interactions between EGF and EGFR subdomains. The intracellular segment of EGFR, covering residues 669–1210, encompasses a juxtamembrane segment, a tyrosine kinase domain, and a C-terminal tail. The dimerization of the extracellular domains facilitates the proximity of the intracellular domains, allowing the formation of an asymmetric kinase domain dimer, which is critical for activation and subsequent signalling[29]. This activation cascade culminates in the recruitment of signaling proteins, initiating pathways governing cell proliferation, survival, apoptosis, migration, angiogenesis, and differentiation [29].

Regulation of EGFR activity is achieved through three primary mechanisms that attenuate its signaling by removing the receptor from the cell membrane: clathrin-mediated endocytosis, proteasome degradation, and clustering-induced internalization. In the predominant clathrin-mediated pathway, EGFR undergoes internalization into clathrin-coated vesicles, which subsequently fuse with early endosomes. Depending on the presence or absence of ligands, these receptors either recycle to the cell surface or are directed to lysosomes for degradation [30]. The proteasome pathway involves the E3 ligase Cbl and adaptor protein Grb2, which recognize phosphorylated tyrosine residues on EGFR, leading to its polyubiquitination and subsequent degradation. An alternative internalization mechanism is driven by the dimerization motif in the transmembrane domain. Intriguingly, activated EGFR can evade degradation, either recycling to the plasma membrane or localizing to cellular organelles like mitochondria and nuclei. Within these organelles, EGFR assumes novel roles, influencing transcriptional regulation, DNA repair, mitochondrial dynamics, and ATP production [31]. Such unconventional localizations of EGFR, particularly in the nucleus and mitochondria, have been linked to adverse clinical outcomes in several cancers, including lung, ovarian, breast, and oropharyngeal malignancies [32].

2.2. Strategies for EGFR-Targeted Cancer Therapies

The modulation or suppression of aberrant EGFR activity has been empirically proven to exert profound antitumor effects. The initial therapeutic approach, employing monoclonal antibodies, was swiftly succeeded by the inhibition of receptor kinase signaling using small molecules. This laid the foundation for the emergence of numerous nanobiotechnological interventions, encompassing peptides, aptamers, single-chain antibodies (scFv), single-domain antibodies (nanobodies), and other non-immunoglobulin structures such as DARPins and Affibodies as targeting agents.

In addition, by harnessing the patient's own immune system, tumour proliferation and metastasis have been significantly reduced. Cancer immunotherapies work

by neutralising the immunosuppressive proteins produced by tumour cells and stimulating cellular immune responses against these malignant cells. In this context, the combined use of nanoparticle delivery systems with cancer immunotherapy is gaining interest. This combination is anticipated to enhance selective cytotoxicity by amalgamating novel ablation techniques with the requisite humoral and cellular immune responses for tumor elimination [33].

Emerging research underscores the potential of crafting specialized tools for the selective killing of cancer cells by merging genuine EGFR-targeting agents with light-sensitive PDT agents or nanoparticles. These nanobiotechnological constructs offer a potent dual-action therapy, leveraging the targeting capability of the moieties and the precision of localized irradiation, thereby minimizing unintended harm to normal tissues. Consequently, EGFR-focused PDT methodologies present significant promise for clinical translation.

2.3. EGFR-Directed Photodynamic Therapy (PDT)

Various validated agents targeting EGFR can be employed to selectively deliver PSs for PDT. Broadly, there are two predominant methods for achieving EGFR-targeted PSs. The first involves conjugating primary or secondary generation PSs to biomolecules or ligands possessing EGFR-targeting capabilities. The alternative approach utilizes nanocarriers adorned with EGFR-targeting agents to transport PSs.

With the first method, the intricate architecture and reduced stability of the biomolecules complicate the synthesis and purification of PS conjugates. More critically, the inherent recognition capabilities of the targeting agents can be altered or completely modified during the conjugation process. This restriction limits the number of PSs that can be attached to a single targeting moiety. For the latter approach, besides the synthetic challenges, the procedures for modifying the surface with targeting agents can significantly alter the nanocarrier's properties, including its size, charge, morphology, stability, drug capacity, and release dynamics.

Theoretically, the greater the multivalency of the compounds directed towards EGFR, the more pronounced the generation of cytotoxic ROS upon light

exposure. The EGFR-mediated intracellular transport of the sensitizers to specific cellular compartments can influence the mode of cell death (e.g., apoptotic versus necrotic), potentially affecting the overall treatment efficacy and patient tolerance. Notably, the physicochemical properties and dimensions of the targeting component and the specific EGFR domain it recognizes can influence factors such as tissue distribution, penetration depth, systemic clearance, cellular uptake, achievable multivalency, and interactions with the immune system.

3. HER2

HER2, also known as ERBB2 or Neu, is a transmembrane tyrosine kinase receptor that plays a central role in the regulation of epithelial cell functions, including growth, differentiation, and motility. It is a member of the ErbB family of receptor tyrosine kinases, which also includes EGFR (ERBB1), HER3 (ERBB3) and HER4 (ERBB4). The HER2 gene is located on the long arm of chromosome 17 and encodes a 185 kDa transmembrane glycoprotein of 1255 amino acids. Notably, aberrations such as gene amplification, mutations, deletions, or other alterations leading to increased HER2 expression or gain-of-function are prevalent in various human malignancies, correlating with poor clinical outcomes. Such overexpression has been documented in cancers of the breast, ovarian, gastric, colorectal, lung, and endometrial regions[34].

[35], [36] Within the extensive landscape of oncological molecular research, HER2 receptor has been a focal point, particularly in breast cancer. This concentrated attention was due by findings that HER2 plays a pivot role in mammary carcinogenesis, as evidenced by in vitro and in vivo [37] studies. It is noteworthy to mention that the genomic amplification or transcriptional overexpression of the HER2 gene manifests in approximately 15–30% of breast neoplasms. As the depth of our understanding of HER2 molecular biology has augmented, it has become evident that aberrant HER2 expression is not confined to breast malignancies. It also manifests in a spectrum of other neoplastic conditions, encompassing gastric, ovarian, uterine serous endometrial carcinoma, colonic, vesical, pulmonary, cervical, oropharyngeal, and esophageal

cancers. Beyond its intrinsic role in oncogenic pathways, HER2 has been subjected to rigorous scientific scrutiny as a prospective therapeutic target.

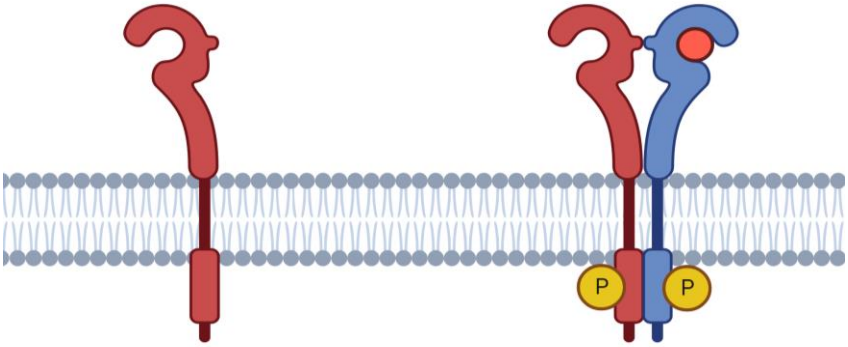

Figure 3 – HER2 structure and conformation

3.2 HER2 overexpression in breast cancer

HER2 (Human Epidermal Growth Factor Receptor 2) overexpression is observed in approximately 15–30% of invasive breast neoplasms, bearing both prognostic and predictive ramifications. It has been documented that breast malignancies can exhibit between 25–50 copies of the HER2 gene, leading to a 40–100-fold surge in HER2 protein levels, culminating in the expression of approximately 2 million receptors on the tumor cell surface [19]. Intriguingly, even estrogen, through the extranuclear, nongenomic activity of the estrogen receptor (ER), has been identified to potentiate HER2 signaling pathways. A truncated form of HER2, called p95, which lacks the extracellular domain, has been identified in certain breast cancers. This constitutively active form confers resistance to trastuzumab, which requires the extracellular domain of HER2 for effective binding. Consequently, p95 remains elusive to antibodies targeting the extracellular domain. [38], [39].

HER2 amplification has been clearly associated with reduced disease-free survival and overall survival in breast cancer patients. Accumulating evidence posits that HER2 amplification is an incipient event in breast tumorigenesis. Approximately 50% of ductal carcinoma in situ cases, which have not yet presented invasive disease characteristics, display amplification of the HER2 gene. This genetic aberration persists as the tumor progresses through stages of

invasive disease, lymph node metastasis, and ultimately to distant metastases. Moreover, breast cancers with HER2 amplification are notably more responsive to certain cytotoxic chemotherapy drugs and tend to show resistance to some hormonal treatments. There is also a significantly increased tendency for these cancers to metastasize to the brain.

3.3 HER2 targeting.

Within the domain of cancer molecular biology and therapeutics, the Human Epidermal Growth Factor Receptor 2 (HER2) has been identified as a critical molecular target, especially in the context of breast and gastric/gastroesophageal neoplasms. Furthermore, the potential of targeting HER2 in ovarian neoplasms is currently under rigorous investigation.

- **Trastuzumab**: This monoclonal antibody specifically binds to the extracellular domain IV of the HER2 receptor.
- **Lapatinib**: an oral dual tyrosine kinase inhibitor, inhibits the signalling pathways of both HER2 and EGFR.
- **Pertuzumab**: This humanized monoclonal antibody operates by obstructing the activation of the HER2 receptor, preventing its dimerization.
- **Ado-Trastuzumab Emtansine**: This innovative antibody-drug conjugate is designed to target HER2 overexpressing cells.
- **Neratinib**: As an oral tyrosine kinase inhibitor, neratinib targets both HER2 and EGFR.
- **Afatinib**: This oral therapeutic agent inhibits EGFR/HER1, HER2, and HER4. [40].

4. Bacteriophages

Bacteriophages, commonly known as 'phages', represent a specific category of viruses that exclusively target and proliferate within bacterial and archaeal hosts.

The initial identification of these entities can be traced back to the pioneering work of Frederick Twort who, over a century ago, observed peculiar disturbances in the growth of bacterial cultures. These perturbations were characterised by the appearance of unique "glassy and transparent" plaques. With scientific caution, Twort postulated that such growth perturbations, combined with the observed plaques, could potentially indicate the existence of "ultra-microscopic viruses". Concurrently, Felix d'Herelle, a renowned Canadian microbiologist, was conducting similar research. Unlike Twort, d'Herelle promptly deduced the viral nature of these entities, in particular their preference for bacterial hosts, and subsequently coined the term 'bacteriophages'. Subsequent studies of these microorganisms revealed a profound revelation: bacteriophages may be the most abundant life forms on Earth. Current scientific approximations indicate their sheer ubiquity, suggesting a potential ratio of 1-10 phages per bacteria cell, culminating in an estimated total of nearly 10^{31} virions on earth[41].

Phages are characterised by great diversity, not only in their morphological characteristics but also at the genomic level, which includes both DNA and RNA genomes. This heterogeneity is further reflected in their infection strategies and life cycles, which can be delineated as either lytic or lysogenic. Genomic analyses reveal a wide range in their genome sizes, spanning from a mere few thousand base pairs to an extensive half a million base pairs. A salient challenge encountered in phage research pertains to the lack of universally conserved genes across diverse phages, complicating their taxonomic categorization endeavours [41].

4.1 The M13 Bacteriophage: A Detailed Examination

The M13 phage, a member of the filamentous phage family *Inoviridae*, is a fascinating object of study. Its genetic architecture comprises a circular single-stranded DNA (ssDNA) genome encapsulated within a protein cylinder, 7 nm wide in diameter, and between 900 to 2000 nm in length. Notably, the M13 phage exhibits specificity towards *E. coli* strains harboring the F-plasmid, a genetic element facilitating bacterial conjugation via the F-pilus. The infection mechanism employed by the M13 phage is a perfect example of the biological precision. The

phage engages with the F-pilus, and as this structure retracts, facilitates the phage's entry into the bacterial cell.

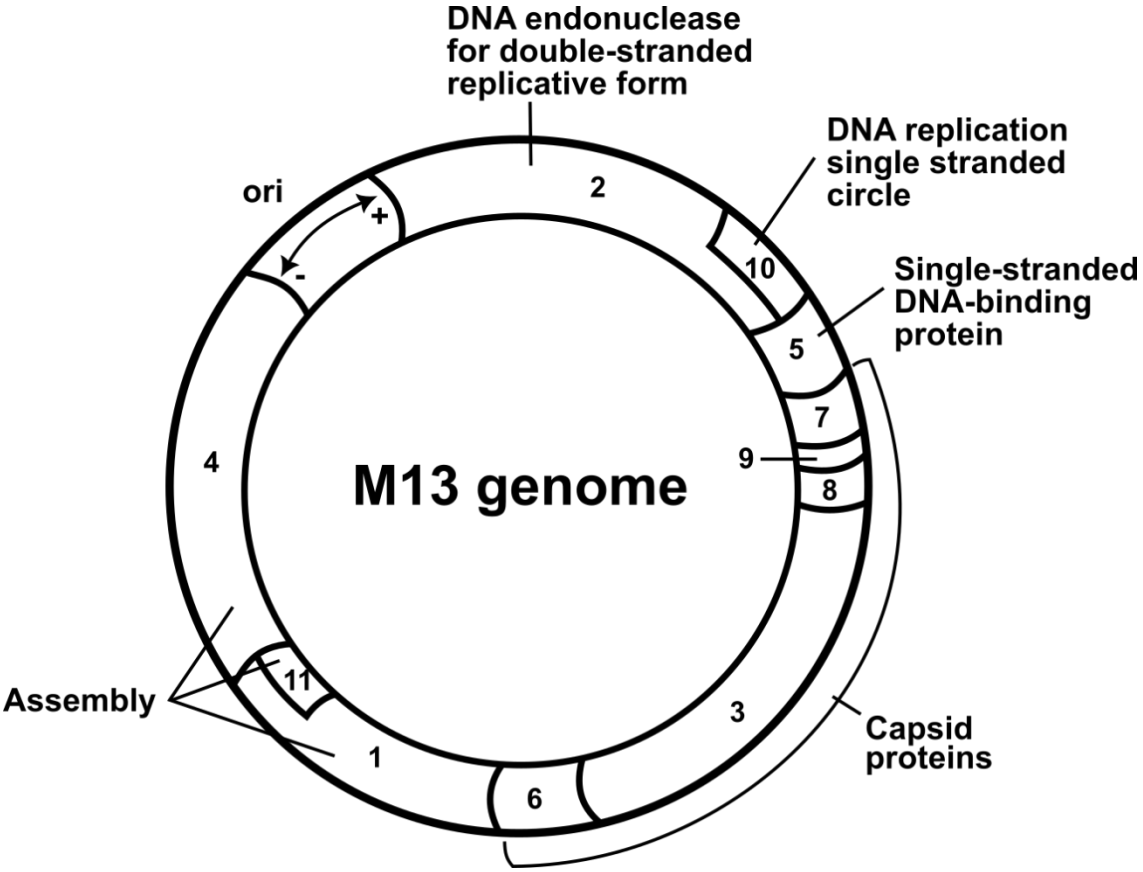

Figure 4 - Diagrammatic representation of the M13 bacteriophage genome detailing the replication and assembly pathways. The origin of replication (ori) is bidirectional, enabling the generation of both plus (+) and minus (-) DNA strands, which are essential for genome propagation and phage morphogenesis. Specific genes, such as 7, 9, 8, 3, and 6, are responsible for coding the capsid proteins, while genes 1, 11, and 4 play crucial roles in the assembly process.

The M13 phage genome is 6.5 Kbp long and has only 11 protein coding genes. These genes can be functionally classified based on their roles in capsid protein synthesis, genome replication, and phage particle assembly at the bacterial membrane. A noteworthy aspect of the M13 genome is an intergenic region devoid of coding potential, which encompasses replication sites for both the positive (+) and negative (-) DNA strands (Figure 4). This region also accommodates a specialized packaging signal, instrumental in initiating phage particle assembly.

The M13 phage uses the host's replication apparatus to amplify its (+) strand, while the (-) strand serves a transcriptional purpose in the bacterial cytoplasm for the synthesis of essential proteins. Among the encoded genes, genes II, V, and X are particularly significant, encoding cytoplasmic proteins pivotal to phage DNA

replication. Post-infection, the ssDNA undergoes a transformation into a supercoiled double-stranded DNA (dsDNA) replicative form, termed RF-DNA, mediated by the host's enzymatic systems.

Genes III, VI, VII, VIII, and IX are dedicated to the synthesis of capsid proteins. Upon synthesis, these proteins localize to the bacterial membrane's cytoplasmic side, poised for their role in assembling subsequent phage generations. The pVIII protein, the major capsid constituent, requires an estimated 2700 molecules for a complete capsid formation. The pIII protein (or minor capsid protein) matures to encompass 406 residues, with a significant segment projecting into the bacterial cell's periplasmic space. The precise mechanisms dictating the membrane positioning of proteins pVI, pVII, and pIX remain unknown[42].

In conclusion, genes I, IV, and XI encode proteins essential for viral particle assembly, albeit not being capsid components. The pI protein intriguingly lacks an N-terminal addressing region but appears to associate with the bacterial membrane, potentially forming channels. The pXI protein exhibits structural similarities with the C-terminal domain of pI and is integral to the phage assembly process. Conversely, the pIV protein integrates into the bacterial Outer Membrane (OM), hinting at its potential role in facilitating the extrusion of the mature viral particle from its bacterial host.

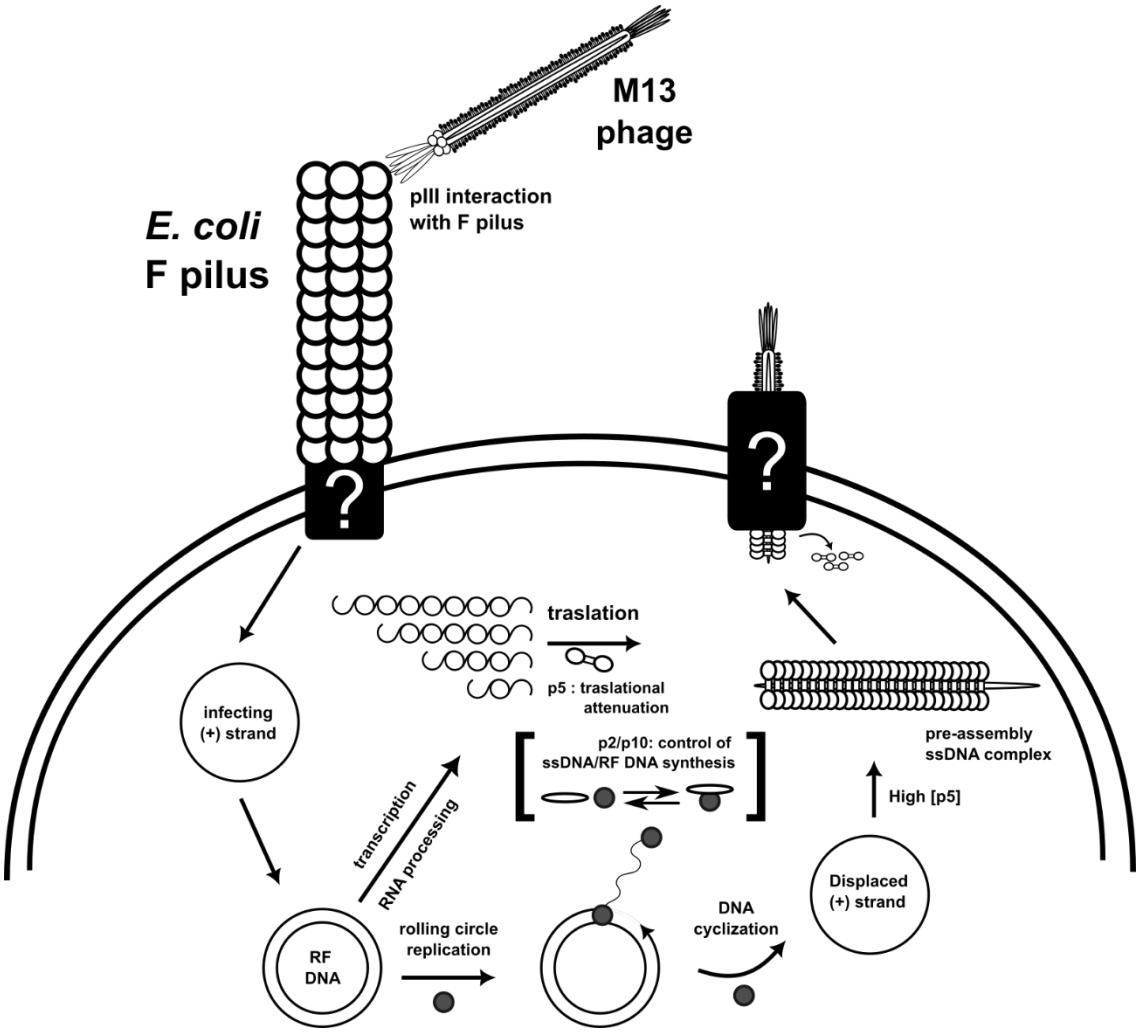

Figure 5 -Diagrammatic representation of the M13 phage infection cycle in E. coli, highlighting the interaction between the phage's protein III (pIII) and the F pilus of the bacterial host. The cycle starts with the infecting single-stranded DNA (+ strand) which is then translated and replicated through a rolling circle mechanism, producing replicative form (RF) DNA. Control of ssDNA/RF DNA synthesis is regulated by proteins p2/p10. High levels of protein p5 lead to pre-assembly of the ssDNA complex. The final stage is the displacement of the (+) strand, which can then initiate a new infection cycle.

4.2 M13 Phage's Infection Mechanism and Life Cycle

The M13 phage employs a sophisticated two-stage infection mechanism, characterized by precision and coordination:

- **Initial Engagement and F-pilus Retraction**: The onset of the infection process is marked by the engagement of the terminal region of the pIII protein with the tip of the F-pilus. This engagement initiates a phenomenon postulated to be the depolymerisation of pilin subunits. As a result, the F-pilus undergoes retraction, pulling it proximal to the bacterial membrane surface.

- **Membrane Assimilation and DNA Transfer**: The following stage involves the incorporation of the pVIII protein, possibly in conjunction with other capsid proteins, into the inner membrane (IM) of the bacterium. This integration is followed by the transfer of phage DNA into the bacterial cytoplasm. This complex transfer process depends on the products of bacterial genes known as tolQRA. Any mutations within these genes confer resistance to this phase of infection, resulting in pilus retraction without actual viral invasion. The tolQRA proteins are strategically positioned at the IM. Notably, while tolQ makes three membrane crossings, both tolR and tolA make a single membrane crossing via an N-terminal domain. Recent research suggests that the transmembrane domains of these proteins may interact with each other[43].

The infection cascade is activated when the N2 domain of the pIII protein engages with the F-pilus tip. This engagement instigates pilus retraction, facilitating the pIII protein's access to the periplasmic domain. Within this space, the N1 domain of pIII establishes an interface with the D3 domain of TolA. The subsequent processes, however, remain unclear. As indicated above, the pVIII protein is postulated to be the main mediator of phage DNA entry into the bacterial cytoplasm. The precise functionalities and implications of tolQ and tolR within this framework remain speculative, but it is hypothesised that they provide a conduit for DNA transfer. Following successful DNA transfer, the phage's single-stranded DNA (ssDNA), now located in the bacterial cytoplasm, is rapidly converted to its double-stranded DNA (dsDNA) RF configuration. The negative (-) strand of this DNA acts as a transcription template, which then orchestrates the synthesis of the phage's 11 proteins. Of these, the pII protein is particularly important because of its central role in replication [44]. RF DNA synthesis continues until a sufficient concentration of pV is reached [45]. This protein associates with the positive (+) DNA strand, inhibiting its transformation into RF DNA, leading to the genesis of protein-DNA assemblages termed pV-DNA. This association is facilitated at the DNA's packaging signal, postulated to be the phage assembly's initiation cue. After this, proteins pVII and pIX engage with the PS, and the DNA commences its emergence from the membrane via a channel constituted by proteins pI and pIV. During this phase, the bond between the pV protein and the DNA is

supplanted by pVIII at its C-terminal domain. The encapsulation sequence culminates in the integration of the terminal proteins, pIII and pVI, which complete the phage assembly process (Figure 5).

4.3Phage Display: An Advanced Molecular Technique and Its Variants

Introduced in 1985, phage display is a pioneering technique in molecular biology that focuses on the integration of a specific coding sequence into the phage genome. This integration leads to the production of a modified capsid protein, which is enhanced by the added sequence of interest. Typically, this sequence is attached to the N-terminus of the gene encoding one of the capsid proteins. While a wide variety of phage proteins can be used for this purpose, the pIII and pVIII proteins are favoured. The phage display methodology has been pivotal in the generation of extensive libraries encompassing proteins, peptides, and antibodies. From these vast repositories, entities with optimal binding to specific targets are identified by a technique called 'panning'. Over the decades, the phage display approach has undergone considerable refinement, with variations often depending on the vector chosen. Our research has focused primarily on displays using pIII and pVIII, with a strong emphasis on pIII display [46].

Diverse Modalities of Phage Display (Figure 6):

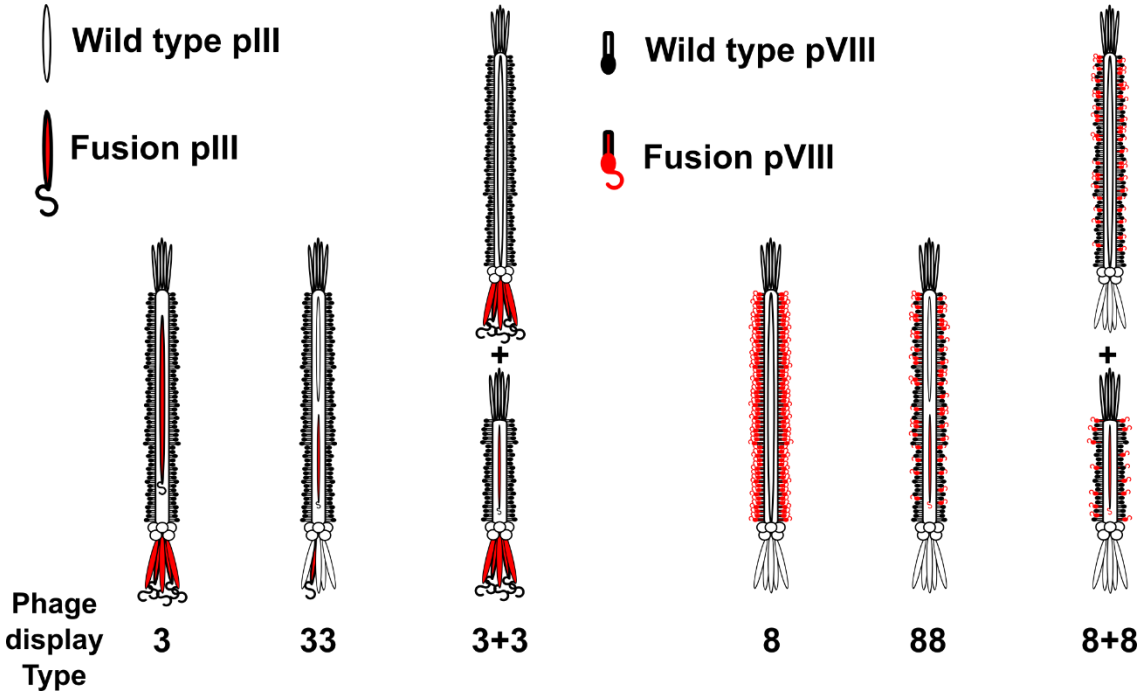

Figure 6 -Visual summary of phage display techniques indicating different valencies of fusion protein presentation. The display on pIII protein can be in the 3, 33, or 3+3 formats, while on pVIII protein, it can be in the 8, 88, or 8+8 formats. These numbers reflect the multiplicity of the fusion proteins on the phage surface.

- **Type 3 and Type 8 Display**: This simple system uses the genome of a wild-type phage as a vector for delivery. The gene to be displayed is modified by attaching the desired genetic sequence to its N-terminus. Singular genes for each protein ensure that every instance of the modified protein has the desired sequence. However, this method of display is subject to constraints on the length of the sequence appended, which is limited to approximately 30 amino acids for pIII display and only 5-8 amino acids for pVIII display.

- **Type 33 and 88 Display:** This variant introduces a second copy of either gene III or gene VIII, which is modified to prevent recombination. This architecture facilitates the integration of extended sequences as only a subset of the capsid proteins in the resulting phage are modified (approximately 1-10% for pVIII) [47].

- **Type 3+3 and 8+8 Display**: This sophisticated display modality, which we predominantly use, integrates a secondary vector, referred to as a

'phagemid', in tandem with the vector containing the complete phage genome. The phagemid works in two ways: it replicates as a bacterial plasmid thanks to a bacterial ORI but is also packed as a phage genome thanks to the phage f1 ORI. Genomically, it contains only the gene intended for display, to which the sequence of interest is attached at the N-terminus. Bacteria harbouring the phagemid are then infected (or possibly co-transformed) by a 'helper' phage that encodes all the necessary phage proteins. In the case of pIII display, the helper presents a truncated version of pIII consisting only of the CT domain. Typically, all helper plasmids have a modified pII or phage ORI, ensuring that their encapsulation is less privileged compared to the phagemid genome. This display modality offers the advantage of easy peptide sequence modification via elementary cloning at the phagemid level. In certain configurations, the expression of the protein display is controlled by the *lac* promoter, making its expression inducible by IPTG or P_{Rham} promoter inducible with rhamnose. This system also supports the display of elongated peptides or sequences. If required, bacteria can be co-transformed with dual phagemids for simultaneous pIII and pVIII display. Upon infection with the helper phage, this culminates in an 'orthogonal display' where both pIII and pVIII are simultaneously modified on an identical virion.

Predominantly, the pIII display is harnessed for phage targeting, and as such, it is fused with targeting peptides, scFv antibodies, nanobodies, or other targeting moieties.

5. Nanobodies

Nanobodies, also known as VHH antibodies, are a unique subclass of antibodies devoid of the light chains that are characteristically present in conventional immunoglobulins. First identified in 1990, they were observed in members of the

Camelidae family, which synthesize them in conjunction with the traditional antibodies. Structurally, nanobodies consist only of the heavy chain, leading to their initial nomenclature as HcAbs (heavy-chain-only antibodies).

Biochemically, nanobodies are characterised by increased specificity and affinity for antigens. Empirical studies have shown that they often outperform conventional antibodies in terms of stability under various stress conditions, including elevated temperatures, proteolytic environments, high pressures, and acidic pH. This enhanced resistance is thought to be a consequence of their compact molecular structure, with a molecular weight of approximately 15 kDa. In vivo, their small size facilitates superior tissue penetration. However, this same attribute can be a limitation, as molecules below the renal filtration threshold are rapidly excreted. To mitigate this, strategies such as PEGylation or conjugation to the Fc domain of conventional antibodies have been explored to augment their in vivo half-life [48].

Immunologically, despite their non-human origin, nanobodies induce a subdued immune response in human hosts. This reduced immunogenicity can be attributed to the significant sequence homology they share with the human VH gene family III. To further attenuate potential immunogenicity, certain nanobody scaffolds have been subjected to "humanization" processes [49].

From a biotechnological perspective, the hydrophilic nature and compact size of nanobodies make them amenable to expression in microbial systems such as *E. coli, P. pastoris*, and *S. cerevisiae* [49]. Their genetic encoding by a singular gene of approximately 360 base pairs make them particularly suitable for phage display techniques.

Aim of the thesis

Cancer refers to diseases characterised by uncontrolled cell proliferaiton leading to tumour formation and potential tissue invasion. These conditions can result from a variety of factors, including genetic mutations, chemical exposures, and individual behaviours. With over 100 types identified, cancer cells can arise from any tissue in the body. The defining characteristic of these cells is deregulated proliferation due to accumulated cellular abnormalities. This can lead to invasion of adjacent tissues and, in advanced stages, metastasis to distant organs, particularly the breast, lungs, prostate and skin. Current treatments include surgery, chemotherapy, radiotherapy, targeted therapies, and immunotherapy. The choice of treatment is influenced by the cancer's type, stage, and specific cellular characteristics. Continuous research seeks to refine and introduce novel therapeutic approaches. Targeted therapy uses drugs to target specific genes and proteins that support cancer cell growth. However, it faces challenges such as the development of resistance in cancer cells, problems with specificity due to mutations, side effects such as rash and hypertension, high costs and limited applicability to certain cancers. In this context of alternatives to traditional cancer treatments, PDT is emerging. PDT is a novel cancer treatment modality that relies on the interaction of a photosensitiser, specific wavelength light and molecular oxygen to induce targeted cellular damage. Compared to traditional methods, PDT offers reduced invasiveness, precise modulation, and minimised long-term damage. However, its application is limited by the depth of light penetration into the tissue and the selective accumulation of the drug itself. Bacteriophages, or 'phages', are viruses that infect bacteria and archaea. The M13 phage, which belongs to the filamentous phage family, is particularly interesting for the ease of genetic manipulation and the straightforward display of proteins on its capsid (as witnessed by many phage display techniques). The latter, involves the integration of specific coding sequences into the M13 phage genome, resulting in modified capsid proteins.

In this thesis, we have integrated PDT, targeted therapy, and phage display techniques to develop a phage-based nanoplatform. This platform is designed to

target overexpressed receptors associated with poor cancer prognosis, overcoming the technical challenges of previous methods. PSs were chemically conjugated to the phage capsid protein, using its structure as a scaffold. By genetically modifying the M13 DNA or specific phagemids for phage display, targeting elements such as nanobodies or peptides were displayed on the tip of the phage virion, allowing specific targeting of cancer cells. These modified phages can efficiently deliver a variety of PSs to cancer cells. When irradiated at the appropriate wavelength, the PSs are activated, facilitating targeted cell destruction, like pulling the trigger after ensuring precise targeting of the cellular targets.

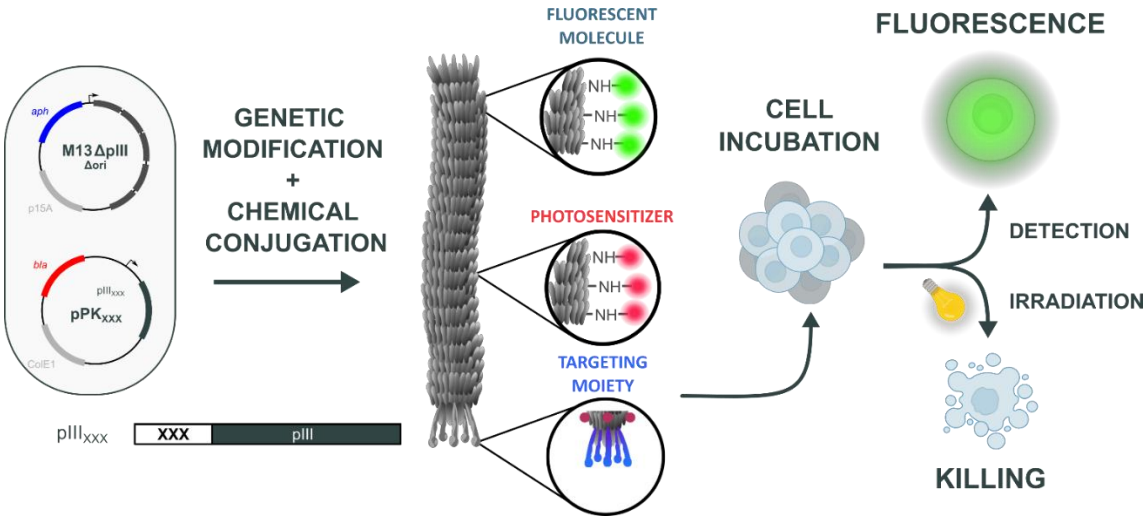

Figure 7 - Graphic abstract: Genetic modification of a phagemid produces a retargeted phage. This phage can be chemically conjugated to either fluorescent molecules or photosensitizers, allowing targeted delivery of these conjugated molecules to specific cells. Upon photoactivation, the targeted cells are selectively killed.

Results and discussion

1. Anti-EGFR Photodynamic Therapy Using M13 Engineered Phage with a targeting peptide.

M13 phages were engineered to specifically target the Epidermal Growth Factor Receptor (EGFR) by displaying the SYPIPDT peptides on their minor coat protein, pIII. It's noteworthy that EGFR, when overexpressed, can stimulate uncontrolled growth, leading to tumorigenesis in a variety of tumors such as those found in the breast, lung, brain, head, neck, and colon. Recognizing the pivotal role of EGFR in tumorigenesis, several therapeutic agents targeting this receptor have been developed and approved. This shift towards targeting EGFR epitomizes the transition in oncology from a generic chemotherapy approach to a molecularly targeted one. To achieve this specific targeting, a synthetic oligonucleotide encoding the SYPIPDT peptide was cloned with the pIII gene of a phagemid vector. This allowed the peptide to be displayed on the phage tip with the assistance of helper phages. The choice of the SYPIPDT peptide was twofold: firstly, its ability to target EGFR [50], and secondly, its lack of amino groups which ensures no interference with the orthogonal functionalization of the virus capsid. This functionalization involves the free amino groups of N-terminal alanine and lysine (Lys8) on pVIII, which are crucial for selective chemical conjugation. Importantly, since the targeting moiety is displayed on the minor coat protein (pIII), the major coat protein pVIII, with its 2700 copies, retains a significant cargo capacity (around 5400 conjugation sites). This allows for the attachment of imaging tags or PSs to the vector capsid without compromising the specific targeting capabilities of the SYPIPDT peptides.

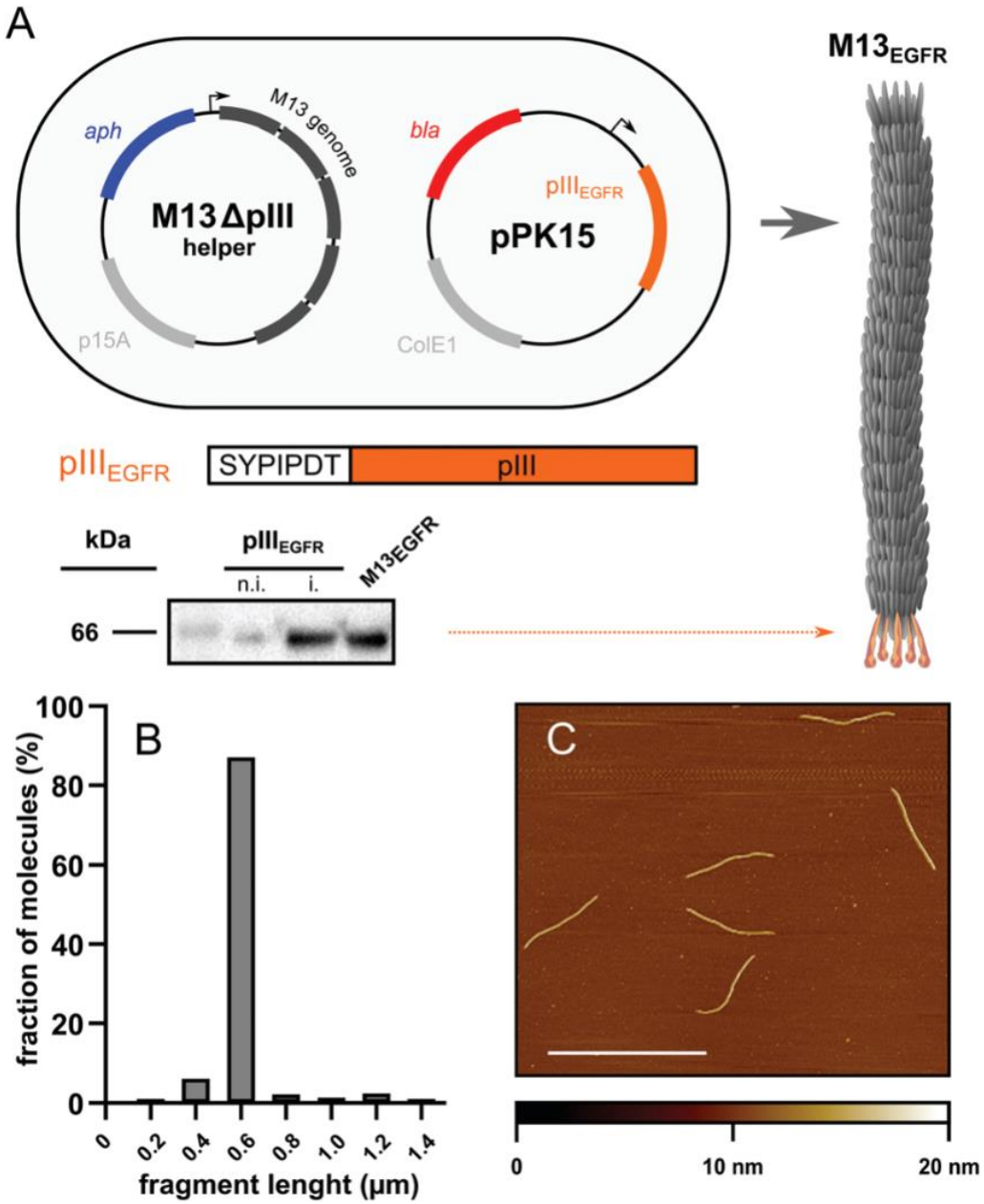

Figure 8- Genetic engineering of M13EGFR phage includes: (A) The episomal components that encode the M13EGFR phage and an immunoblot showcasing the SYPIPDT-pIII fusion, which confirms its integration into the purified virion. Key elements: pPK15 with ampicillin resistance cassette (red); ColE1 ori; pIIIEGFR fusion (orange). The M13ΔpIII helper consists of aph kanamycin resistance cassette (blue); p15A ori, and M13 genes (excluding pIII, shown in dark grey). (B) The size variation of M13EGFR phages as identified by AFM. (C) An AFM image of the isolated M13EGFR phages. Scale bar represents 1 μm [51].

To validate the accurate expression of the SYPIPDT-pIII fusion, immunoblotting was employed using an anti-pIII antibody. The resulting band, corresponding to the anticipated molecular weight, was observed in immunoblots of *E. coli* cultures containing the pPK15 phagemid, as illustrated in Figure 8A. This SYPIPDT-pIII fusion was similarly identified in the purified recombinant phages, confirming the successful integration of the targeting peptide into the $M13_{EGFR}$ virions.

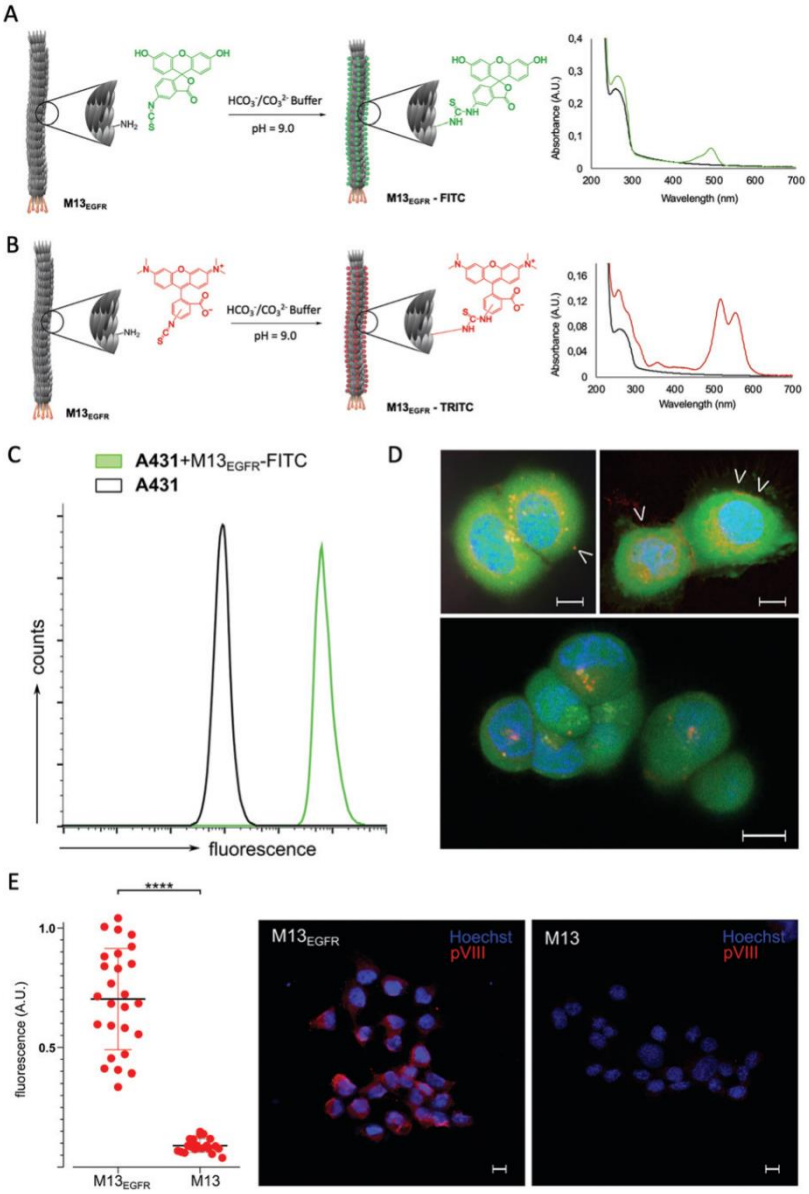

Figure 9 - (A) FITC Conjugation with $M13_{EGFR}$: Absorption spectra for $M13_{EGFR}$ is represented by the black line, while $M13_{EGFR}$–FITC is shown by the green line. Given the starting $M13_{EGFR}$ concentration and FITC's molar extinction coefficients, an estimated 200 FITC molecules are attached to each $M13_{EGFR}$. (B) TRITC Conjugation with $M13_{EGFR}$: The black line depicts the absorption spectra of $M13_{EGFR}$, and the red line represents $M13_{EGFR}$–TRITC. Based on the initial $M13_{EGFR}$ concentration and TRITC's molar extinction coefficients, around 1700 TRITC molecules are bound to each $M13_{EGFR}$. (C) Flow cytometry evaluates the refactored $M13_{EGFR}$–FITC phages aimed at the A431 cell line, which overexpresses EGFR. (D) Confocal microscopy images of A431 cells show the internalized $M13_{EGFR}$–TRITC phages (in red), cell nuclei (Hoechst, in blue), and the cytoplasm (calcein AM, in green). Arrow indicators point to phages situated near cell edges. (E) The retargeting towards the EGFR receptor facilitates the specific uptake of the $M13_{EGFR}$ phage vector. Immunostaining displays the pVIII major capsid protein (in red) and nuclei (Hoechst, in blue). The scale bar measures 10 µm [51].

To further characterize these phage preparations, Atomic Force Microscopy (AFM) was utilized in a solution-based setting. The resulting images revealed that

the $M13_{EGFR}$ phages were intact, exhibiting an approximate diameter of 4.7 nm. Furthermore, the contour length distribution was predominantly around 575 (±45) nm, as determined from an analysis of 365 phage molecules (see Figures 8B and C). This reduced phage length is indicative of the proper packaging of the smaller pPK15 phagemid into the $M13_{EGFR}$ virion, which is favoured over the packaging of the more extensive M13ΔpIII helper phage genome. Less than 7% of the analysed phages displayed an exceeding length. Most of these outliers were approximately double the standard phage length, suggesting they might be dimeric entities, containing two packaged phagemids. The preserved structural integrity, coupled with the anticipated size distribution (refer to Figures 8B and C), provides robust evidence supporting the successful engineering of the $M13_{EGFR}$ platform. To assess the capability of the displayed peptides to target specifically towards A431 cells, $M13_{EGFR}$ phages were chemically conjugated with FITC, as depicted in Figure 9A. The A431 cell line, derived from human epidermoid squamous carcinoma, is characterized by an amplified EGFR gene, leading to a high expression of the receptors on their cell membranes. This makes A431 an ideal model to evaluate the targeting efficiency of EGFR-retargeted phages. Upon $M13_{EGFR}$–FITC incubation with these cells at a multiplicity of 100:1, a distinct shift in fluorescence intensity was observed via flow cytometry after 30-minute, confirming the phage vector's targeting capability (see Figure 9C). Previous studies have shown that filamentous phages, when displaying receptor-targeting peptides, can be selectively taken up by cells, as evidenced in the SKBR-3 breast cancer cell line [52].

To further delve into the cellular uptake and localization of $M13_{EGFR}$, a $M13_{EGFR}$–TRITC conjugate was synthesized, as shown in Figure 9B. When this conjugate was co-incubated with A431 cells, rapid phage vector internalization was observed within 30 minutes, predominantly accumulating in the cell's perinuclear compartments (refer to Figure 9D). Detailed examination of confocal microscopy images also revealed the presence of $M13_{EGFR}$ phages on the cell surface, as indicated by arrowheads in Figure 9D. This suggests a receptor-mediated uptake mechanism for $M13_{EGFR}$, an attribute highly sought-after in a PDT vector, given that PSs require cellular internalization to maximize treatment efficacy. The

specificity of $M13_{EGFR}$ vector internalization was further scrutinized using immunocytochemistry, employing antibodies targeting the major capsid protein pVIII (Figure 9E). Remarkably, the fusion of the SYPIPDT peptide to pIII resulted in an over tenfold enhancement in the binding rate of $M13_{EGFR}$ compared to its non-retargeted M13 phage control. This underscores the altered targeting ability of the re-engineered phage vector.

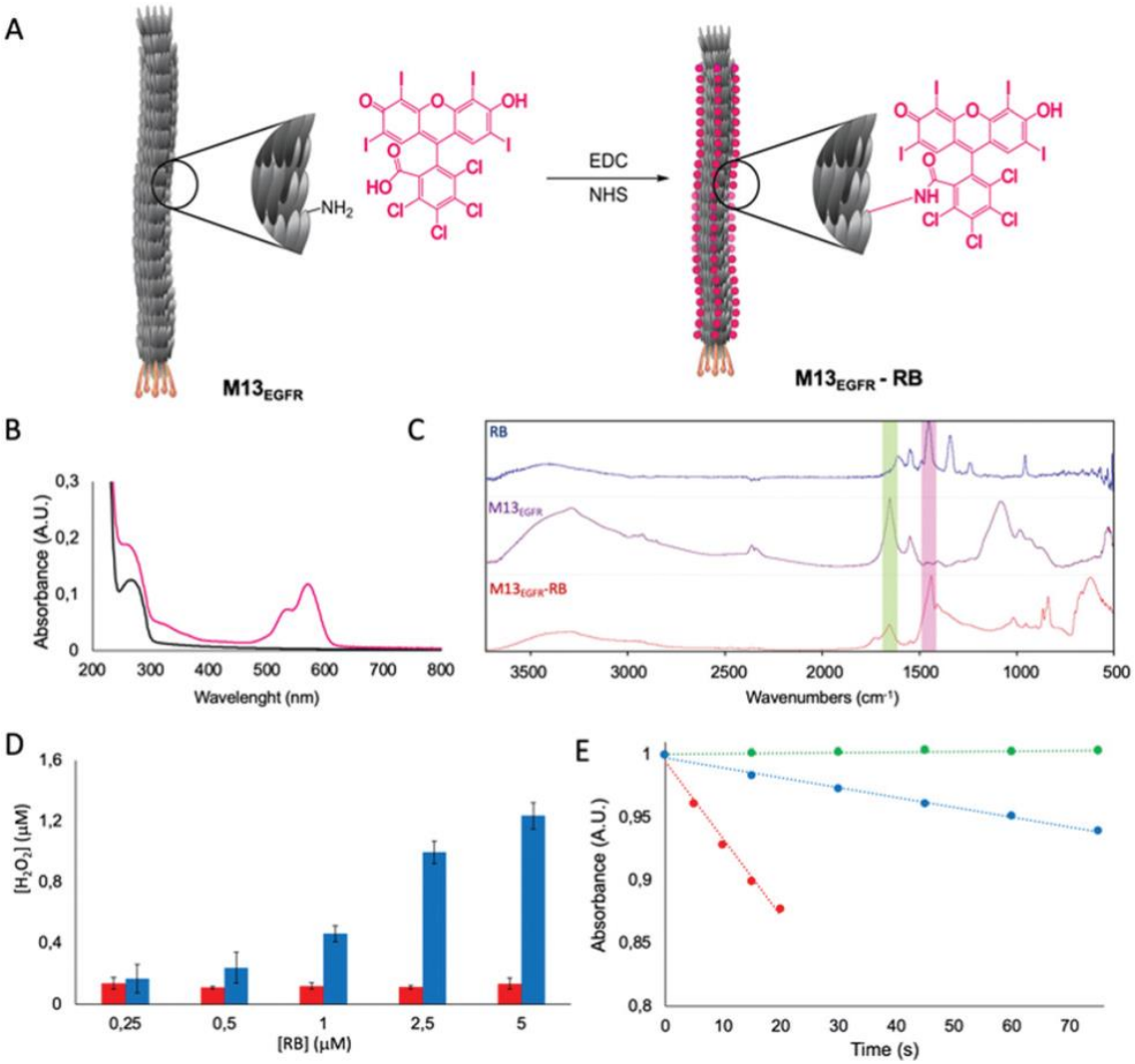

Figure 10 - (A) The process of conjugating RB to $M13_{EGFR}$. (B) Absorption spectra comparison between $M13_{EGFR}$ (represented by the black line) and $M13_{EGFR}$–RB (depicted by the rose line). (C) ATR-FTIR spectra showcasing RB, $M13_{EGFR}$, and the conjugated $M13_{EGFR}$–RB. (D) Peroxide generation illustrated using varying concentrations of RB (in red) and $M13_{EGFR}$–RB (in blue). (E) Analysis of 1O2 generation by monitoring the reduction in ABMDMA absorbance against irradiation time under white light. The spectra for $M13_{EGFR}$, $M13_{EGFR}$–RB, and RB are represented by green, blue, and red lines respectively[51].

Rose Bengal (RB) is an FDA-approved dye with a longstanding clinical history, having been utilized in ophthalmological procedures for over three decades[53]. Commercially known as PV-10, RB has been extensively studied in clinical trials for its potential therapeutic effects against human melanoma and is currently

progressing through stage III trials[53]. Beyond its clinical applications, RB molecules have garnered attention as PSs, showcasing promising potential in PDT.

In our research, we chemically conjugated RB molecules to the capsomers of the $M13_{EGFR}$ phage. This conjugation of $M13_{EGFR}$ with RB ($M13_{EGFR}$–RB), was achieved using an EDC/NHS cross-coupling reaction. This reaction allows the bond between the amino groups present in the $M13_{EGFR}$ capsomers and the activated carboxylic-acid group of RB, as illustrated in Figure 10A. After conjugation, the absorbance slope of the purified $M13_{EGFR}$–RB, depicted in Figure 10B, underwent a shift to 560 nm and broadened confirming the successful attachment of RB to the $M13_{EGFR}$ capsid. Based on the initial concentration of $M13_{EGFR}$ and the molar extinction coefficients of RB, we estimated that around 710 RB molecules were attached to each $M13_{EGFR}$ phage.

Further evidence of this conjugation was provided by ATR-FTIR spectroscopy, as shown in Figure 10C. The spectrum of the $M13_{EGFR}$–RB bioconjugate distinctly displayed both the Amide I band (1652 cm^{-1}), characteristic of the phage, and a diagnostic band of RB (1439 cm^{-1}) associated with the CvC stretching of its aromatic component.

To assess the photodynamic potential of the $M13_{EGFR}$–RB conjugate, we evaluated its ability to produce ROS upon exposure to visible light. Using the Amplex Red assay (Figure 10D) for peroxide detection and ABMDMA (Figure 10E) for singlet oxygen detection, we observed that $M13_{EGFR}$–RB exhibited enhanced peroxide generation compared to RB alone. However, the singlet oxygen quantum yield (ΦΔ) of $M13_{EGFR}$–RB ($\Phi\Delta_{M13–RB} = 0.10$) was found to be lower than that of free Rose Bengal ($\Phi\Delta_{RB} = 0.76$).

Conjugating Rose Bengal (RB) to the $M13_{EGFR}$ capsomer proteins, there's a notable shift in photoactivation from type II (an energy transfer process) to type I

(an electron transfer process) mechanisms. This shift enhances the production

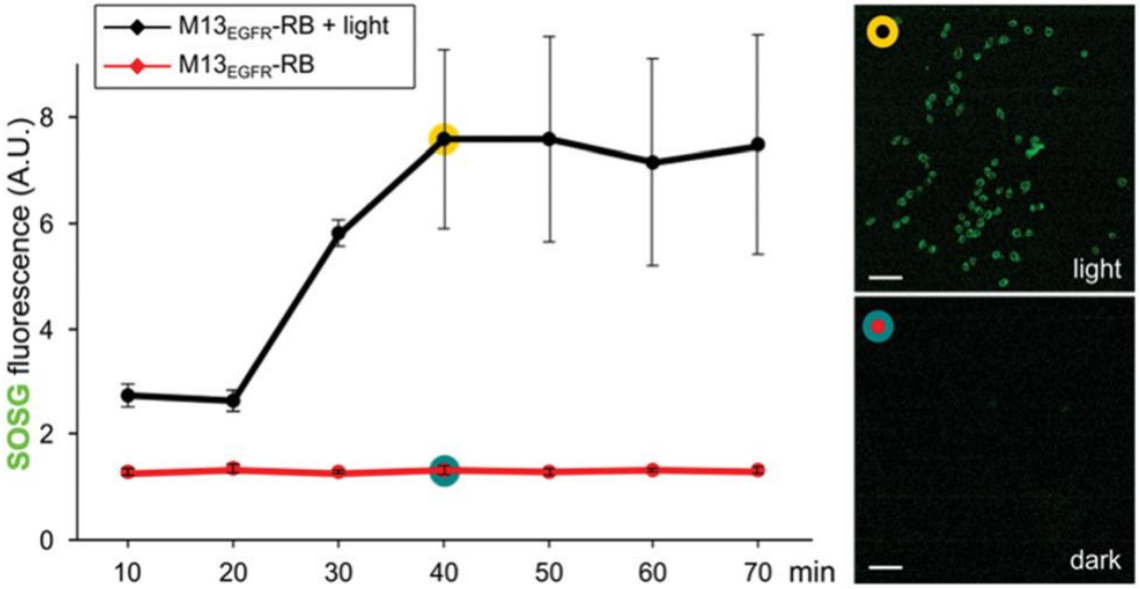

Figure 11 Photoactivity of M13EGFR–RB observed through SOSG fluorescence under light exposure. As the fluorescence intensity of SOSG rises, it indicates a proportional increase in singlet oxygen concentration, providing an estimate of the intracellular ROS generated. Scale bar represents 50 μm [51].

of peroxides over singlet oxygen ($^1O_2$), a behaviour previously observed when. RB is coupled to proteins.[54] Typically, the activation of the type I mechanism necessitates a sacrificial electron donor, implying that environments rich in electrons are conducive to type I processes. In this context, the protein residues of the phage might directly facilitate the electron transfer, obviating the need for the external introduction of electron-donating entities. This characteristic is particularly intriguing, given the growing interest in developing type I PSs for anticancer PDT.

To evaluate the photodynamic capabilities of the bioconjugated $M13_{EGFR}$–RB, we aimed to track the in-cell production of ROS during irradiation using various reporters. Initial experiments employed AmplexRed and dichlorofluorescein (DHFC) to detect peroxides produced in cells upon irradiation of the $M13_{EGFR}$–RB vector. However, these attempts did not yield definitive results due to the overlapping spectral properties of these dyes with the RB sensitizer, complicating the differentiation of signal contributions. Similarly, the CellROX™ detector was found unsuitable as its fluorescence was merely activated by cell irradiation, without providing clear insights. In contrast, the singlet oxygen sensor green

(SOSG) exhibited spectral properties distinct from RB and remained inactivated by photodynamic irradiation alone, making it an ideal candidate to demonstrate in-cell ROS production mediated by the phage vector, as illustrated in Figure 11.

A431 cells were treated with M13$_{EGFR}$–RB and SOSG, followed by irradiation using a white LED lamp. Post-irradiation, confocal microscopy was employed to capture micrographs at regular intervals, monitoring SOSG emission. Notably, SOSG fluorescence reached its peak and plateaued after 40 minutes, but only in specimens that were irradiated in the presence of M13$_{EGFR}$–RB. In contrast, control samples, either kept in the dark or irradiated without M13$_{EGFR}$–RB, consistently displayed a diminished SOSG fluorescence, as depicted in Figure 11

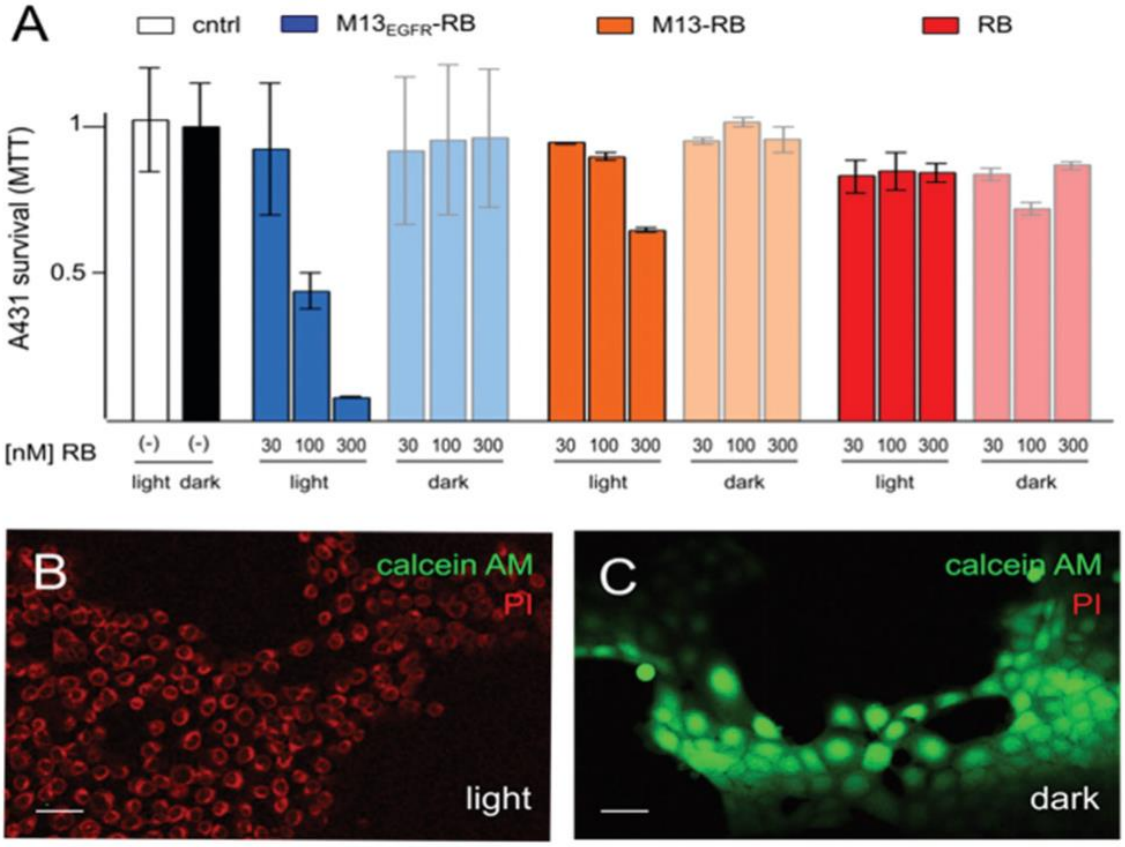

Figure 12 - Photodynamic targeting of the epidermoid cancer cell line: (A) Post 24 hours of low-intensity PDT treatment, A431 cell survival rates are presented for M13EGFR–RB, M13–RB, and RB alone. Control samples were maintained in darkness. The error bars represent the standard deviation from six repeated tests. (B) Light irradiation triggers M13EGFR–RB to rapidly initiate membrane permeability and reduce cell viability, observed 30 minutes post-irradiation. The markers used are calcein AM (in green) and propidium iodide (PI, in red). The scale bar measures 50 μm. (C) Observations like (B) but without any light irradiation [51].

Reflecting upon the enhanced internalization and the augmented capability of the engineered vector to produce peroxides over singlet oxygen, it's evident that $M13_{EGFR}$–RB acts as a potent intracellular ROS generator upon light activation.

To further evaluate the anticancer photodynamic potential of the $M13_{EGFR}$–RB bioconjugates, experiments were conducted on A431 cells. These cells were treated with $M13_{EGFR}$–RB, M13–RB, or RB alone for 90 minutes. Post-incubation, cells were washed to eliminate any unbound photosensitizing agents and then exposed to a low irradiance (2.4 mW cm^2) white LED light for 30 minutes. Control samples were kept in dark. After a 24-hour recovery period, cell survival rates were assessed using the MTT cell viability assay. Notably, while treatments with M13–RB and RB alone did not exhibit any significant cytotoxic effects, $M13_{EGFR}$–RB demonstrated remarkable efficacy in eliminating A431 cells. This was evident even at concentrations as low as 100 nM RB equivalents, which translates to 140 pM $M13_{EGFR}$–RB phage concentration (as shown in Figure 12A). To our knowledge, this represents one of the most potent concentrations ever reported for PDT treatments. At the highest concentration tested, $M13_{EGFR}$–RB induced near-total eradication of A431 cells, as indicated by the pronounced reduction in calcein staining and the significant uptake of the typically impermeable propidium iodide stain within 30 minutes post-irradiation (Figure 12B). Importantly, these effects were absent in non-irradiated samples (Figure 12A), underscoring the inherent safety and minimal cytotoxicity of M13 phages in the absence of light activation.

Contrastingly, the photodynamic efficacy of non-refactored phages (M13–RB, as shown in Figure 12C) was less pronounced, especially at lower RB equivalent concentrations, highlighting the specificity imparted by the phage engineering. Only at elevated concentrations of M13–RB was a non-specific cytotoxic effect observed, which is likely attributed to residual phages passively adhering to the cell layer during incubation. In conclusion, these findings emphasize that $M13_{EGFR}$–RB, upon internalization, facilitates the generation of cytotoxic ROS when the RB PS is activated by light.

2. Colon Cancer Targeting: Molecularly Engineered Phage Nanovector for Photodynamic Therapy

To engineer the M13 phage vector to specifically bind to colon cancer (CC) cells, we utilized a nine-amino-acid, disulfide-constrained peptide, CPIEDRPMC. This peptide was previously isolated from a phage-display library using the HT29 CC cell line as a target [23]. We hypothesized that this peptide could serve as an effective ligand to modify the tropism of the M13 phage towards CC cells.

The genetic sequence encoding the CPIEDRPMC peptide was integrated in-frame with the pIII gene of a phagemid vector. This configuration enabled a pentavalent display of the peptide-pIII fusion at one terminus of the phage. To complement the remaining M13 genes, we employed the Hyperphage (deltapIII) helper phagemid (Figure. 13I). Following the production and purification processes (detailed in the Materials and Methods section), the resultant $M13_{CC}$ virions were subjected to validation for peptide display using Immunoblotting techniques (Figure. 13I).

To evaluate the targeting efficiency of the engineered M13CC, we employed immunohistochemical confocal microscopy on HT29 and DLD1 cell lines (Figure 13A-10H and the graph in Figure. 13J). Our findings revealed that the $M13_{CC}$ displayed a pronounced affinity for both CC cell lines, particularly the HT29 (Figure. 13C and 13G). Control experiments, utilizing the unaltered wild-type M13 phage, exhibited no discernible differences when juxtaposed with the control samples (Figure. 13B and 13F). This underscores that the specific binding of $M13_{CC}$ to CC cells is facilitated by the CPIEDRPMC peptide display.

Given that preincubation with Fibronectin (FN) has been documented to compete the binding of the targeting peptide to CC cells [24], we concurrently explored the inhibitory effect of FN on $M13_{CC}$ binding. Our observations indicated that pre-treatment with FN notably hindered the binding of $M13_{CC}$, especially in the HT29 CC cell line (Figure 13J), corroborating prior studies.

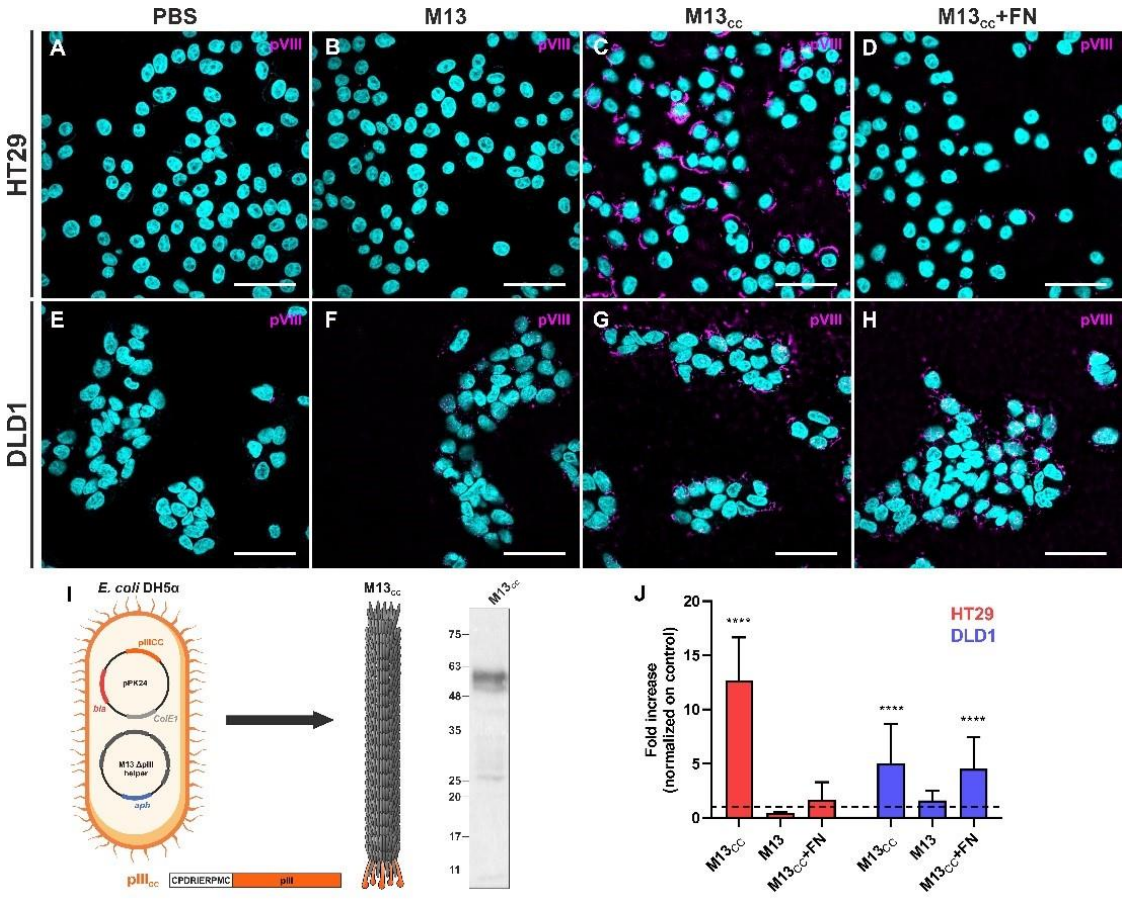

Figure 9 – M13cc specifically targets CC cells as observed through immunohistochemical confocal microscopy. In the HT29 cell line: (A) cells were incubated with PBS, (B) treated with M13, (C) exposed to M13cc, and (D) interacted with M13CC after pre-treatment with fibronectin (FN). For the DLD1 cell line: I cells were incubated with PBS, (F) treated with M13, (G) exposed to M13CC, and (H) interacted with M13cc after pre-treatment with fibronectin (FN). In these images, cell nuclei are depicted in cyan, while the major coat protein pVIII of the phage is shown in magenta. The scale bar represents 50 µm. (I) A schematic representation of the phage modification shows that the CPDIRIERPMC coding sequence was integrated in tandem with pIII (highlighted in orange), resulting in the pPk24 plasmid. Bacteria transformed with this plasmid, when superinfected with the Hyperphage helper, yield modified phages. An immunoblot of M13cc confirms the inclusion of the altered pIII in the purified virions. (J) A quantitative analysis was conducted on the confocal images. The fluorescence intensities observed were expressed as a fold increase relative to the control PBS (indicated by a dashed line). The statistical significance of these observations was determined using one-way ANOVA, comparing each set to the control (PBS). A significance level of ****p < 0.0001 was noted.

Furthermore, we bioconjugated RB to the M13cc virions through the EDC/NHS cross-coupling reaction. In this reaction, the activated carboxylic-acid group of RB interacts with the accessible N-terminal and lysine side chain of M13cc capsomers, to reach a covalent amidic bond. UV-Vis spectroscopic analysis (Figure.11A) of the resultant bioconjugate manifested a distinct peak shift and a wider RB absorption spectrum relative to RB alone. These spectral alterations unequivocally verified the bioconjugation of RB to the M13cc capsid. Leveraging on the extinction coefficient of RB, we deduced an average conjugation of

approximately 910 RB molecules per individual phage virion.

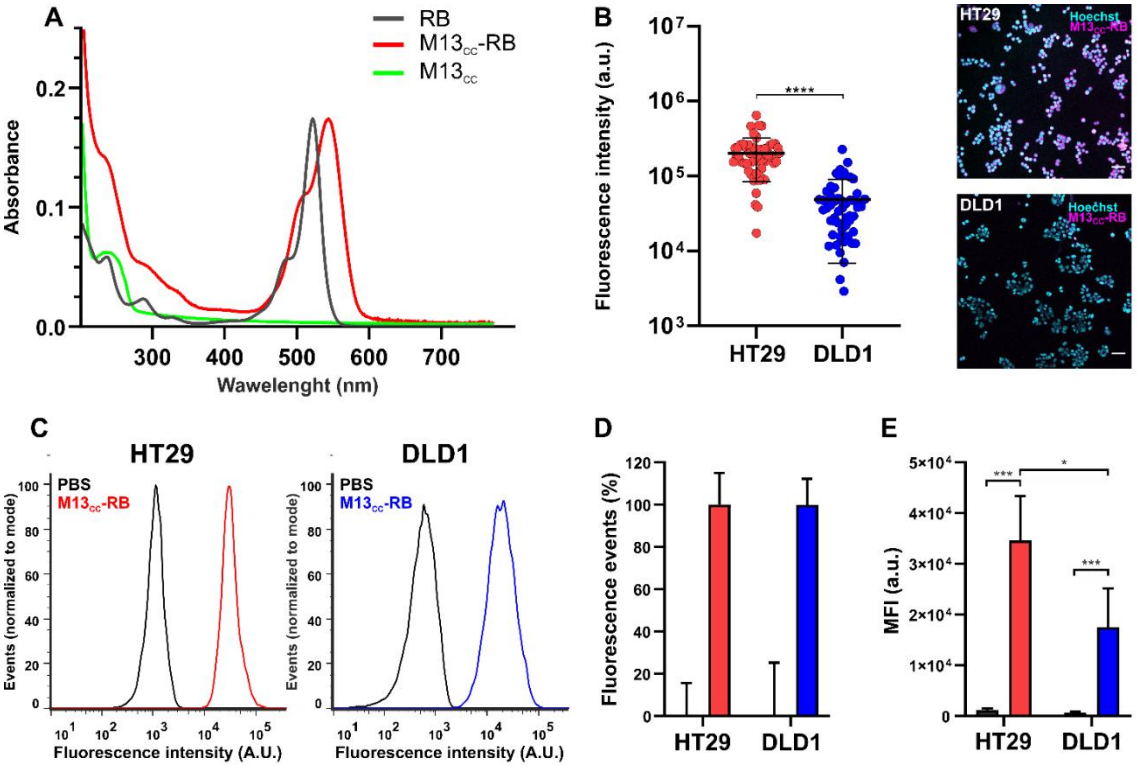

Figure 14 - Enhanced targeting of M13CC-RB is observed towards CC cells, with a notably higher affinity for HT29 cells. In (A), the UV-VIS absorption spectra are represented for RB (in grey), M13CC-RB (in red), and M13CC (in green). Moving to (B), a microscopic examination showcases the retargeting capabilities of the engineered 1 µM phage on HT29 and DLD1 CC cell lines. The statistical significance between the two was determined using a t-test, with a significance level of ****$p < 0.0001$ for HT29 compared to DLD1 cells. In (C), flow cytometry was employed to analyze the retargeting efficiency of the RB-conjugated M13CC phage against HT29 (represented in red) and DLD1 (shown in blue), with PBS serving as the control and depicted in black. For (D), the percentage of fluorescent events was quantified using flow cytometry. Lastly, in (E), the mean fluorescence intensity for HT29 and DLD1 cells, post-incubation with RB-M13CC, is presented, with PBS serving as the control (shown in black). All graphical representations and computations were executed using FlowJoTM software.

The tropism of the bioconjugated $M13_{CC}$-RB phage vector was meticulously assessed on two colon cancer cell lines: HT29 and DLD1. To validate the retargeting capability of this RB phage bioconjugate, we employed both confocal microscopy and flow cytofluorimetry. The intrinsic fluorescence of the RB sensitizer served as a pivotal marker in these analyses.

Confocal microscopy was utilized to provide a detailed visualization of the binding proficiency of the RB phage bioconjugate vector to the cell lines. Semi-quantitative analyses, as depicted in Figure 14B, were conducted to elucidate the extent of retargeting. Our findings revealed a pronounced retargeting capability

of the vector towards both cell lines. Notably, the affinity was significantly more pronounced for the HT29 cells, mirroring the observations made with the unconjugated M13$_{CC}$.

To further substantiate these findings, flow cytometry analyses were executed on both cell lines. The discernible shift in fluorescence intensity peak, as illustrated in Figure 14C relative to the control (which consisted in cells incubated with only PBS), attested to the retargeting prowess of the vector across both cell lines. Remarkably, the fluorescence was observed in 100% of the cell populations for both CC cell lines, as shown in Figure 14D, signifying comprehensive targeting. A comparative analysis of the mean fluorescence intensity (MFI) revealed a markedly higher intensity for HT29 cells compared to DLD1 cells (Figure 14E). This observation was congruent with the data obtained from the confocal microscopy experiments.

Collectively, these results underscore that the conjugation process with the RB PS did not compromise the inherent tropism of the phage vector. The vector retained its preferential binding affinity towards the HT29 cells.
To assess the photodynamic efficacy and specificity of the M13CC-RB phage nanovector, we exposed both the high-affinity HT29 and the low-affinity DLD1 CC cell lines to increasing concentrations of either M13CC-RB or unconjugated RB alone. After incubation, the cells were washed thoroughly and then irradiated with a low power LED lamp for 30 minutes. Control samples were kept in the dark.

Our observations revealed that the toxicity in the light absence (dark toxicity) was completely negligible. Moreover, the use of RB alone resulted in minimal cytotoxic effects, as depicted in Figure 15A. However, a notable concentration-dependent decline in cell viability was evident post-treatment with photo-irradiated M13$_{CC}$-RB across both HT29 and DLD1 cell lines (Figure 15B). Strikingly, the retargeted vectors exhibited profound cytotoxicity towards HT29 cells even at the minimal tested concentration (0.1 µM RB equivalents), with only 8% ± 0.8 of the cells remaining viable. In contrast, DLD1 cells displayed a more modest cytotoxic response at the same concentration, with a viability of 72% ± 0.9. It's important to note that this differential response cannot be ascribed to varying photosensitivity between the two cell lines, as both HT29 and DLD1 demonstrated analogous viability profiles when irradiated in the absence of either

sensitizer or phage. As a result, while the reduction in cell viability was similar at higher sensitiser concentrations (0.3 and 1 μM RB equivalents, as shown in Figure 15B), HT29 cells exhibited increased sensitivity to phage-mediated PDT, confirming the superior targeting efficiency of M13CC-RB to this cell line (as evidenced in Figure 14E).

These findings collectively elucidate two pivotal insights:

i) The engineered M13$_{CC}$-RB phage nanovector efficiently delivers light-activated photosensitiser (PS) molecules to CC cells, eliciting photodynamic cytotoxic responses even at picomolar vector concentrations.

ii) The cytotoxic effects are enhanced in cell lines with enhanced targeting efficiency, highlighting the photosensitisation specificity conferred by the phage vector.

Given the marked sensitivity of HT29 cells to M13$_{CC}$-RB-mediated PDT, subsequent investigations were tailored to elucidate the mechanistic underpinnings of the phage-induced cytotoxic effects only on this cell line.

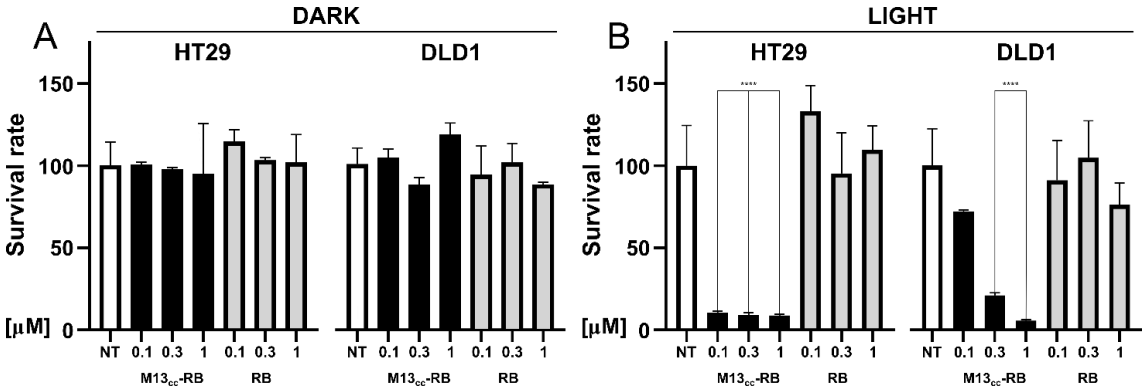

Figure 15 - *Photoirradiated M13$_{CC}$-RB significantly reduces the viability of CC cells. The cytotoxic impacts of M13CC-RB or just RB on HT29 and DLD1 cells were observed when these cells were either kept in the dark (labeled as DARK in section A) or exposed to a white LED bulb for 30 minutes (labeled as LIGHT in section B), with observations made 24 hours post-treatment. The MTT test was utilized to analyze cell viability. The statistical significance of the results was determined using one-way ANOVA, followed by Dunnet's multiple comparison test. Significance levels were marked as * p < 0.05; *** p < 0.001; **** p < 0.0001 when compared to untreated cells, labeled as NT.*

To delineate the underlying mechanisms responsible for the photo-induced cytotoxicity exhibited by M13$_{CC}$-RB, we embarked on a comprehensive examination of the ROS genesis facilitated by this phage vector in an in vitro cell-free system. The photodynamic attributes of M13$_{CC}$-RB were assessed via two distinct methodologies: Amplex Red (AR) assay, useful for the quantification of

peroxide species (Figure. 16A), and the ABMDMA assay, optimized for the detection of singlet oxygen ($^1O_2$) entities (Figure. 16B).

When isoabsorbing RB solutions were subjected to the AR assay through a concentration gradient from 0.25 to 4 μM, it was found that the bioconjugation of RB to the M13 phage significantly enhanced peroxide production compared to the isolated photosensitiser (PS).Conversely, the quantum yield of singlet oxygen generation by M13$_{CC}$-RB ($\Phi\Delta = 0.20$) manifested a diminished efficacy relative to an equimolar solution of the RB alone ($\Phi\Delta = 0.76$). Control reactions, executed in dark, validated the absence of ROS genesis, thereby reinforcing the photodynamic nature of this phenomenon.

To assess the phage's aptitude in producing intracellular ROS—a central determinant for efficacious PDT—we employed the highly sensitive ROS-Glo™ bioluminescent assay, which is used to quantitatively assess intracellular hydrogen peroxide concentrations. HT29 cells were exposed to M13$_{CC}$-RB at concentrations of 0.3 and 1 μM and photo-irradiated. The ensuing intracellular ROS concentrations were normalized against those elicited by the RB alone. A pronounced 7-fold amplification in intracellular ROS was observed at the higher phage concentration probed. Contrarily, the ROS induction mediated by the unbound RB was risible at best under analogous experimental parameters. Additionally, dark conditions ROS genesis remained negligible (Figure. 16C). These empirical data strongly suggest that the cytotoxic effect by the M13$_{CC}$ phage vector is predominantly attributable to the intracellular production of ROS.

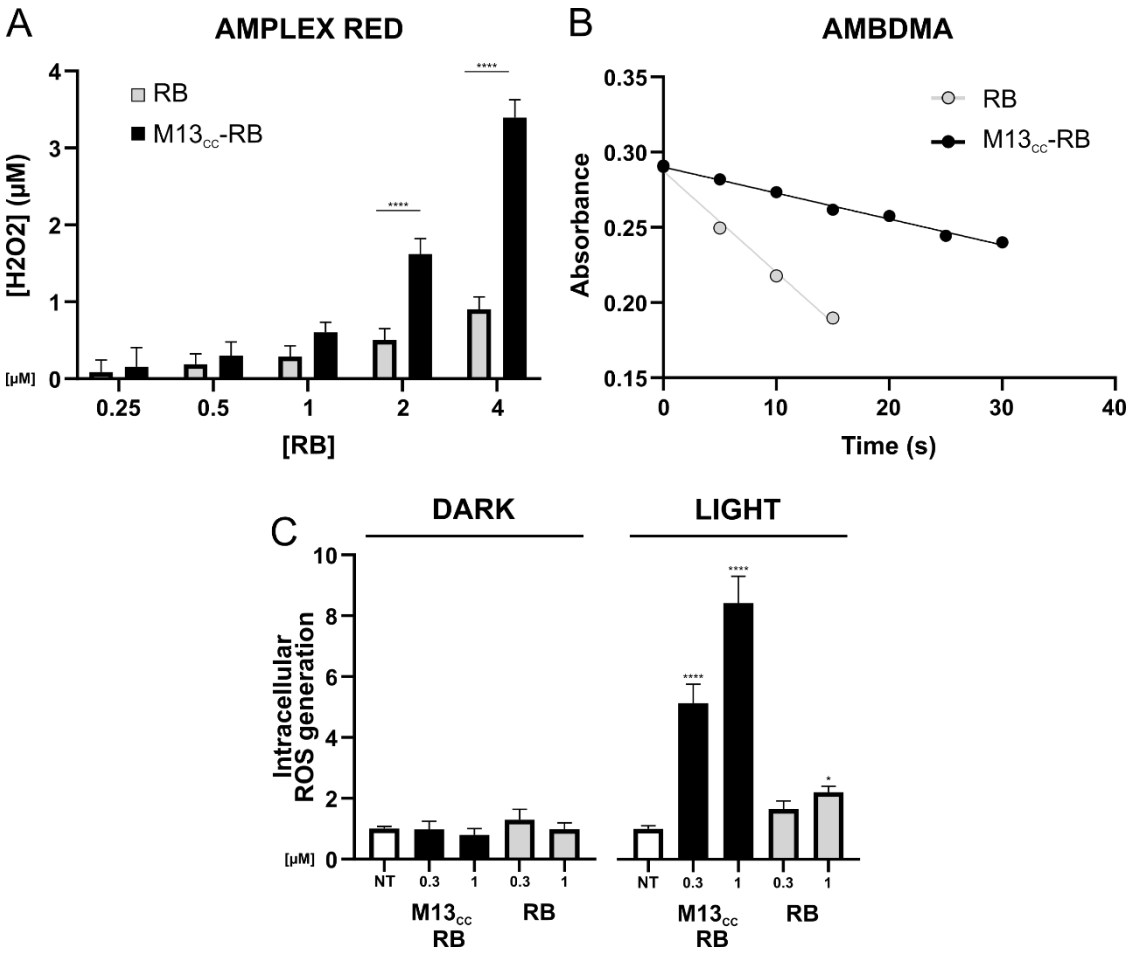

Figure 16 - M13CC-RB elevates intracellular ROS levels upon irradiation. In (A), the quantification of peroxides, as determined by the AR test, showcases the amounts produced by varying concentrations of RB (represented by white squares) and M13CC-RB (represented by black squares) following 30 minutes of white LED irradiation. In (B), the generation of singlet oxygen by RB (indicated by grey dots) and M13CC-RB (indicated by black dots) is presented over increasing durations of irradiation, with the monitoring based on the diminishing UV-Vis absorption of ABMDMA. Moving to (C), the generation of intracellular ROS is measured using the ROS-Glo assay (by Promega) after HT29 cells are exposed to M13CC-RB, both in the presence and absence (dark) of 30-minute irradiation. The statistical significance of the findings was determined using two-way ANOVA, followed by Dunnet's multiple comparisons test. Significance levels are denoted as * $p < 0.05$ and **** $p < 0.0001$ when compared to the untreated cells, labeled as NT.

Cells, when subjected to specific oxidative stressors, can activate a range of molecular cell death pathways, including but not limited to necrosis, apoptosis, and autophagy [29, 30]. To discern the integrity of the cellular membrane, an indicator of cell viability, we employed the non-permeant dye 7-AAD. This dye serves as a robust marker for membrane integrity, enabling the differentiation between cells in the early stages of regulated cell death (characterized as Annexin-V+/7-AAD-) and those with compromised cellular membranes (manifested as Annexin-V+/7-AAD+).

Upon irradiation, a significant part of the HT29 cells exhibited the Annexin-V+/7-AAD+ phenotype, indicative of necrotic events. This observation was consistent

across varying post-irradiation durations and showed a dose-dependent tendency (as illustrated in Figure. 17). Specifically, the fraction of cells exhibiting dual positivity (both Annexin-V and 7-AAD) witnessed a notable increase, even at the minimal RB equivalent concentration of 0.1 μM, with the earliest post-irradiation time point assessed (3 hours, registering at 11.7% ±0.8). This trend of increasing cytotoxicity and necrotic behavior was more pronounced with increasing concentration of M13CC-RB vector or by extending the post-irradiation interval. Remarkably, at the apex RB equivalent concentration and a post-irradiation duration extending to 24 hours, a predominant majority of the HT29 cells (amounting to 85.8% ±3) exhibited compromised membrane integrity, as evidenced in Figure. 17 . This data underscores the profound susceptibility of HT29 cells to oxidative stressors, predominantly culminating in necrotic cell death.

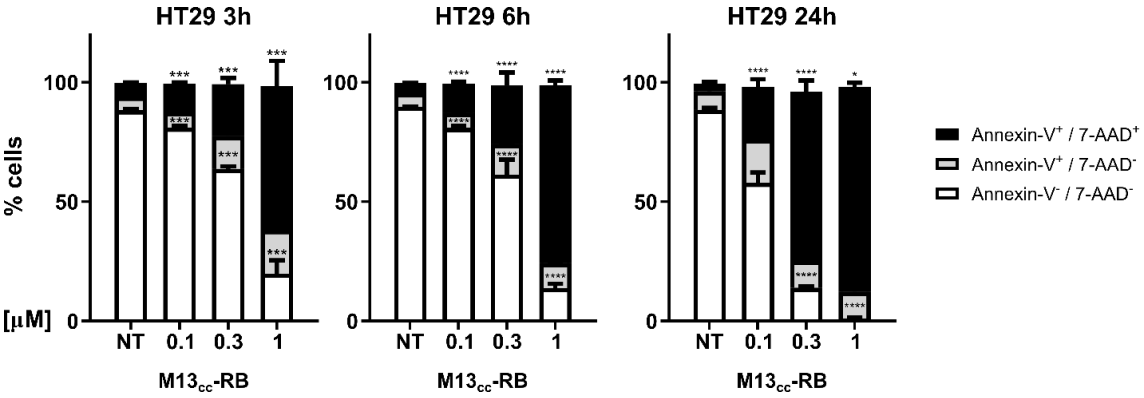

Figure 17 - Cell death mechanisms triggered by photosensitization through M13CC-RB are detailed as follows: The percentages of HT29 cells that are Annexin-V-/7-AAD-, Annexin-V+/7-AAD-, and Annexin-V+/7-AAD+ are presented after intervals of 3-, 6-, or 24-hours post-treatment with the photoactivated M13CC-RB. The statistical relevance of these observations was determined using a two-way ANOVA, followed by Dunnet's multiple comparisons test. Significance markers are * $p < 0.05$, *** $p < 0.001$, and **** $p < 0.0001$ when juxtaposed against untreated cells, denoted as NT.

Three-dimensional (3D) experimental models are emerging as pivotal tools in bridging the disparity between traditional 2D cell cultures and in vivo studies. These models adeptly emulate the architectural, biochemical, biomechanical, and intercellular interactions, offering a more authentic representation than their 2D counterparts [31]. Furthermore, they have been instrumental in unveiling novel therapeutic mechanisms associated with PDT [12, 32]. A critical precursor to assessing the efficacy of PDT is ascertaining the penetration capabilities of retargeted phages within a 3D colorectal cancer (CC) model, given that the

diffusion limitations within the tumour's inner core can significantly modulate the therapeutic response.

To start our evaluation of the phage nanovector platform within 3D models, we first sought to confirm the consistency in the generation of CC spheroids, focusing on their dimensions and morphological characteristics. This was achieved through bright field microscopy examinations and subsequent 3D reconstructions (data omitted for brevity). Post five days of spheroid growth, we employed the CyQUANT® fluorescent dye, which selectively stains actively proliferating cells. Only the peripheral layer of the CC spheroids exhibited positive staining, suggesting a central non-proliferative core encased by a proliferative cellular layer.

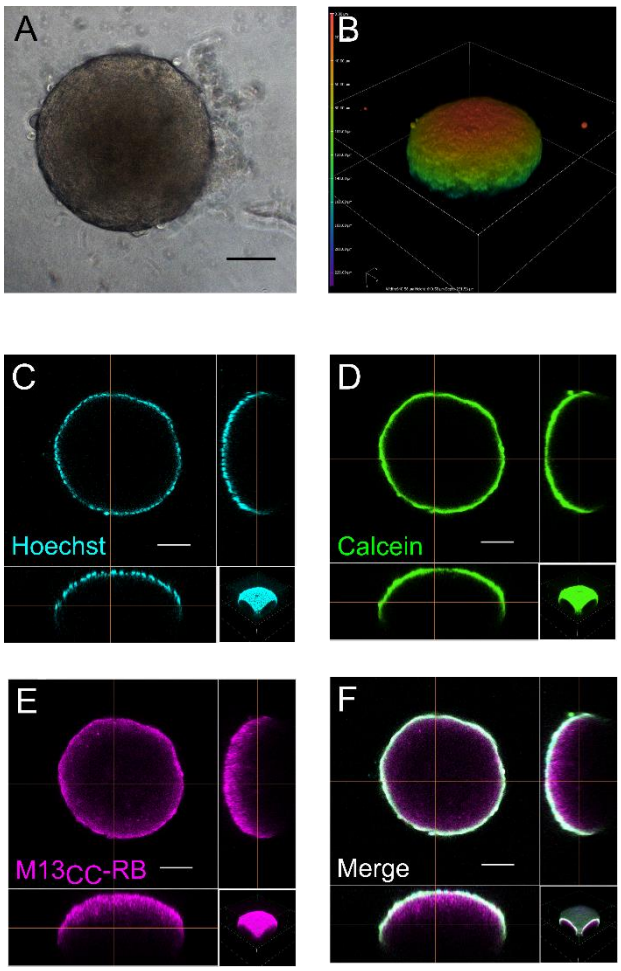

Figure 18 - M13$_{CC}$-RB exhibits profound penetration into CC multicellular spheroids. The structure of multicellular spheroids is assessed in (A) using bright field microscopy and in (B) through confocal microscopy, 24 hours post-incubation with M13$_{CC}$-RB at a 3 µM concentration of PS. A heatmap in the confocal view emphasizes Z-depth coding, which indicates the relative elevation of cells within the confocal stack, thereby attesting to the CC spheroid's integrity. The penetration of M13$_{CC}$-RB into the spheroid is depicted as follows: (C) with Hoechst staining in cyan, (D) with Calcein AM in green, (E) showing M13$_{CC}$-RB in magenta, and (F) as a merged view of all the previous stains. All images have scale bars representing 100 µm.

Our subsequent purpose was to discern the interaction dynamics between the M13$_{CC}$-RB phage vector and the CC spheroids. HT29 spheroids were incubated with the M13$_{CC}$-RB phages for 24-hour and kept in dark. Comparative analysis of bright field images, pre- and post-incubation, ascertained that the vector did not impair the spheroid's morphology and structural integrity (Figure. 18A A and 18B). We employed confocal microscopy, leveraging the inherent fluorescence of RB to pinpoint the phage vector's location. This was complemented with Hoechst (Figure. 18C) and Calcein AM (Figure. 18D) live stains to identify proliferative cells within the spheroid. Remarkably, the M13$_{CC}$-RB nanovector exhibited deep penetration capabilities, infiltrating even the non-proliferative core of the spheroid (Figure. 18E). This region typically remains impervious to even permeable low molecular nuclear stains, such as Hoechst (Figure. 18F). No structural alterations were discernible in the 3D reconstructions of the phage-infiltrated spheroid (Figure. 18B).

Collectively, these findings underscore the exceptional ability of the M13$_{CC}$-RB vector to traverse the entirety of the CC spheroid. This capability enables the delivery of the PS deep into the spheroid core, a region often inaccessible to other therapeutic entities, such as antibodies or virus-like particles.

To assess the cytotoxic effects of photoactivated M13$_{CC}$-RB within a 3D cellular context, and to juxtapose its efficacy against RB in isolation, multicellular CC spheroids were subjected to incubation with either the RB-conjugated phage or PS alone (from 1 to 3 µM RB equivalents). After 30 minutes of exposure, spheroid viability was assessed using the 3D CellTiter-Glo® reagent. Notably, a significant decrease in cell viability was observed for the M13$_{CC}$-RB at the 3 µM concentration, with 39%±5 viable cells recorded. In contrast, reduced cytotoxicity was observed at the lower RB equivalent of 1 µM for M13$_{CC}$-RB, with a viability of 71%±7 (Figure 19 A). Interestingly, no photosensitisation was observed for RB in isolation under similar conditions (Figure 19A). These empirical observations suggest that while RB in its native, unconjugated form struggles to penetrate the multicellular CC spheroid, the engineered phage vector promptly delivers

substantial payloads of RB photosensitiser deep into the spheroid, thereby inducing marked cytotoxicity upon irradiation.

The efficacy of M13$_{CC}$-RB-mediated photosensitization was assessed on the spheroids via confocal microscopy (Figure. 19B-19D). Spheroids subjected to M13$_{CC}$-RB treatment manifested a complete flattening, accompanied by a comprehensive loss of their three-dimensional integrity (Figure. 19C). This was in strong contrast to the morphological preservation observed in control spheroids (Figure. 19B) and those exposed to RB alone (Figure. 19D). This profound alteration in the spheroid's 3D architecture post M13$_{CC}$-RB treatment and subsequent photoirradiation was further corroborated through bright field microscopic evaluations of representative specimens 24 hours post-irradiation (Figure. 19E). The confocal z-stack's 3D reconstructions of M13$_{CC}$-RB treated spheroids, 24 hours post-irradiation, further accentuated this loss of structural integrity (Figure. 19F). Subsequent examinations of these spheroids, focusing on M13$_{CC}$-RB, Calcein AM, and nuclear (Hoechst) staining, were conducted (Figure. 19G-16J). A pronounced disintegration of the spheroid's architecture was evident, with a plethora of disaggregated cells exhibiting Hoechst staining (Figure. 19G). Residual phage structures were highlighted by sporadic RB fluorescence (Figure. 19I). Notably, these disaggregated cellular entities were devoid of Calcein AM

fluorescence staining (Figure. 19H), suggesting a loss of viability within the disrupted CC spheroid.

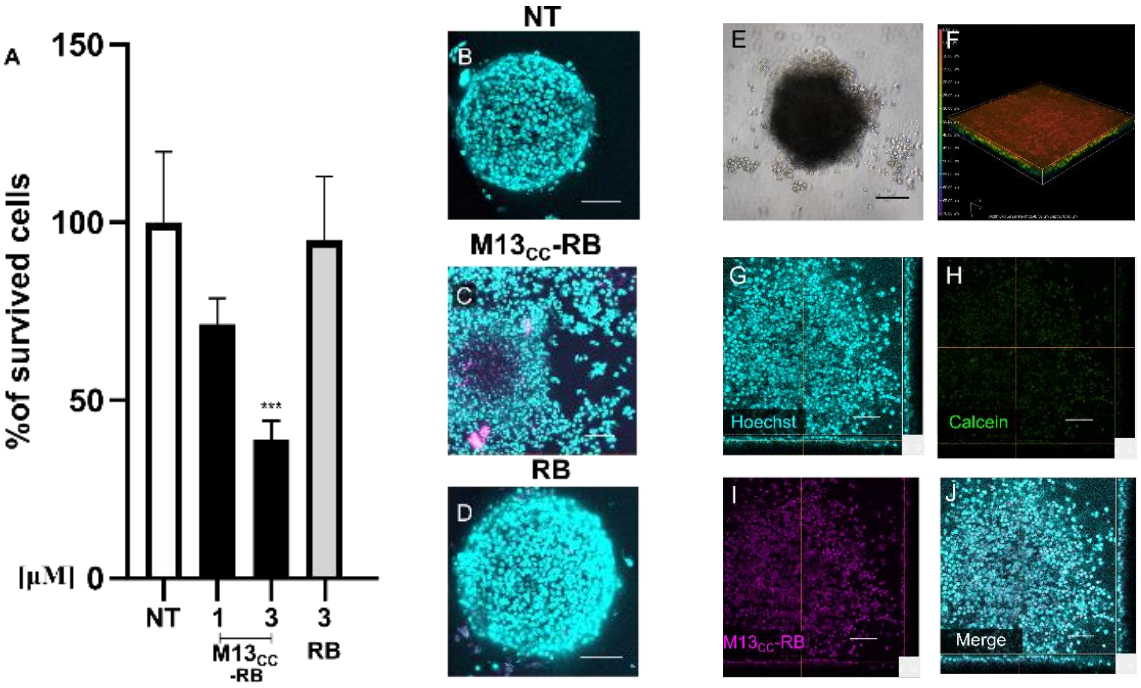

Figure 19 - M13$_{CC}$-RB compromises the structure and viability of CC multicellular spheroids when exposed to light. In (A), the cytotoxic impacts of M13$_{CC}$-RB at concentrations of 1μM and 3 μM, or RB alone at 3 μM, are presented after 30 minutes of irradiation. The 3D CellTiter-Glo® assay was employed to gauge viability. The statistical significance of these findings was determined using one-way ANOVA, followed by Dunnet's multiple comparisons test, with significance levels marked as ** $p < 0.01$ and *** $p < 0.001$ when compared to untreated cells, denoted as NT. In the subsequent images, (B) showcases an untreated control spheroid, (C) displays spheroid disaggregation post M13$_{CC}$-RB-mediated PDT, and (D) reveals the absence of spheroid disaggregation after PDT using RB alone. The structure of multicellular spheroids posts PDT with M13$_{CC}$-RB at a 3 μM concentration of PS is assessed in (E) using bright field microscopy and in (F) through confocal microscopy. A heatmap in the confocal view emphasizes Z-depth coding, indicating the relative elevation of cells within the confocal stack and pointing to the loss of spheroid integrity. The effects of M13$_{CC}$-RB photoactivation on the spheroid are depicted in (G) with Hoechst staining in cyan, (H) with Calcein AM in green, (I) showing M13$_{CC}$-RB in magenta, and (J) as a merged view of all the previous stains. All images have scale bars representing 100 μm.

In our study, the M13$_{CC}$-RB bioconjugate demonstrated in vitro PDT efficacy in two CC cell lines, HT29 and DLD1. The former showed heightened sensitivity, potentially due to differences in their DNA repair systems. Furthermore, the phage's interaction with fibronectin hinted at the involvement of the fibronectin receptor in the specific binding of the M13$_{CC}$ phages, aligning with previous findings.

Interestingly, our study revealed the phage's unique ability to penetrate cancer spheroids, a capability not previously reported. Given phages' presence in various human organs and their ability to bypass physiological barriers[55], this

finding is consistent with their potential in targeted therapies. In our experiments, the M13$_{CC}$-RB phage demonstrated deep penetration into CC spheroids, even at picomolar concentrations, suggesting its potential in enhancing PDT efficiency.

Our results also highlighted the different cell death mechanisms induced by PDT, with our M13$_{CC}$-RB primarily inducing non-programmed cell death in CC cells. The damage and subsequent cell death mechanisms are influenced by various factors, including the PS's cellular localization and the light exposure conditions. Our findings suggest that the M13$_{CC}$-RB phage induces significant intracellular ROS generation, which is pivotal for PDT-induced cell death.

In conclusion, our research highlights the potential of bacteriophage-based PDT in the treatment of CC. The M13$_{CC}$-RB phage bioconjugate shows remarkable penetration and photosensitisation capabilities in multicellular spheroids, offering a promising avenue for in vivo studies and potential clinical applications in CC and other malignancies.

3. From Peptide to Nanobody: The Evolution of Anti-EGFR Photodynamic Therapy Using the M13 Engineered Phage 2.0 Platform.

In our efforts to improve the targeting capabilities of the M13 engineered platform, we moved from the SYPIPDT peptide targeting EGFR to the 7D12 nanobody. This nanobody, with the sequence QVKLEESGGGSVQTGGSLRLTCAASGRTSRSYGMGWFRQAPGKEREFVSGI SWRGDSTGYADSVKGRFTISRDNAKNTVDLQMNSLKPEDTAIYYCAAAAGSA WYGTLYEYDYWGQGTQVTVSS, is known in literature to specifically target the outer membrane domain of the EGFR[56]. To achieve this enhanced specificity, the 7D12 nanobody sequence was cloned in conjunction with the pIII gene of the phagemid pComb3XSS vector as described in M&M. For optimized phage production, the resultant phagemid, pComb3XSS_7D12, was transformed using the HyperΔOriΔpIII Helper plasmid. This plasmid was derived from the HyperΔOri helper phage genome by removing its oriF1 sequence, ensuring the resultant genome was not encapsulated within the newly synthesized engineered phages

(Figure 20A). The production of the $M13_{7D12}$ phage was subsequently verified using Atomic Force Microscopy (AFM) (data is not presented here for brevity).

Simultaneously, a control phage was developed by fusing a non-specific peptide sequence GHLIPLRQPSHQ to the pIII (GHL peptide). This sequence lacks specificity for EGFR or any eukaryotic target [57].

A bead affinity assay was performed to test the ability of the engineered phages to target EGFR (MBE-K012, AcroBiosystem), with concentrations tested ranging from 10^8 to 10^{12}. After the incubation period, samples were subjected to flow cytometry for analysis. For detection, the beads and phages were incubated with an anti-pVIII FITC antibody. $M13_{GHL}$ was used as a negative control, while the SC101 antibody, a commercial monoclonal antibody commonly used to characterise EGFR expression, was used as a benchmark. Data analysis revealed that the $M13_{7D12}$ phage exhibited a high affinity for EGFR with a Kd value of 2.2 nM. In contrast, $M13_{GHL}$ showed no affinity at all. The SC101 antibody presented a Kd of 2.3 nM, this suggest that the modified $M13_{7D12}$ phage's affinity for EGFR is comparable to the monoclonal antibody one, this can be explained because the 7D12 nanobody is displayed in pentavalent display on the five copies of the pIII protein on the tip of the phage.

Notably, the increased affinity is attributed to the specific nanobody display and not a general phage modification or aberration due to the phage’s genome manipulation, as evidenced by the absence of affinity in the $M13_{GHL}$ control phage produced in the same way as the other one but displaying another moiety (Figure 20B).

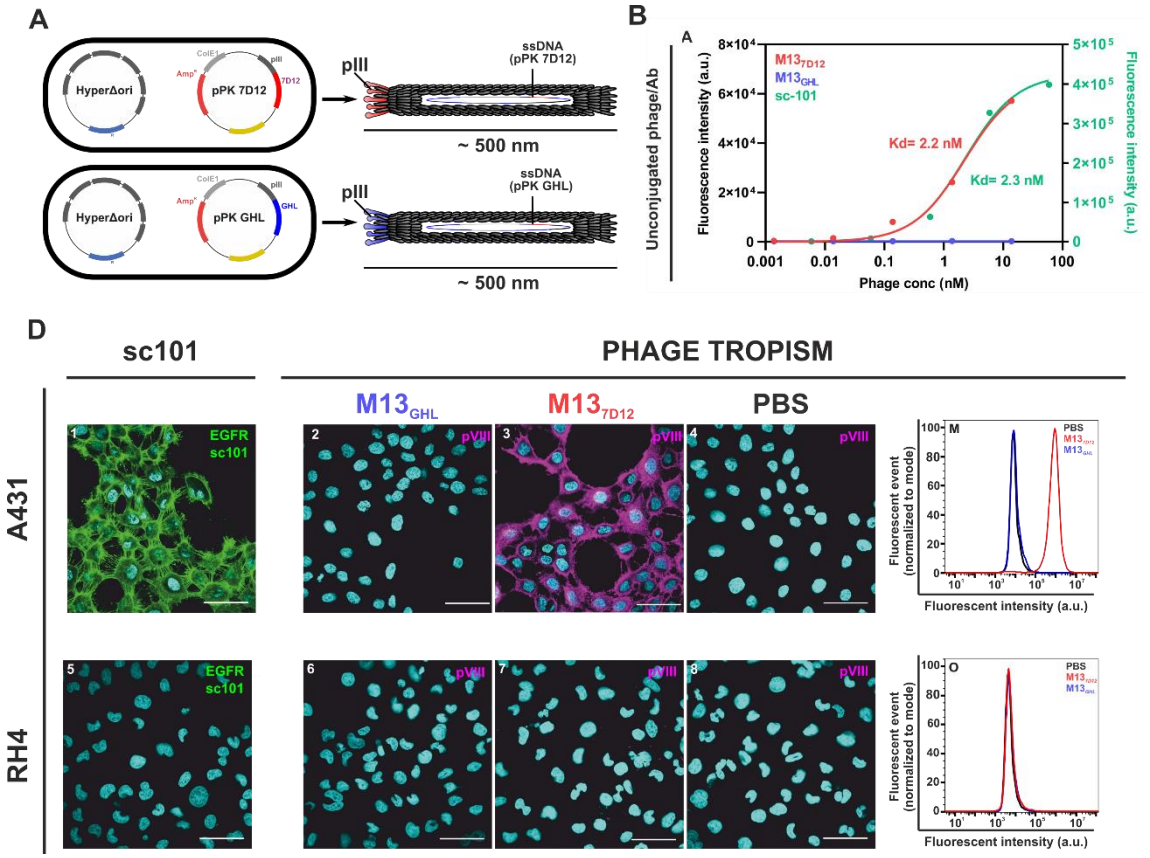

Figure 20 - Phage interactions and tropism analysis. (A) Phage diagrams showing modifications for EGFR targeting via 7D12 nanobody and non-specific peptide display for GHL. (B) Graph showing fluorescence intensity versus phage concentration; SC101 is highlighted as a positive control. (D) Microscopic visualisation of EGFR expression in A431 and RH4 cell lines (in green) using the Sc101 monoclonal antibody. Phage-associated fluorescence is shown in magenta. Adjacent histograms derived from flow cytometry quantify fluorescence intensities for different phage types and controls.

Having established the affinity of $M13_{7D12}$ for EGFR, it was essential to evaluate its ability to target EGFR in a cellular system. Two different cell lines were selected for this purpose: A431, derived from human epidermoid squamous cell carcinoma, known in the literature for its EGFR overexpression, and RH4, derived from human alveolar rhabdomyosarcoma, known for its lack of EGFR expression[58]. To ensure robust results, before evaluating the targeting ability of $M13_{7D12}$, the EGFR expression profiles of both cell lines were determined using immunohistochemistry and confocal microscopy, as detailed in the Methods & Materials (M&M) section, using the monoclonal antibody SC-101. As shown in Figure 20.D, only the A431 cell line showed strong EGFR expression, as evidenced by intense green fluorescence, which was notably absent in the RH4 cell line. Following this characterisation, the phage tropism was assessed by immunohistochemistry as described in M&M. The cell lines were incubated with

$M13_{7D12}$ and $M13_{GHL}$ as a negative control, followed by incubation with an anti-pVIII FITC antibody. No fluorescence was observed in the EGFR-negative RH4 cell line under any condition. In contrast, the EGFR-positive A431 cell line showed strong fluorescence (in purple) only when incubated with the retargeted $M13_{7D12}$ phage. No fluorescence was observed for the negative control ($M13_{GHL}$) or for cells incubated with the secondary anti-pVIII-FITC antibody alone. These observations highlight the enhanced ability of the modified phage to target EGFR in a cellular context.

To further validate these findings, flow cytometry was used as described in M&M. The results were consistent with previous observations. Specifically, for the EGFR-negative RH4 cell line, no discernible peak shift indicative of phage-cell binding was detected for either $M13_{GHL}$ or $M13_{7D12}$, nor for samples treated with the secondary anti-pVIII-FITC antibody alone. Conversely, in the A431 cell line, a significant peak shift encompassing 100% of the cell population was observed exclusively for cells incubated with the $M13_{7D12}$ phage. This confirms the superior targeting efficiency of the engineered phage. No peak shifts were observed in other control conditions.

Following the successful demonstration of the engineered phage's retargeting capabilities, the next objective was to ascertain the potential of this nanovector platform as an effective carrier for molecular delivery to targeted cells. To achieve this goal, the phages were bioconjugated with Rose Bengal (RB), a photosensitizer, as well as with the CF488 fluorophore. Rose Bengal was selected for its dual functionality as a fluorophore and a photosensitizer, ensuring consistent performance in photodynamic therapy (PDT) applications. Meanwhile, CF488 was chosen due to its high efficacy in fluorescence analysis. The RB conjugation was achieved by a coupling reaction in which the carboxylic acid group of the RB was activated, facilitating its interaction with the N-terminus of the M13 capsomers, culminating in the formation of a covalent amidic bond. The CF488A-SE bioconjugate was synthesised by incubation with M13 phage in sodium carbonate buffer as explained in M&M. The bioconjugate was then subjected to a thorough purification process using dialysis, with its purity and concentration confirmed by UV-Vi's spectrometry. The successful bioconjugation was validated by UV-Vis spectroscopic analysis as shown in Figure 21 A and E.

After bioconjugation, the affinity of the phages, $M13_{7D12}$ and $M13_{GHL}$, for EGFR was re-evaluated using the bead affinity assay as before. Pertaining to the CF488 conjugation (Figure 20B), the $M13_{7D12}$ phage retained its affinity, exhibiting a calculated Kd of 2.9 nM. However, for the RB-conjugated phage, while the $M13_{7D12}$ maintained a heightened affinity for EGFR, an off-target effect was also observed for the control phage, as depicted in Figure 20D.

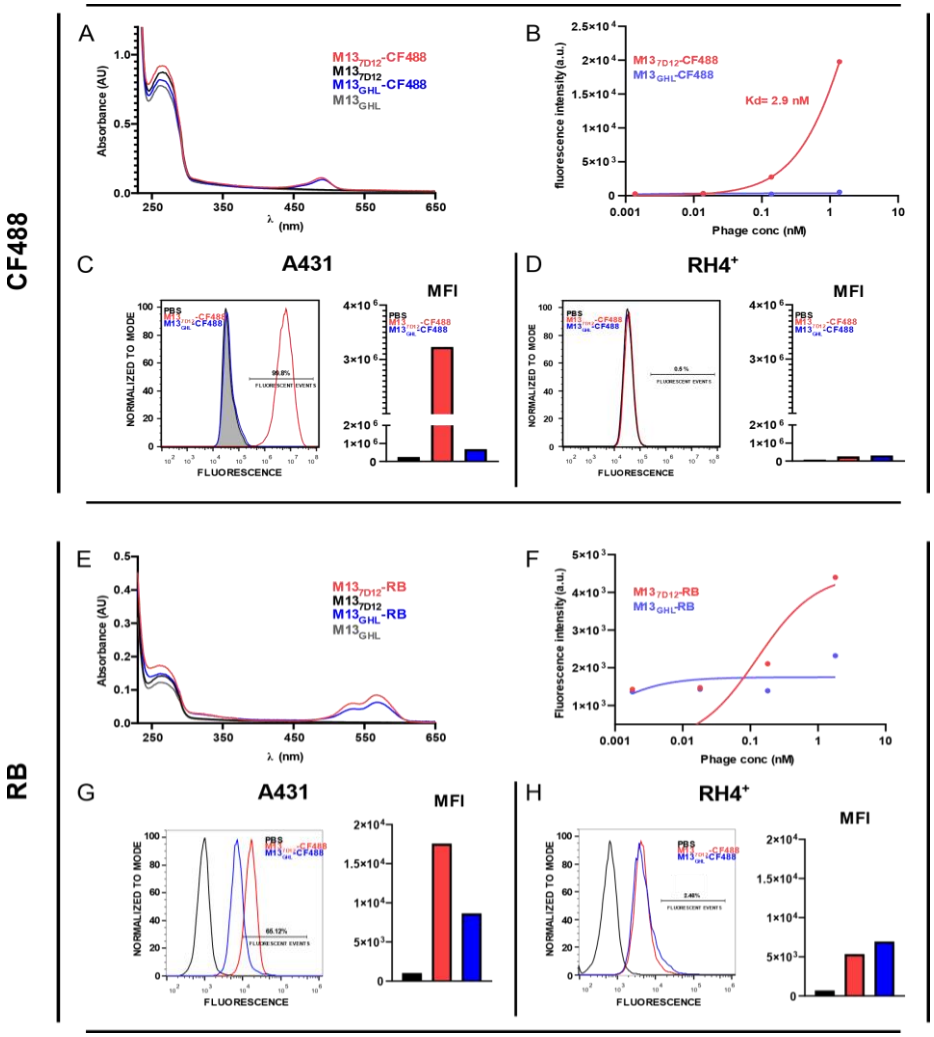

Figure 10 - Analysis of bacteriophage conjugation to CF488 and RB molecules. (A) & (E) UV-VIS spectra showing effective phage conjugation, represented by peak shifts after conjugation with CF488 and RB, respectively. (B) & (F) Interaction analysis of the conjugated phages with EGFR-covered beads, indicating effective target recognition. (C), (D), (G) & (H) Retargeting assays using flow cytometry, highlighting the efficiency of the conjugated phages in recognising their designated targets. Differences in fluorescence intensity between treated (with CF488 or RB) and untreated phages highlight successful conjugation.

These findings were further corroborated in cellular systems. Both cell lines were tested with the conjugated phages via flow cytometry analysis. For the CF488-conjugated samples, a peak shift, indicative of phage binding to A431 cells, was exclusively observed for the $M13_{7D12}$ phage, accounting for 99.8% of the cell

population. No such shift was detected for cells treated with the control phage or PBS. This shift corresponded to a Mean Fluorescence Intensity (MFI) of $3x10^6$, markedly elevated compared to controls. In contrast, the RH4 cell line exhibited no discernible peak shifts, and the calculated MFI was negligible.

For the RB-conjugated phages, an off-target peak shift was observed in the A431 cell line even for the control phage, potentially attributable to residual unconjugated RB molecules in the sample. However, the population shift for cells treated with $M13_{7D12}$ was 65.12% relative to $M13_{GHL}$, and the corresponding MFI was also higher. In the RH4 cell line, the peak shift for $M13_{7D12}$ was 2.46% relative to $M13_{GHL}$, but the $M13_{GHL}$ population exhibited a higher MFI. This variation in peak shifts underscores that, despite the off-target effects potentially linked to residual RB activated, the $M13_{7D12}$-RB conjugate retains its specificity.

Following the successful targeting of EGFR after RB bioconjugation, we sought to evaluate the photodynamic efficacy and killing specificity of the $M13_{7D12}$ phage. To this end, the phage was incubated with the two cell lines, A431 and RH4, at RB-equivalent concentrations of 0.1 and 0.3 μM for 45 minutes. The cells were then washed and irradiated for 20 minutes as described in the Methods and Materials (M&M) section. Control samples were kept in dark, followed by an MTT assay to assess cell viability. Notably, no significant cytotoxic effect was observed under non-irradiated conditions. However, a dose-dependent cytotoxicity was observed upon irradiation. At the 0.3 μM concentration, pronounced cytotoxicity was observed in both cell lines, potentially attributable to an overproduction and saturation of ROS, leading to non-specific effects. Conversely, at the 0.1 μM concentration, the RH4 EGFR-negative cell line exhibited minimal cytotoxicity, with approximately 90% cell viability. In contrast, the A431 EGFR-positive cell line displayed a survival rate of less than 35%, emphasizing the specificity of the cytotoxic effect mediated by the retargeted $M13_{7D12}$ phage. It's noteworthy that this cytotoxic effect was achieved at sub-picomolar concentrations of the engineered phage (Figure 22A).

To further elucidate whether the observed cytotoxicity was a consequence of PDT-induced ROS generation, we employed the ROS-Glo bioluminescence assay (Promega). This assay quantitatively measures intracellular ROS

concentrations. Cells were treated with increasing concentrations of the $M13_{7D12}$ phage, ranging from 0.3 to 1 µM RB equivalents, followed by irradiation. In the absence of irradiation, ROS generation was minimal. However, upon light exposure, a 10-fold increase in ROS production was observed at the highest concentration. These findings unequivocally demonstrate the capability of the bioconjugated system to generate ROS intracellularly, establishing a direct correlation between the observed cytotoxicity and effective ROS generation (Figure 22 B).

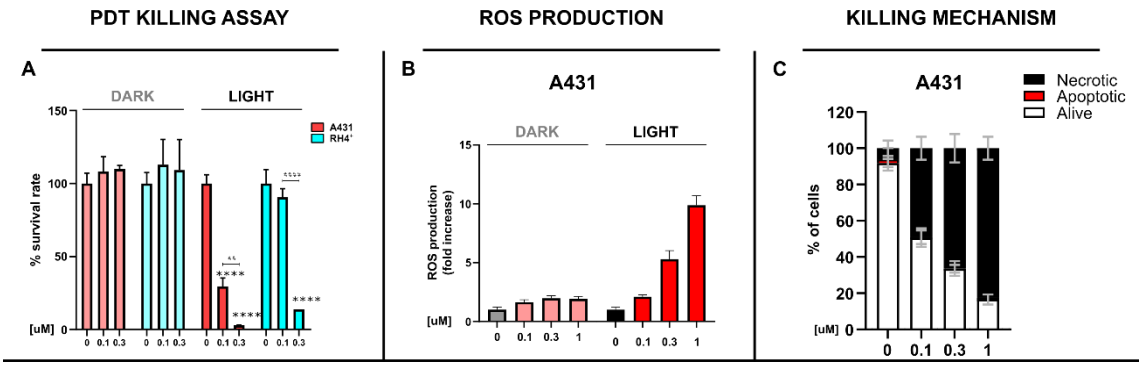

Figure 22 -Assessment of the targeted cytotoxic effects of phage $M13_{7D12}$. (Left) Differential cytotoxicity results in EGFR-positive (A431 in Red) and EGFR-negative (RH4 in cyan) cell lines, assessed after irradiation and in dark condition (dark). (Centre) Detection of ROS production in treated cells using the ROSGlo assay. (Right) Determination of cell death mechanisms after treatment using the Annexin/7-AAD assay.

As previously discussed, while immortalized cell lines serve as foundational models, three-dimensional in vitro models are gaining prominence in pre-in vivo studies due to their capacity to emulate the architecture, biochemistry, and biomechanical intracellular interactions inherent to actual tumor environments. Leveraging this understanding, we cultivated A431 cell spheroids by seeding 500 cells, allowing them to mature as delineated in the Methods & Materials (M&M) section. This was undertaken to evaluate the performance of the bioconjugated nanovector. Five days post-seeding, upon achieving the desired spheroid dimensions and confirming the appropriate 3D structure via bright field microscopy (specific data not presented for conciseness), the spheroids were treated with the $M13_{7D12}$ phage at an RB equivalent concentration of 3µM. While certain spheroids were not irradiated as controls, others underwent a 30-minute irradiation. Subsequent analyses involved visualizing some spheroids using

confocal microscopy and assessing the viability of others employing the 3D CellTiter-Glo reagent, as detailed in M&M.

As depicted in Figure 23A, spheroids treated with PBS and M13$_{7D12}$, but kept in dark conditions, preserved their 3D structural integrity, correlating with elevated cell viability as evidenced by the viability assay. After irradiation, while the PBS-treated spheroids maintained their three-dimensional configuration, those exposed to M13$_{7D12}$ exhibited a pronounced disruption of 3D structural integrity, accompanied by a marked reduction in cell viability. These observations highlight the ability of the engineered phage to infiltrate the three-dimensional spheroid environment. Furthermore, they establish a direct association between the compromised spheroid structure and the cytotoxic effect, underscoring the photodynamic therapeutic potency of the bioengineered nanovector.

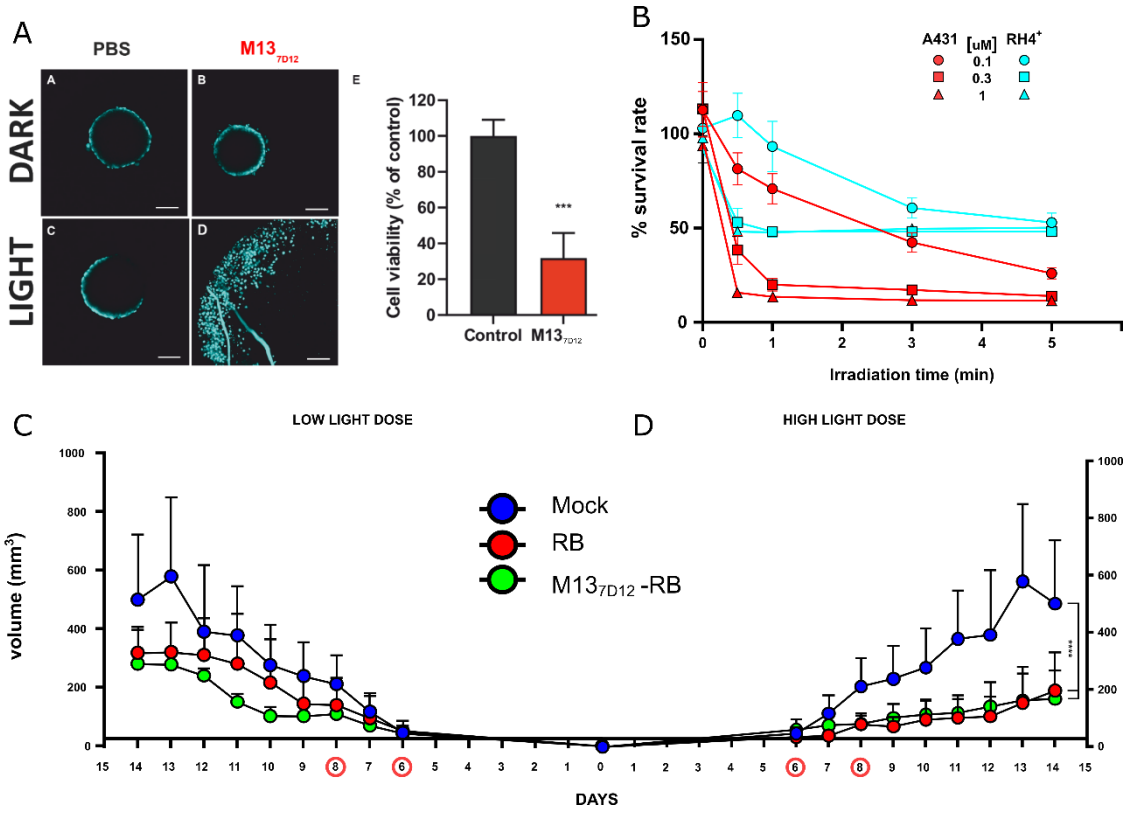

Figure 11 - Evaluation of the therapeutic potential of the retargeted phage M13-$_{7D12}$ (A) Confocal microscopy assessments of spheroids after treatment with PBS (control) and M13$_{7D12}$; top panels (A & B) denote spheroids kept in dark conditions, while bottom panels (C & D) represent irradiated samples. (B) Quantitative analysis of spheroid viability using the CellTiter-Glo 3D assay after treatment, highlighting a significant reduction in viability following M13-7D12 exposure compared to the control. (C) Dose-dependent analysis of cellular responses to different exposure times using an 880-mW laser. (D) In vivo examination of treatment efficacy in mouse models divided into three different groups, each exposed to two different doses of light. Individual data points in the plot symbolise specific treatment responses, with different colours delineating the different experimental cohorts.

To evaluate the potential applicability of the nanovector in a more complex translational in vivo setting, we established a novel irradiation configuration using a 565 nm therapeutic laser with an output of 880 mW [ThorLab. The PDTassay was replicated using increasing concentrations of RB equivalents linked to the phage conjugates and tested in both A431 and RH4 cell lines. We explored a spectrum of irradiation fluency, spanning from 30 seconds to 5 minutes, aiming to discern the optimal time fluency that would elucidate the cytotoxic dynamics of PDT. Notably, irradiation time longer or equal to 1 minute resulted in the comprehensive eradication of A431 cells across all concentrations examined. In contrast, for the EGFR-negative RH4 cell line, non-specific cytotoxicity was observed, affecting only half of the cell population across all concentrations. When exposed for 30 seconds, a clear cytotoxic effect was observed, with the $M13_{7D12}$ phage exhibiting enhanced cytotoxicity against the A431 cell line, reducing viability to below 30% at the highest concentration. Conversely, the RH4 cell line exhibited over 90% viability at the lowest concentration tested, as determined by the MTT assay (Figure 23B). These results highlight the ability of the therapeutic laser to effectively activate the photosensitiser, mirroring the specific cytotoxic results observed in previous PDT assays with reduced light output. Consequently, this irradiation setup holds promise for subsequent in vivo investigations.

To establish an optimised setup for localised tumour irradiation in mice, we used the configuration previously validated for its efficacy in in vitro assays (565 nm therapeutic laser with 880 mW output (ThorLab). Given the potential of this laser setup, we initiated a preliminary in vivo investigation using immunodeficient mice, a model that more accurately simulates tumour growth and response dynamics injected. For this study, mice were divided into three different experimental groups: a mock group, which served as the untreated control; a positive control group administered with RB, to ascertain the efficacy of PDT under the novel irradiation parameters with this in-vivo unused setup; and a third group treated with the bioengineered and conjugated phage $M13_{7D12}$. 1.8 million of A431 cells were injected in both flanks in a final volume of 50 μL. After the bump reached

the treatable dimensions on the 6th day both the RB compound and the bioconjugated $M13_{7D12}$ phage were injected intra-tumourally (IT) at the concentration of 15 μM of RB equivalents. Injection was followed by 45' of incubation and two distinct irradiation sessions of 5 minutes each. Tumor progression was meticulously monitored throughout the day's experimental duration. The study was concluded on the 14th day when three out of the five mice in the mock group died. Notably, none of the mice from the treated groups died.

To elucidate the PDT potential of our phage vector, we subjected the mice to two disparate light doses: a high-intensity light dose and a low-intensity light dose made by the scattering of the light trough the mice bodies. Data from the high intensity light dose regimen showed a clear and significant slowing of tumour growth in irradiated tumours compared to the control group under both RB and $M13_{7D12}$ phage conditions. This data corroborated that the intrinsic PDT potential of the phage vector remains intact, indicating that the conjugation process preserves the inherent efficacy of the sensitizer (Figure 23 C).

Conversely, under the low-intensity light dose regimen, the phage exhibited superior efficacy compared to RB alone. This enhanced performance is likely attributable to the sustained presence and augmented RB concentration mediated by the phage within the tumor environment (Figure 20D). These preliminary in vivo results have important implications for future research efforts. Subsequent studies will focus on intravenous (IV) delivery of the vector to determine if the phage can effectively deliver an increased payload of sensitiser to tumour cells, thereby enhancing therapeutic outcomes.

4. PhagHER2.0 Preliminary Precision in HER2 Targeting

In invasive breast cancer, HER2 (human epidermal growth factor receptor 2) is overexpressed in an estimated 15-30% of cases. This overexpression is often associated with reduced survival in breast cancer patients and, in certain scenarios, with an increased risk of recurrence. Tumours characterised by this aberrant HER2 expression profile tend to be highly resistant to selected

chemotherapeutic agents and hormonal treatments and have an increased rate of cerebral metastases[39]. Given these significant challenges, there is an urgent need to develop innovative therapeutic approaches that can complement and enhance the efficacy of conventional treatments. In alignment with this objective, an M13 phage was bioengineered, employing the methodology delineated in this study, to specifically target HER2. The production of the $M13_{HER2}$ phage involved the integration of a nanobody, designated as 2R15S, with the QVQLQESGGGSVQAGGSLKLTCAASGYIFNSCGMGWYRQSPGRERELVSRI SGDGDTWHKESVKGRFTISQDNVKKTLYLQMNSLKPEDTAVYFCAVCYNLETY WGQGTQVTVSS sequence. This nanobody, as documented in literature, is renowned for its specificity in targeting HER2 [59] and was fused with the pIII protein inherent to the M13 phage. The requisite phagemid for engineering this phage was procured from a gene syntheis service (OfficinaeBio), and its synthesis was facilitated using the HyperΔOriΔpIII Helper plasmid, as elaborated in the Materials and Methods section.

Prior to evaluating the efficacy of the $M13_{HER2}$ phage in targeting HER2, three different cell lines (BT474, MDAMB231 and RH4) were selected based on their documented HER2 expression profiles. HER2 expression levels in these cell lines were assessed by both confocal microscopy and flow cytometry using the sc-33684 antibody as described in M&M. As shown in Figure 24A, the BT474 cell line exhibits strong HER2 expression as demonstrated by immunohistochemical micrographs. This observation is further substantiated by flow cytometry data, which indicates a significant peak shift in the population incubated with the antibody. In contrast, both the MDAMB231 and RH4 cell lines displayed diminished HER2 expression levels. While this reduced expression was not discernible through confocal microscopy, it was evident in flow cytometry analyses. This suggests that the phage's retargeting capability might be less effective in these cell lines.

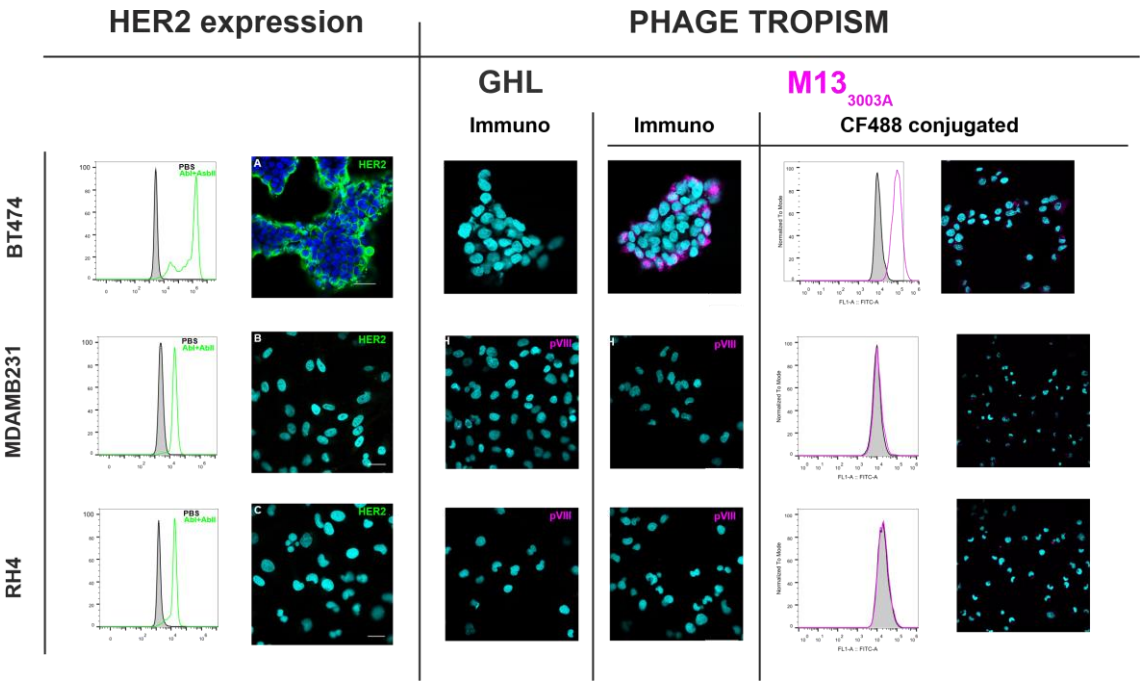

Figure 12 - Integrated Evaluation of HER2 Expression and M13 Phage Affinity Across Cell Lines. The left panels display flow cytometry histograms contrasting PBS controls with cells treated with anti-HER2 antibodies to quantify HER2 expression levels in BT-474, MDA-MB-231, and HCC1954 cell lines. These histograms are juxtaposed with their corresponding confocal microscopy images, identified as A) BT-474, B) MDA-MB-231, and C) HCC1954, illustrating the cellular distribution of HER2. The 'Phage Tropism' section on the right demonstrates the selective binding of M13-3003A phage to HER2-positive cells, as opposed to the non-specific M13GHL phage. The immunofluorescence images, obtained through confocal microscopy, depict anti-pVIII-FITC antibody interaction in magenta. The cells incubated with CF488-tagged M13-3003A phage are analysed using both flow cytometry and confocal microscopy, offering a detailed look at the phage's targeted binding to HER2-expressing cells.

Following the initial characterization, the tropism of the $M13_{HER2}$ phage for HER2 was assessed in the selected cell lines using immunohistochemistry coupled with confocal microscopy. This was juxtaposed against the $M13_{GHL}$ phage, a previously utilized variant that displays the GHLIPLRQPSHQ peptide, which is non-specific for eukaryotic cells, serving as a negative control. As depicted in Figure 24B, fluorescence attributable to the antipVIII-FITC antibody was exclusively observed in the BT474 cell line and solely in samples incubated with the retargeted engineered phage. The absence of significant fluorescence in other samples underscores the engineered phage's specificity in targeting cells with elevated HER2 expression.

To further evaluate the potential of the $M13_{HER2}$ phage as a nanovector for molecular delivery, it was conjugated with the CF488 fluorophore. This bioconjugation process entailed incubating the engineered phage with preactivated CF488 in a sodium carbonate buffer, subsequently followed by purification through dialysis. The successful conjugation was ascertained using UV-Vi's spectroscopy (data omitted for brevity).

Subsequent assays, employing both confocal microscopy and flow cytometry, were conducted on all three cell lines to determine the phage's-maintained ability to target HER2. Notably, for the BT474 cell line, a pronounced fluorescence was observed in samples treated with the $M13_{HER2}$-CF488 phage. This observation was consistent with flow cytometry results, which indicated a significant peak shift relative to samples treated solely with PBS, emphasizing the robust binding of the bioconjugated phage to the cells. In contrast, no discernible fluorescence was detected in the MDAMB231 and RH4 cell lines through confocal microscopy. This observation was consistent with flow cytometry results, which showed no significant shift for these cell lines, thereby reaffirming the engineered phage's specificity in targeting only those cell lines that overexpress HER2.

The comprehensive evaluation of the engineered phage's efficacy across different cell lines, particularly its pronounced specificity for the BT474 cell line, highlights its potential as a targeted therapeutic agent. Moreover, the successful conjugation of the $M13_{HER2}$ phage with the CF488 fluorophore not only emphasizes the versatility of this bioengineered tool but also its potential as a molecular delivery system.

In essence, this research has paved the way for a deeper understanding of targeted therapies in the context of HER2-overexpressing breast neoplasms. The findings underscore the importance of continued exploration in this domain, with the aim of enhancing the efficacy of treatments and improving patient outcomes in the face of complex oncological challenges. Future endeavours should focus on the clinical applicability of the $M13_{HER2}$ phage in PDT and its potential synergistic effects when combined with existing therapeutic regimens.

Conclusions

The research presented explores the innovative potential of the M13 phage as a targeted delivery system for PDT. Central to this research is the molecular engineering of M13 phages to target specific receptors. This was achieved by using targeting peptides, which are short sequences of amino acids known for their affinity to specific cell types or receptors. The use of these targeting peptides represents a significant advance in the field of targeted therapies, allowing a more precise and effective approach compared to traditional methods.
Two different peptides were used to target two different cancers. The first one displayed on the tip of the phage was SYPIPDT, a peptide that targets EGFR, a receptor known for its role in various cancers, a high retargeting capability was obtained with the engineered phage. Following the genetic modifications, the M13 phage was bioconjugated with Rose Bengal (RB), an FDA-approved dye and photosensitizer. Spectroscopic analyses confirmed the successful bioconjugation, and the resultant bioconjugate exhibited an enhanced capability to produce ROS upon light activation. This ROS generation, a cornerstone of PDT's therapeutic mechanism, was significantly amplified by the targeted approach facilitated by the peptides in both cell-free and cell-system. This ability translated also in a high killing efficiency towards A431 cell line, known for the EGFR high expression, after the chemical conjugation with RB. This suggested the effective development of a nanovector that can improve the PDT potency by delivering PS with a high payload on the interested cells.

The developed platform has a high modular capability, on both chemical conjugation of PS or fluorescent molecules and genetic modification to target different cell lines with different expression profiles. This versatility is underlined by the display of another peptide in fusion with the pIII protein of the M13 phage, the CPIEDRPMC peptide, known in literature by its ability to target Colon Cancer cells[60]. The M13$_{CC}$ phage was conjugated with RB and its efficacy was rigorously assessed, revealing pronounced retargeting capabilities, especially towards the HT29 colon cancer cells. This was evident through various techniques, including confocal microscopy and flow cytometry analyses. The photodynamic efficacy of the bioconjugated phage was further highlighted by the

significant cytotoxic effects observed upon photo-irradiation. The heightened sensitivity of the HT29 cells to the phage-mediated PDT underscores the effectiveness of the targeting peptides in guiding the phage to its intended targets. Mechanistic investigations provided insights into the underlying processes. The cytotoxic effects were predominantly attributed to the intracellular production of ROS, which triggers cellular necrosis. A standout observation was the bioconjugated phage's ability to deeply penetrate CC spheroids, a capability not previously documented. This deep penetration, made possible by the targeting peptides and probably the peculiar phage biology and virion shape, suggests the potential of the bioconjugated phage in enhancing PDT efficiency across a more extensive tissue depth.

To amplify the targeting capabilities of the M13 engineered platform, a significant transition was made from the SYPIPDT peptide, which primarily targets EGFR, to the 7D12 nanobody. This nanobody, characterized by its unique sequence, is renowned for its specific affinity to the outer membrane domain of the EGFR. The decision to incorporate the 7D12 nanobody was driven by its potential to offer enhanced specificity in targeting. In parallel, a control phage was developed by integrating a non-specific peptide sequence ($M13_{GHL}$) to the pIII. This sequence was chosen due to its lack of specificity for EGFR or any eukaryotic target. The targeting capabilities of the engineered phages were then tested using a beads affinity assay. The $M13_{7D12}$ phage showcased a high affinity for EGFR, comparable to the SC101 monoclonal antibody when the 7D12 nanobody was correctly displayed. To further validate the targeting capabilities of $M13_{7D12}$, two distinct cell lines, A431 and RH4, were employed. The A431 cell line is known for its EGFR overexpression, while the RH4 cell line is notable for its lack of EGFR expression. Through a series of experiments, including immunohistochemistry and flow cytometry, the $M13_{7D12}$ phage demonstrated a pronounced ability to target EGFR within a cellular context, especially in the A431 cell line. Following these successful demonstrations, the next phase involved evaluating the potential of the $M13_{7D12}$ phage as a carrier for molecular delivery. The phages were bioconjugated with both RB and CF488, and their affinity for EGFR was re-assessed. The results indicated that the $M13_{7D12}$ phage retained its affinity post-bioconjugation outperforming the control phage for specific binding.

Subsequently the photodynamic efficacy of the $M13_{7D12}$ phage was assessed. Experiments revealed that the bioconjugated phage could effectively generate ROS intracellularly, leading to cytotoxic effects, especially in the A431 cell line, this due to a specific necrotic killing effect. Recognizing the limitations of two-dimensional cell cultures, the research then transitioned to three-dimensional in vitro models. A431 cell spheroids were cultivated and treated with the $M13_{7D12}$ phage. The results underscored the phage's ability to infiltrate and disrupt the three-dimensional spheroid environment, emphasizing its potential in a real-world tumor context.

Lastly, preliminary in vivo investigations were conducted using immunodeficient mice. The results from these experiments were promising, with the $M13_{7D12}$ phage demonstrating superior efficacy in slowing tumor growth, especially under a low-intensity light dose regimen. This preliminary in vivo data sets the stage for future research, with a focus on intravenous administration of the vector to further enhance therapeutic outcomes.

The developed nanovector demonstrates exceptional modularity, enabling tailored approaches in targeted therapies. Capitalizing on this feature, we addressed challenges associated with HER2 (Human Epidermal Growth Factor Receptor 2) overexpression, which is observed in 15-30% of invasive breast neoplasms[35]. Such overexpression leads to reduced survival rates, heightened recurrence risk, and resistance to specific treatments. To tackle these challenges, we adapted our nanovector to bioengineer an M13 phage, termed $M13_{HER2}$, specifically targeting HER2. This was achieved by incorporating a nanobody, 2R15S, known for its specificity towards HER2.

For validation, we selected three cell lines, BT474, MDAMB231, and RH4, based on their documented HER2 expression levels. Among these, the BT474 cell line displayed pronounced HER2 expression, while MDAMB231 and RH4 exhibited diminished levels. Experimental results indicated that the $M13_{HER2}$ phage effectively targeted the BT474 cell line, emphasizing its specificity. This targeting capability was further confirmed when the phage was conjugated with the CF488 fluorophore.

Throughout our research, we have successfully developed and characterized phage-based nanovectors, specifically $M13_{EGFR}$, $M13_{CC}$, $M13_{7D12}$ and $M13_{HER2}$ to target EGFR, CC, and HER2 overexpressing cell lines. This achievement underscores the precision and adaptability of our engineered phages in recognizing and binding to distinct cellular markers.

While our in vitro results are promising, the transition to in vivo systems presents a new set of challenges and opportunities. It is imperative to study the behaviour of these phages in a living organism, particularly in terms of immune response and potential off-target effects. The specificity and efficacy observed in controlled settings need to be validated in the complex environment of a living system. As we move forward, we will focus on comprehensive in vivo studies to understand the interactions, safety profile and therapeutic potential of our phage-based nanovectors. By addressing these critical aspects, we aim to pave the way for innovative, targeted treatment modalities that can significantly improve patient outcomes in the face of oncological challenges.

Materials and methods

Phage engineering

- **M13$_{EGFR}$** The nucleotide sequence encoding the SYPIPDT peptide, which targets the EGFR receptor, was synthesized by annealing two oligonucleotides: AD0127 (CATGGCCAGCTATCCGATTCCGGATACCGGTGGCGGTG) and AD0218 (GATCCACCGCCACCGGTATCCGGAATCGGATAGCTGGC). These oligonucleotides were designed to produce NcoI and BamHI overhangs at the 5' and 3' ends of the coding sequence, respectively. Subsequently, this insert was cloned into a pre-digested pSEX81 vector (sourced from ProGen) using the NcoI and BamHI restriction sites, resulting in the creation of the pPK15 phagemid. Following the ligation process, the construct was transformed into *E. coli* (strain TG1). The validity of these ligations was further confirmed through Sanger sequencing of the extracted phagemid DNA. *E. coli* clones that were resistant to ampicillin and harbored the authenticated pPK15 phagemid were then transduced using the Hyperphage helper system (ProGen). This facilitated the multivalent type 3 display of the SYPIPDT-pIII fusion protein on the tip of the phage virion.
- **M13cc**has been genetically engineered to exhibit a specific targeting peptide, CPDIERPMC, which is covalently linked in-frame to the pIII capsid protein. The peptide's coding sequence (CDS) was synthesized by annealing two specific oligonucleotides: AD0186 (CATGGCCTGTCCAATTGAAGATAGGCCTATGTGTGGTGGCGGTG) and AD0187 (GATCCACCGCCACCACACATAGGCCTATCTTCAATTGGACAGGC). These oligonucleotides were designed to produce NcoI and BamHI overhangs at their respective ends. Subsequently, this insert was strategically integrated into the pSex81 vector (sourced from ProGen,

Heidelberg, Germany) that had been linearized using the same restriction enzymes, obtained from New England Biolabs (NEB). The resultant phagemid, termed pPK24, harbors the CPDIERPMC peptide, which is fused in-frame with the pIII CDS. This fusion is preceded by a PelB leader sequence, which facilitates the periplasmic localization and subsequent incorporation of the fusion protein into the virion, as depicted in Figure. 1I. The integrity and authenticity of this phagemid were confirmed through Sanger sequencing and further validated by immunoblotting to ensure the expression of the desired fusion construct. Following the transformation of this construct into *E. coli* TG1, colonies that were positive for the desired trait were identified based on their resistance to ampicillin. These colonies were then superinfected with the Hyperphage helper phage (sourced from ProGen). This step ensured the pentavalent type 3 display of the pIII peptide fusion on the phage's surface.

- **M13$_{7D12}$** The nucleotide sequence encoding the "QVKLEESGGGSVQTGGSLRLTCAASGRTSRSYGMGWFRQAPGKER EFVSGISWRGDSTGYADSVKGRFTISRDNAKNTVDLQMNSLKPEDTAIY YCAAAAGSAWYGTLYEYDYWGQGTQVTVSS" nanobody, which targets the EGFR receptor, was obtained from a synthetic gene. This gene sequence was amplified via PCR using two primers: AD0276 (GTTTTGAGCTCCAGGTTAAATTAGAGGAGTC) and AD0277 (GTTTTACTAGTGCTAGATACCGTCACTTGAGTA). These primers were designed to produce SacI and SpeI overhangs at the 5’ and 3’ ends of the coding sequence, respectively. Subsequently, this sequence was integrated into a pre-digested pComb3XSS vector (Addgene; modified to substitute the PelB leader with a DsbA leader sequence[61]) using the SacI and SpeI restriction sites, resulting in the creation of the pComb3XSS_7D12 phagemid. After the cloning process, the construct was transformed into *E. coli*. The authenticity of this cloning was further confirmed through Sanger sequencing of the extracted phagemid DNA. The *E. coli* clones were then transformed with a helper plasmid "HyperΔori" derivative devoide of the f1 origin, which provides all the other proteins except for the pIII and cannot be packaged as phage DNA.

- **M13$_{HER2}$** The nucleotide sequence encoding the "MEVQLVEKGGGRVQAGGSLRLRCAASGITFSINTMGWYRQAPGKQR ELVALISSIGDTYYADSVKGRFRIRRDNAKNTVYLRMRRLKPEDTAVYYC KRFRTAAQGTDYWGQGTRVTVSK" nanobody, which targets the HER2 receptor, was obtained from a synthetic gene. This gene sequence was amplified via PCR using two primers: AD0259 (gttttGAGCTCatggaagtgcag) and AD0260 (gttttACTAGTtttgctcacggt). These primers were designed to produce NcoI and BamHI overhangs at the 5' and 3' ends of the coding sequence, respectively. Subsequently, this sequence was integrated into a pre-digested pComb3XSS vector (see above) using the NcoI and BamHI restriction sites, resulting in the creation of the pComb3XSS_HER2^{+} phagemid. After the cloning process, the construct was transformed into *E. coli*. The authenticity of this cloning was further confirmed through Sanger sequencing of the extracted phagemid DNA. The E. coli clones were then transformed with the helper plasmid "HyperΔori", which provides all the other proteins except for the pIII and cannot be packaged as phage DNA.

For propagation, the bacteria were cultivated overnight in LB medium, enriched with Ampicillin (100 mg/L), Kanamycin (25 mg/L), and 0.4 mM IPTG. This medium ensured the selection of host cells containing both pPK15 phagemid and the helper phage or the helper plasmid, and simultaneously induced the expression of the pIII fusion protein, driven by the P_{lac} promoter. Following cultivation, the culture underwent centrifugation at 6000g for 30 minutes to segregate the bacterial cells from the phages found in the supernatant. To this supernatant, PEG 8000 (4% w/v) and NaCl (3% w/v) were added. After agitating the mixture for 90 minutes at 4°C, it was centrifuged at 15,000 g for 15 minutes to sediment the M13 virions. These pelleted phages were reconstituted in mQ water and subsequently precipitated by adjusting the pH to the phage's isoelectric point (IEP) using HCl Following the IEP-based purification and precipitation, the phages were reconstituted in 1xPBS (pH 7.2). This methodology was demonstrated to effectively eliminate endotoxins originating from the host bacterial cultures, rendering the phages suitable for subsequent cell culture

experiments[62]. The concentration of the phages was determined by measuring the absorbance at a wavelength of 269 nm using a UV-Vis spectrophotometer, with a known extinction coefficient of ε = 3.84 μM.

Bioconjugation and Purification of $M13_{EGFR}$ Phages

The bioconjugation process of the engineered M13 phages with RB was meticulously executed. Initially, RB was solubilized in DMSO to achieve a 10 mM concentration. Subsequently, 1-Ethyl-3-(3-dimethylaminopropyl) carbodiimide (EDC) and N-hydroxysuccinimide (NHS) were incorporated under continuous stirring to reach final concentrations of 10 mM and 15 mM, respectively. This mixture was subjected to incubation at 25 °C for 3 hours, with a consistent shaking rate of 700 rpm, using a ThermoMixer HC (S8012-0000; STARLAB, Hamburg, Germany), ensuring protection from light. A volume of 50 μl of the activated RB solution was dropwise addedd to 1 ml of a PBS solution enriched with M13 phages at 40 nM concentration, under intense stirring. This was followed by an overnight incubation at 25 °C, maintaining a mild stirring condition of 700 rpm.

For the fluorescent labeling of $M13_{EGFR}$, FITC was dissolved in DMSO to yield a 10 mM concentration. A 50 μl aliquot of this FITC solution was carefully added to 1 ml of a 100 mM sodium carbonate buffer (pH 9) containing M13EGFR phages at 40 nM. The mixture was incubated overnight at 25 °C with continuous shaking at 700 rpm. An identical protocol was employed for the TRITC labeling of M13EGFR phages. To ensure the purity of the conjugated phages, a purification step was performed. This involved dialysis against a 100 mM sodium carbonate buffer (pH 9) using a regenerated cellulose membrane with a 14,000 kDa cut-off. This step was crucial to eliminate unconjugated RB, TRITC, FITC, CF488 and any reaction by-products. The progress of the purification was monitored through UV-Vis spectral analysis of the dialysate at each stage. The final dialysis cycle was conducted against a 10 mM PBS solution at pH 7.4, facilitating the removal of the alkaline buffer.

In the preparation of the CF488A-SE bioconjugate, the following methodology was meticulously adhered to:

Initially, CF488A-SE was solubilized in dimethyl sulfoxide (DMSO) to yield a stock solution with a concentration of 10 mM. Subsequently, 20 µL of this stock solution was meticulously dispensed in a dropwise manner to 1 ml of a sodium carbonate buffer (100 mM, pH 9). This buffer solution contained M13 phages at a concentration of 40 nM. During the addition, the solution was maintained under continuous stirring conditions. Following the addition, the resultant mixture was incubated for a duration of 3 hours at a controlled temperature of 25 °C. The stirring was maintained at a moderate speed of 700 rpm to ensure uniform distribution and interaction of the components. Post-incubation, the bioconjugate was subjected to a purification process. This was achieved through dialysis against phosphate-buffered saline (PBS) using a regenerated cellulose membrane with a molecular weight cut-off of 14 kDa. To monitor the efficiency and progression of the purification, UV-Vis spectral analyses of the dialysate were conducted at each stage. Finally, the quantity of CF488A present in the purified product was ascertained using UV-Vi's spectrometry. The quantification was based on the molar extinction coefficient at its maximum absorbance of 488 nm, which is given by $\varepsilon\_488nm = 70{,}000\ M^{-1}cm^{-1}$.

Atomic Force Microscopy (AFM) Characterization of $M13_{EGFR}$ Phages

The atomic force microscopy (AFM) analysis of M13 phages was conducted using a Multimode 8 AFM system (Bruker, USA). Specimens were prepared by adsorbing fully hydrated phages onto the pristine surface of freshly cleaved muscovite mica, sourced from Electron Microscopy Sciences, USA. A carefully measured aliquot of the phage solution, adjusted for concentration and diluted in PBS buffer, was deposited onto the mica surface, and allowed to adsorb for a duration of 2 minutes. After this, the AFM fluid cell was assembled, and a defined volume of ultrapure water (milliQ, Millipore, USA) was introduced into the cell. The imaging process was executed in the PeakForce Tapping® mode in a liquid environment, utilizing ScanAsyst Fluid+ probes (Bruker, USA).

Post-imaging, the acquired micrographs underwent processing using the NanoScope Analysis software (version 1.80). The primary processing step involved the flattening of the micrographs to ensure clarity and accuracy. For a detailed morphological analysis, the (x, y, z) coordinates outlining the contours of

several hundred individual phages were semi-automatically digitized from the micrographs. This digitization was facilitated by a custom-developed software tool, designed using Matlab (Mathworks, USA)[63], [64].

Immunoblotting Analysis

- **Protein Extraction Procedure**: *E. coli* TG1 cells, transformed with the cloned phagemids, were cultured until they reached an optical density (OD) of 0.4 in Luria-Bertani (LB) medium supplemented with 2% glucose. A 1 mL aliquot of this culture was set aside to evaluate the expression of the non-induced pIII protein. The remaining culture was centrifuged at 5000g for 5 minutes, and the resultant pellet was resuspended in 5 mL of LB medium enriched with 1 mM IPTG. This induced culture was then incubated under shaking conditions for 3 hours at 37 °C. After this, both the uninduced and induced samples were resuspended in 1% SDS, ensuring an equivalent OD of 4.
- **Immunoblotting Procedure**: Both the protein extracts and the purified phages, at a concentration of 10^{10} pfu μL^{-1}, were subjected to electrophoresis on a 12% (w/v) SDS-PAGE gel. The separated proteins were then electrotransferred onto a PVDF membrane (Immobilion-P, Millipore, France). The membrane was subsequently treated with a blocking solution composed of 5% milk in PBS (pH 7.4) with an addition of 0.05% Tween. Following the blocking step, the membrane was incubated with the Anti-M13 pIII Monoclonal Antibody (sourced from New England BioLabs) at a dilution of 1:5000 in the blocking solution, and this was allowed to proceed for 1 hour at ambient temperature. The membrane was then washed thrice with PBS containing 0.05% Tween. For detection, the membrane was incubated with an HRP-conjugated IgG anti-mouse secondary antibody (Jackson) at a dilution of 1:10,000, again for 1 hour at room temperature. Visualization of the proteins was achieved using a detection ECL solution (GVS). The resulting images were captured using the ChemiDoc™ Imaging System (Bio-Rad).

Spectroscopic Characterization of engineered M13 Bioconjugates

For the detailed characterization of the M13 bioconjugates, advanced spectroscopic techniques were employed. Absorption spectra were acquired using the Cary60 UV-Vis spectrophotometer from Agilent Technologies, offering insights into the electronic transitions inherent to the bioconjugates. In parallel, the molecular vibrational characteristics and functional group compositions were elucidated using attenuated total reflectance Fourier transform infrared (ATR-FTIR) spectroscopy with the Nicolet iS10 spectrometer. During the sample preparation phase for ATR-FTIR analysis, a 10 µl aliquot of the bioconjugate solution was methodically placed onto a germanium crystal substrate. This was allowed to dry in a controlled manner, resulting in the formation of a uniform thin film. Each spectral acquisition was comprehensive, encompassing 70 scans at a high resolution of 0.5 cm^{-1}. All data, from collection to analytical interpretation, were processed using the Omnic software suite.

Amplex® red assay

To assess the capability of generating peroxides upon exposure to visible light, the Amplex Red® assay was employed. This assay is predicated on the principle that the colourless and nonfluorescent Amplex Red® reagent undergoes a reaction with peroxides, leading to the formation of the coloured and fluorescent compound, resorufin, in the presence of horseradish peroxidase (HRP) as a catalyst. The quantification of the generated peroxides is determined by contrasting the amount of resorufin produced by samples exposed to irradiation against those of non-irradiated reference samples, which are maintained in dark conditions. To prepare the assay, a 10 µl aliquot of a 50 mM Amplex Red® stock solution in DMSO was introduced to 1 ml of a 50 mM phosphate buffer (pH 7.4), yielding a final concentration of 500 µM. Subsequently, 10 µl of a 0.4 mg ml^−1 HRP solution in PBS was incorporated into the Amplex Red® solution, resulting in the final working solution. Test solutions, encompassing varying concentrations of RB and M13EGFR–RB (ranging from 0 µM to 5 µM) in a 50 mM phosphate

buffer (pH 7.4), were subjected to a 30-minute irradiation using a white LED Valex 30 W lamp, positioned 30 cm away from the sample plate. The irradiation power density was maintained at 2.4 mW cm^2, as verified using a Delta Ohm LP 471 RAD photo-radiometer. Each concentration was tested in triplicate to ensure reproducibility. Post-irradiation, 10 µl of the working solution was added to each sample well, followed by a 30-minute incubation at ambient temperature under dark conditions. The fluorescence emission of the samples was subsequently measured at 590 nm (with an excitation wavelength of 560 nm) using a PerkinElmer EnSpire® Multimode Plate Reader. A calibration curve, established using standard H_2O_2 solutions, facilitated the conversion of the fluorescence readings into the corresponding concentrations of peroxides produced upon irradiation.

- **ABMDMA assay**

To evaluate the generation of singlet oxygen ($^1O_2$) upon irradiation, the compound 9,10-Anthracenediyl-bis(methylene) dimalonic acid (ABMDMA) was employed as a specific $^1O_2$ detector. The underlying mechanism involves the reaction of the disodium salt of ABMDMA with $^1O_2$, resulting in the formation of an endoperoxide. This chemical transformation is manifested as a bleaching of the ABMDMA compound. The extent of $^1O_2$ generation is quantitatively determined by monitoring the decrease in absorbance at 401 nm. Iso-absorbing solutions of both RB and $M13_{EGFR}$–RB were meticulously prepared in deuterated PBS with a pH of 7.4. For the assay, 500 µL of the solutions, containing a concentration of 15 µM RB and 25 µM ABMDMA, were subjected to continuous stirring. These solutions were then exposed to irradiation using a Valex cold white LED lamp, ensuring an irradiance of 2.4 mW cm^{-2} on the cuvette surface, a value confirmed using the Delta Ohm LP 471 RAD photo-radiometer. To ascertain the singlet oxygen quantum yield (ΦΔ), Rose Bengal (RB) was employed as a reference standard, known to have a yield of 0.76 in deuterated PBS. The quantum yield of the sample, $M13_{EGFR}$–RB (denoted as ϕΔS), was computed using the equation: $\phi\Delta S = kS/kR \times \phi\Delta R$. In this equation, 'k' represents the slope of the photodegradation rate of ABMDMA, 'S' denotes the sample ($M13_{EGFR}$–RB), 'R' signifies the reference (RB), and ϕΔR corresponds to the ΦΔ of the reference (RB).

Cell cultures

- **A431** cell line, derived from human epidermal carcinoma, was cultivated under controlled conditions. The growth medium employed was RPMI 1640, enriched with several supplements to ensure optimal cell proliferation and health. Specifically, the medium was fortified with 10% heat-inactivated fetal bovine serum (FBS) to provide essential growth factors. Additionally, to prevent bacterial contamination and support cellular metabolism, 1% penicillin-streptomycin solution at a concentration of 100 U ml^{-1} and 1% L-glutamine at 200 mM were added, respectively. All the supplements were sourced from Euroclone, Italy. The cells were maintained at a temperature of 37 °C within a humidified incubator, which also provided an atmosphere containing 5% CO_2, ensuring an optimal environment for cellular growth and function.

- **RH4** cell line, derived from human alveolar rhabdomyosarcoma and characterized by its EGFR-negative phenotype, was cultivated under specific conditions. The growth medium chosen for this cell line was DMEM, which was supplemented to ensure optimal cellular growth and health. This medium was enhanced with 10% heat-inactivated fetal bovine serum (FBS) to provide the necessary growth factors. To prevent bacterial contamination and to support cellular metabolism, 1% penicillin-streptomycin solution at a concentration of 100 U ml^{-1} and 1% L-glutamine at 200 mM were added, respectively. All these supplements were sourced from Euroclone, Italy. The cells were consistently maintained at a temperature of 37 °C within a humidified incubator, which also provided an atmosphere enriched with 5% CO_2, ensuring an optimal environment for cellular growth and maintenance.

- **HT29 and DLD1** colon cancer cell lines, were procured from the American Type Culture Collection (ATCC, Manassas, VA, USA). The HT29 cell line, known for its mismatch repair (MMR)-proficient characteristics, was

cultivated in McCoy's 5A medium. In contrast, the DLD1 cell line, recognized for its MMR-deficient nature, was grown in RPMI 1640 medium. Both media were supplemented to ensure optimal cellular growth and vitality. Specifically, they were fortified with 10% heat-inactivated fetal bovine serum (FBS), 1% l-glutamine at a concentration of 200 mM, and 1% penicillin/streptomycin solution at 100 U/mL. All these supplements were acquired from Euroclone, Pero, Italy. The cell lines were consistently maintained at a temperature of 37°C within a humidified incubator, ensuring an atmosphere enriched with 5% CO_2 to provide an ideal environment for cellular growth and sustenance.

- **BT474** cell line, derived from human mammary gland tumors and characterized by its overexpression of the HER2/neu membrane receptor, a receptor for the human epidermal growth factor 2, was cultivated under specific conditions. The growth medium chosen for this cell line was RPMI, which was supplemented to ensure optimal cellular growth and health. This medium was enhanced with 10-20% heat-inactivated fetal bovine serum (FBS) to provide the necessary growth factors. To prevent bacterial contamination and to support cellular metabolism, 1% penicillin-streptomycin solution at a concentration of 100 U ml^{-1} and 1% L-glutamine were added, respectively. All these supplements were sourced from Euroclone, Italy. The cells, known for their longer duplication time of approximately 100 hours, were consistently maintained at a temperature of 37 °C within a humidified incubator. This incubator also provided an atmosphere enriched with 5% CO_2, ensuring an optimal environment for cellular growth and maintenance**.**

- **MDA-MB-231** cell line, derived from human mammary gland tumors and characterized by its under-expression of the HER2/neu membrane receptor, was diligently cultivated under specific conditions. The growth medium chosen for this cell line was RPMI, which was supplemented to ensure optimal cellular growth and health. This medium was enhanced with 10% heat-inactivated fetal bovine serum (FBS) to provide the necessary growth factors. To prevent bacterial contamination and to

support cellular metabolism, 1% penicillin-streptomycin solution and 1% L-glutamine were added, respectively. All these supplements were sourced from Euroclone, Italy. The cells were consistently maintained at a temperature of 37 °C within a humidified incubator, which also provided an atmosphere enriched with 5% CO_2, ensuring an optimal environment for cellular growth and maintenance.

EGFR and HER2 expression evaluation

To assess the expression levels of EGFR and HER2 in cells, an immunocytochemistry protocol was employed. Cells were seeded at a density of 1×10^6 cells per well on uncoated coverslips and allowed to grow overnight until they reached approximately 25% confluency. Subsequently, the cells were fixed using a 4% paraformaldehyde (PFA) solution for 15 minutes, ensuring the preservation of cellular structures. This was followed by a permeabilization step using 0.1% Triton for another 15 minutes to facilitate antibody access to intracellular targets. To prevent non-specific antibody binding, cells were blocked using a 2% low-fat milk solution for 45 minutes. For the primary antibody incubation, cells were exposed to the SC101 antibody (to evaluate EGFR expression relevant for A431 and RH4 cell lines) and e2-4001 antibody (to assess HER2 expression) at a concentration of 1:500. This incubation was carried out for 1 hour at room temperature (RT). After thorough washing, cells were then treated with an AlexaFluor488 anti-mouse secondary antibody at a dilution of 1:1000 for another 1 hour at RT. To ensure the removal of unbound secondary antibodies, cells underwent three additional washes.

- **Confocal analysis**: Finally, the nuclei were stained using Hoechst 33342 at a concentration of 1 μg ml^{-1}. Imaging of the stained cells was conducted using a NIKON A1R confocal microscope, and the acquired images were subsequently analysed using the ImageJ software to provide detailed insights into the expression levels of EGFR and HER2.
- **Cytofluorimetry analysis**: Flow cytometric evaluations were conducted utilizing the CytoFLEX S (Beckam Coulter) cell sorter. The cell population

was strategically gated based on forward and side scatter parameters. Fluorescence associated with AlexaFluor488 was detected in the FL1 channel. To quantify the extent of $M13_{EGFR}$–FITC targeted cells in relation to control samples, the median fold-increase in fluorescence was employed as a metric. Each analysis encompassed the evaluation of a minimum of 10,000 events. Comprehensive interpretation of the data was facilitated using the FlowJo™ software.

Engineered phage retargeting evaluation via Immunofluorescence (IF)

The retargeting behaviour of unconjugated phages was thoroughly investigated using immunocytochemistry techniques. Cells were seeded at a density of 1 × 10^6 cells per well on uncoated coverslips and allowed to grow until they reached approximately 25% confluency. Following this, the cells were treated with a complete medium containing either 2×10^{10} engineered phages or M13 phages for a period of 45 minutes. The medium was subsequently discarded, and the cells on the coverslips were rinsed three times with 1× PBS. For fixation, a 4% paraformaldehyde (PFA) solution was applied for 15 minutes, after which the cells were permeabilized using 0.1% Triton for an additional 15 minutes. To block non-specific binding, cells were incubated in a 2% low-fat milk solution for 45 minutes. The specimens were then incubated with a mouse anti-pVIII antibody (sourced from ProGen) at a dilution of 1:300 for 1 hour at room temperature. After washing, they were further incubated with a goat anti-mouse IgG antibody conjugated with both Alexa Fluor®568 and Alexa Fluor®488 (from Invitrogen) at a dilution of 1:1000 for another hour at room temperature. Following three washes to eliminate any unbound antibody, the cells were stained with Hoechst 33342 (from Invitrogen) at a concentration of 1 μg ml^{-1}. Cellular imaging was performed using a NIKON A1R confocal microscope, and the acquired images were subsequently analysed with the ImageJ software for detailed insights.

Engineered phage retargeting evaluation.

- **Flow cytometry**: The retargeting capability of the engineered M13 phages was validated using flow cytometry. All flow cytometric evaluations were

executed using the CytoFLEX S (Beckam Coulter). Phages conjugated with specific molecules were incubated with A431 cells at a ratio of 100:1 for a duration of 30 minutes. Subsequently, the cell population was delineated based on forward and side scatter parameters. The fluorescence resulting from the conjugated molecules was captured in the FL1 channel, utilizing an excitation wavelength of 488 nm and an emission filter set at 525/30 nm. The median fold-increase in fluorescence served as the metric to determine the number of cells targeted by the engineered M13 phages in comparison to control samples. For each sample, a minimum of 10,000 events were analysed. The acquired data were comprehensively processed and interpreted using the FlowJo™ software.

- **Confocal microscopy:** The retargeting capability of the engineered M13 phages was meticulously validated using confocal microscopy. For this purpose, the phages were labelled with TRITC, CF488, RB, or other with appropriate primary and secondary antibodies, and their interaction with the suitable cell line for each specific test was examined using a NIKON A1R confocal microscope. Round coverslips were positioned at the base of a Corning 6-well plate, and 2×10^5 cells per well were seeded, allowing them to grow overnight until they reached approximately 25% confluency. Subsequently, the cells were treated with complete medium enriched with M13 engineered phage conjugated with the respective molecules at a final concentration of 1 μM for a duration of 90 minutes. Post-incubation, cells underwent three washes with PBS and were then stained for 30 minutes using Hoechst 33342 (sourced from Invitrogen) at a final concentration of 1 μg mL^{-1}. The round coverslips were carefully extracted from the 6-well plate and positioned into an Attofluor cell chamber (Invitrogen, USA) containing 1 mL of DMEM without phenol red, supplemented with 10% FBS, 1% Penicillin–Streptomycin, and 1% L-glutamine. Finally, cellular images were captured using the NIKON A1R confocal microscope for detailed analysis.

PDTkilling assays.

Cell lines were seeded in 96-well flat-bottom plates (Corning) and cultivated until they reached approximately 90% confluency. For treatment, cells were exposed to growth medium supplemented with Rose Bengal (RB), the unconjugated engineered phage as controls, and the phage conjugated with RB. This incubation lasted 45 minutes. After this incubation, cells were washed with 1X PBS to remove unattached phage or photosensitizer. They were then irradiated for 30 minutes using a white light LED, achieving an irradiance of 2 mW cm^2 the choice of this duration was inferred from preliminary tests, which indicated a more pronounced cytotoxic effect at 0.1 µM with a 30-minute exposure compared to shorter durations. Other irradiation in vitro test were performed using a 565 nm therapeutic laser with an 880 mW output from ThorLab (ThorLab, USA) for a spectrum of fluency ranging from 30 seconds to 5 minutes of irradiation to teste the translational ability of the nanovector platform. After irradiation, cells were returned to complete medium and incubated for 24 hours at 37°C in a 5% CO_2 environment. Parallel control groups were kept in the dark throughout this period. Cell viability was subsequently assessed using the MTT (3-(4,5-dimethylthiazol-2-yl)-2,5-diphenyltetrazolium bromide) assay from Merck, Darmstadt, Germany.

Cell Viability and Membrane Permeabilization after PDT treatment

Post-PDT cell viability was evaluated using the MTT assay. Following the treatment, the existing culture medium was discarded and replenished with fresh medium containing MTT at a concentration of 0.5 mg mL^{-1}. Cells were then incubated for 90 minutes at 37°C in a 5% CO_2 atmosphere. Subsequently, the MTT-containing medium was removed, and DMSO was introduced to solubilize the formazan crystals. Absorbance readings were taken at wavelengths of 570 nm and 690 nm using the EnSpire multimode plate reader (PerkinElmer, USA). The results presented are the average of at least three independent experiments, with data expressed as mean ± standard deviation. For a more detailed evaluation of cell viability and potential membrane permeabilization due to phage-mediated PDT, a live/dead staining method using Calcein and Propidium Iodide (PI) was employed, specifically on a cell line suitable for the experiment. Cells,

numbering 1 million, were seeded in 6-well plates, each equipped with a 25 mm round coverslip, and allowed to grow until they reached 50% confluency. These cells were then treated with complete medium enriched with the engineered phage conjugated with RB at a concentration of 1 μM. After a 90-minute incubation, cells underwent a triple wash with PBS and were exposed to LED light illumination as previously detailed. At two distinct time points, immediately post-treatment (t1) and 24 hours post-treatment (t2), cells were stained for 15 minutes using 100 nM Calcein AM and 30 nM PI. The stained cells on the coverslips were then prepared in a cell chamber, and imaging was conducted using a NIKON A1R confocal microscope, equipped with the necessary filters.

Killing mechanism assay

To elucidate the cellular death pathways activated by the M13 conjugated engineered phage, cells were subjected to a post-treatment analysis at intervals of 3, 6, and 24 hours. After these durations, cells were thoroughly rinsed and delicately detached using TrypLE, a product of Gibco by Thermo Fisher. For further analysis, cells were then treated with 100 μL of Guava Nexin Reagent, sourced from Luminex, Austin, Texas, USA. This reagent comprises both 7-aminoactinomycin (AAD) and annexin V-phycoerythrin (PE). A 20-minute incubation at ambient temperature in a light-deprived environment followed. Post-incubation, the cellular samples were subjected to flow cytometric analysis utilizing the Guava EasyCyte 6-2L system, a product of Luminex.

Multicellular Spheroid generation

For the consistent and uniform generation of multicellular spheroids, CC cells and A431 cells were cultured utilizing a low adhesion multi-well plate technique, the 96U Bottom Plate from Nunclon Sphera (Thermo Fisher Scientific, Waltham, MA, USA) was employed. A total of 500 cells were dispensed into each well in a volume of 100 μL, facilitated by centrifugation. Following seeding, the plates were incubated at 37°C in a 5% CO_2 environment for a duration of 5 days, allowing the cells to aggregate and form spheroids. To maintain optimal culture conditions,

50% of the medium was refreshed every third day. Precision in liquid handling was ensured using an automated multichannel pipette, operating at a dispensing rate of 10 µL/s, sourced from Gilson, Middleton, WI, USA.

Upon successful formation of the microtissues, the spheroids were carefully transferred to GravityTrap recipient plates, a product of Insphero AG, Schlieren, Switzerland. This facilitated the continuous observation of spheroid growth, viability, and allowed for detailed microscopic analyses. Over a 5-day observation period, the spheroids exhibited steady, exponential, and uniform growth. Drawing from established literature [27], it was noted that the outer layer of the spheroid predominantly contained proliferating cells, while the inner core was characterized by a mix of quiescent living cells and cells undergoing apoptosis.

$M13_{CC}$-RB Cytotoxicity on Tumor Spheroids

To assess the growth and uniformity of spheroids and to conduct an initial evaluation of the potential cytotoxic effects of M13CC-RB on multicellular tumor spheroids, we employed the CyQUANT® cell proliferation assay (Invitrogen, Thermo Fisher) as per the manufacturer's guidelines. Briefly, following a 45-minute incubation with M13CC-RB and a subsequent 30-minute irradiation period, the spheroids were subjected to staining with CyQUANT® GR dye, which had been appropriately diluted to a 400-fold concentration in the 1X cell-lysis buffer supplied with the kit and further diluted 20-fold with distilled water prior to application. It is noteworthy that all solutions were prepared and maintained in a light-protected environment and were used within a few hours of their preparation. Subsequently, the spheroids were subjected to analysis using either the Nikon Eclipse Ti microscope, equipped with a Digital Sight camera DS U3 (Nikon, Tokyo, Japan), or the Nikon A1R confocal microscope (Nikon). This approach allowed for the comprehensive monitoring of spheroid growth, evaluation of their uniformity, and the preliminary assessment of potential cytotoxic effects induced by M13CC-RB, ensuring precise data acquisition for our research.

Peroxide Production by the M13 Bioonjugated Phage during PDT

The ability of the M13 engineered conjugated phage to induce the generation of peroxides under visible light exposure was ascertained using the Amplex® Red (AR) assay in a cell-free environment. The AR compound, inherently nonfluorescent and devoid of colour, undergoes a reaction with peroxides in the presence of horseradish peroxidase (HRP) catalyst. This leads to the formation of resorufin, a fluorescent dye characterized by absorption and emission maxima at 563 nm and 587 nm respectively. Peroxide generation was quantified based on the differential resorufin production between irradiated and non-irradiated samples. A working solution (WS) was crafted by combining 1 mL of 50 mM PBS (pH 7.4), 10 µL of a 50 mM AR solution in DMSO, and 10 µL of an HRP solution (0.4 mg/mL in PBS). Sample solutions were established at varying concentrations, specifically 0, 0.25, 0.5, 1, 2, or 4 µM, of both RB and the M13 engineered conjugated phage in 50 mM PBS. To ensure reproducibility, two parallel 96-well plates were populated with these sample solutions (90 µL), and each concentration was replicated thrice technically. One of these plates underwent a 30-minute irradiation using a white LED lamp (Valex cold white LED, with a noted irradiance of 24 mW/cm^2 on the plate surface, gauged using the Delta Ohm LP 471 RAD photo-radiometer). The counterpart plate was preserved in darkness as a control measure. Post-irradiation, each well across both plates received 10 µL of the WS. Following a subsequent 30-minute incubation in the dark, the fluorescence emission intensity was logged at 590 nm (with an excitation wavelength of 530 nm). For quantitative discernment, a calibration curve was produced using standard H_2O_2 solutions, facilitating the translation of fluorescence readings into specific peroxide concentrations. All fluorescence metrics were obtained utilizing the PerkinElmer EnSpire® Multimode Plate Reader.

In vivo PDT

To assess the in vivo photodynamic therapeutic potential of our engineered phage nanovectors, we conducted an experiment using 15 HsdCpb:NMRI-Foxn1nu nude mice. On day 0, each mouse was bilaterally inoculated with 1.8x10^6 A431 cells to establish tumour implantation. By day 6, the tumours were palpable and had reached a size suitable for treatment initiation.

The mice were then randomly assigned to one of three experimental groups of five animals each: a control group (mock), a group treated with rose bengal alone (RB-treated), and a group treated with the phage rose bengal conjugate (Phage-RB-treated). For the RB-treated and Phage-RB-treated groups, 30 µL of a PBS-based solution containing 15 µM RB or Phage-RB was injected into the tumours on both flanks. This was followed by an incubation period of 45 minutes to allow for adequate drug uptake.

After incubation, tumours were treated with PDT using a 565 nm, 880 mW therapeutic laser (ThorLab, USA). Right flank tumours were exposed to 380 mW cm^{-2} for 5 minutes. Left flank tumours were irradiated for 5 minutes at a lower irradiance calculated indirectly from the diffusion of scattered light through the mouse body. A second treatment with identical settings was performed 50 minutes after the first treatment.

Tumour progression was carefully monitored daily using a digital caliper until three of the five mice in the mock group died.

Statistical Analysis

Data is presented as mean ± SEM from a minimum of three independent trials. For result comparisons, one or two-way ANOVA or t-tests were employed, with subsequent Dunnett or Tukey post-hoc tests. Analyses were conducted using GraphPad InStat version 8.0 (GraphPad Prism, San Diego, CA), and a p-value < 0.05 was deemed statistically significant.

References

[1] L. Ulfo, P. E. Costantini, M. Di Giosia, A. Danielli, and M. Calvaresi, “EGFR-Targeted Photodynamic Therapy,” *Pharmaceutics*, vol. 14, no. 2, 2022, doi: 10.3390/pharmaceutics14020241.

[2] S. S. Lucky, K. C. Soo, and Y. Zhang, “Nanoparticles in photodynamic therapy,” *Chem Rev*, vol. 115, no. 4, pp. 1990–2042, Feb. 2015, doi: 10.1021/CR5004198/ASSET/IMAGES/LARGE/CR-2014-004198_0033.JPEG.

[3] M. M. Kim and A. Darafsheh, “Light Sources and Dosimetry Techniques for Photodynamic Therapy,” *Photochem Photobiol*, vol. 96, no. 2, pp. 280–294, Mar. 2020, doi: 10.1111/PHP.13219.

[4] T. G. St Denis and M. R. Hamblin, “Synthesis, bioanalysis and biodistribution of photosensitizer conjugates for photodynamic therapy,” *Bioanalysis*, vol. 5, no. 9, pp. 1099–1114, May 2013, doi: 10.4155/BIO.13.37.

[5] E. Middha and B. Liu, “Nanoparticles of Organic Electronic Materials for Biomedical Applications,” *ACS Nano*, vol. 14, no. 8, pp. 9228–9242, Aug. 2020, doi: 10.1021/acsnano.0c02651.

[6] D. Antoku *et al.*, “Improvement of Photodynamic Activity of Lipid–Membrane-Incorporated Fullerene Derivative by Combination with a Photo-Antenna Molecule,” *Chemistry – A European Journal*, vol. 24, no. 29, pp. 7335–7339, May 2018, doi: 10.1002/chem.201800674.

[7] M. L. Agazzi, J. E. Durantini, N. S. Gsponer, A. M. Durantini, S. G. Bertolotti, and E. N. Durantini, “Light-Harvesting Antenna and Proton-Activated Photodynamic Effect of a Novel BODIPY−Fullerene C $_{60}$ Dyad as Potential Antimicrobial Agent,” *ChemPhysChem*, vol. 20, no. 9, pp. 1110–1125, May 2019, doi: 10.1002/cphc.201900181.

[8] M. R. Hamblin, “Fullerenes as photosensitizers in photodynamic therapy: pros and cons,” *Photochemical & Photobiological Sciences*, vol. 17, no. 11, pp. 1515–1533, Nov. 2018, doi: 10.1039/c8pp00195b.

[9] J. Xu *et al.*, “All-in-One Theranostic Nanomedicine with Ultrabright Second Near-Infrared Emission for Tumor-Modulated Bioimaging and Chemodynamic/Photodynamic Therapy,” *ACS Nano*, vol. 14, no. 8, pp. 9613–9625, Aug. 2020, doi: 10.1021/acsnano.0c00082.

[10] E. Bassan, A. Gualandi, P. G. Cozzi, and P. Ceroni, “Design of BODIPY dyes as triplet photosensitizers: electronic properties tailored for solar energy conversion, photoredox catalysis and photodynamic therapy,” *Chem Sci*, vol. 12, no. 19, pp. 6607–6628, 2021, doi: 10.1039/D1SC00732G.

[11] M. Lan, S. Zhao, W. Liu, C. Lee, W. Zhang, and P. Wang, “Photosensitizers for Photodynamic Therapy,” *Adv Healthc Mater*, vol. 8, no. 13, Jul. 2019, doi: 10.1002/adhm.201900132.

[12] Y. Yamakoshi *et al.*, “Active Oxygen Species Generated from Photoexcited Fullerene (C_{60}) as Potential Medicines: $O_2^{-\bullet}$ versus $^1O_2$,” *J Am Chem Soc*, vol. 125, no. 42, pp. 12803–12809, Oct. 2003, doi: 10.1021/ja0355574.

[13] P. L. Chu *et al.*, “Vandetanib sensitizes head and neck squamous cell carcinoma to photodynamic therapy through modulation of EGFR-dependent DNA repair and the tumour microenvironment,” *Photodiagnosis Photodyn Ther*, vol. 27, pp. 367–374, Sep. 2019, doi: 10.1016/j.pdpdt.2019.06.008.

[14] A. Ormond and H. Freeman, “Dye Sensitizers for Photodynamic Therapy,” *Materials*, vol. 6, no. 3, pp. 817–840, Mar. 2013, doi: 10.3390/ma6030817.

[15] M. Valko, M. Izakovic, M. Mazur, C. J. Rhodes, and J. Telser, “Role of oxygen radicals in DNA damage and cancer incidence,” *Mol Cell Biochem*, vol. 266, no. 1/2, pp. 37–56, Nov. 2004, doi: 10.1023/B:MCBI.0000049134.69131.89.

[16] W. M. Star, “Light delivery and light dosimetry for photodynamic therapy,” *Lasers Med Sci*, vol. 5, no. 2, pp. 107–113, Jun. 1990, doi: 10.1007/BF02031371.

[17] J. S. Dysart and M. S. Patterson, “Characterization of Photofrin photobleaching for singlet oxygen dose estimation during photodynamic therapy of MLL cells *in vitro*,” *Phys Med Biol*, vol. 50, no. 11, pp. 2597–2616, Jun. 2005, doi: 10.1088/0031-9155/50/11/011.

[18] J. J. Reiners Jr, J. A. Caruso, P. Mathieu, B. Chelladurai, X.-M. Yin, and D. Kessel, “Release of cytochrome c and activation of pro-caspase-9 following lysosomal photodamage involves bid cleavage,” *Cell Death Differ*, vol. 9, no. 9, pp. 934–944, Sep. 2002, doi: 10.1038/sj.cdd.4401048.

[19] M. S. D’Arcy, “Cell death: a review of the major forms of apoptosis, necrosis and autophagy,” *Cell Biol Int*, vol. 43, no. 6, pp. 582–592, Jun. 2019, doi: 10.1002/cbin.11137.

[20] R. R. Allison and K. Moghissi, “Photodynamic Therapy (PDT): PDT Mechanisms,” *Clin Endosc*, vol. 46, no. 1, p. 24, 2013, doi: 10.5946/ce.2013.46.1.24.

[21] H. Shi and P. J. Sadler, “How promising is phototherapy for cancer?,” *Br J Cancer*, vol. 123, no. 6, pp. 871–873, Sep. 2020, doi: 10.1038/s41416-020-0926-3.

[22] A. P. Thomas, L. Palanikumar, M. T. Jeena, K. Kim, and J.-H. Ryu, “Cancer-mitochondria-targeted photodynamic therapy with supramolecular assembly of HA and a water soluble NIR cyanine dye,” *Chem Sci*, vol. 8, no. 12, pp. 8351–8356, 2017, doi: 10.1039/C7SC03169F.

[23] E. F. F. da Silva *et al.*, “Intracellular singlet oxygen photosensitizers: on the road to solving the problems of sensitizer degradation,

bleaching and relocalization," *Integrative Biology*, vol. 8, no. 2, pp. 177–193, Feb. 2016, doi: 10.1039/c5ib00295h.

[24] M. Richter and H. Zhang, "Receptor-Targeted Cancer Therapy," *DNA Cell Biol*, vol. 24, no. 5, pp. 271–282, May 2005, doi: 10.1089/dna.2005.24.271.

[25] N. E. Hynes and H. A. Lane, "ERBB receptors and cancer: the complexity of targeted inhibitors," *Nat Rev Cancer*, vol. 5, no. 5, pp. 341–354, May 2005, doi: 10.1038/nrc1609.

[26] R. I. Nicholson, J. M. W. Gee, and M. E. Harper, "EGFR and cancer prognosis," *Eur J Cancer*, vol. 37, pp. 9–15, Sep. 2001, doi: 10.1016/S0959-8049(01)00231-3.

[27] M. L. Martin-Fernandez, D. T. Clarke, S. K. Roberts, L. C. Zanetti-Domingues, and F. L. Gervasio, "Structure and Dynamics of the EGF Receptor as Revealed by Experiments and Simulations and Its Relevance to Non-Small Cell Lung Cancer," *Cells*, vol. 8, no. 4, p. 316, Apr. 2019, doi: 10.3390/cells8040316.

[28] J. P. Dawson, M. B. Berger, C.-C. Lin, J. Schlessinger, M. A. Lemmon, and K. M. Ferguson, "Epidermal Growth Factor Receptor Dimerization and Activation Require Ligand-Induced Conformational Changes in the Dimer Interface," *Mol Cell Biol*, vol. 25, no. 17, pp. 7734–7742, Sep. 2005, doi: 10.1128/MCB.25.17.7734-7742.2005.

[29] M. A. Lemmon, J. Schlessinger, and K. M. Ferguson, "The EGFR Family: Not So Prototypical Receptor Tyrosine Kinases," *Cold Spring Harb Perspect Biol*, vol. 6, no. 4, pp. a020768–a020768, Apr. 2014, doi: 10.1101/cshperspect.a020768.

[30] T. Soldati and M. Schliwa, "Powering membrane traffic in endocytosis and recycling," *Nat Rev Mol Cell Biol*, vol. 7, no. 12, pp. 897–908, Dec. 2006, doi: 10.1038/nrm2060.

[31] G. Liccardi, J. A. Hartley, and D. Hochhauser, "EGFR Nuclear Translocation Modulates DNA Repair following Cisplatin and Ionizing Radiation Treatment," *Cancer Res*, vol. 71, no. 3, pp. 1103–1114, Feb. 2011, doi: 10.1158/0008-5472.CAN-10-2384.

[32] W. Xia *et al.*, "Nuclear expression of epidermal growth factor receptor is a novel prognostic value in patients with ovarian cancer," *Mol Carcinog*, vol. 48, no. 7, pp. 610–617, Jul. 2009, doi: 10.1002/mc.20504.

[33] S. Akkın, G. Varan, and E. Bilensoy, "A Review on Cancer Immunotherapy and Applications of Nanotechnology to Chemoimmunotherapy of Different Cancers," *Molecules*, vol. 26, no. 11, p. 3382, Jun. 2021, doi: 10.3390/molecules26113382.

[34] N. Iqbal and N. Iqbal, "Human Epidermal Growth Factor Receptor 2 (HER2) in Cancers: Overexpression and Therapeutic Implications," *Mol Biol Int*, vol. 2014, pp. 1–9, Sep. 2014, doi: 10.1155/2014/852748.

[35] S. Ménard, S. M. Pupa, M. Campiglio, and E. Tagliabue, “Biologic and therapeutic role of HER2 in cancer,” *Oncogene*, vol. 22, no. 42, pp. 6570–6578, Sep. 2003, doi: 10.1038/sj.onc.1206779.

[36] R. Nahta, L. X. H. Yuan, B. Zhang, R. Kobayashi, and F. J. Esteva, “Insulin-like Growth Factor-I Receptor/Human Epidermal Growth Factor Receptor 2 Heterodimerization Contributes to Trastuzumab Resistance of Breast Cancer Cells,” *Cancer Res*, vol. 65, no. 23, pp. 11118–11128, Dec. 2005, doi: 10.1158/0008-5472.CAN-04-3841.

[37] W. J. Muller, E. Sinn, P. K. Pattengale, R. Wallace, and P. Leder, “Single-step induction of mammary adenocarcinoma in transgenic mice bearing the activated c-neu oncogene,” *Cell*, vol. 54, no. 1, pp. 105–115, Jul. 1988, doi: 10.1016/0092-8674(88)90184-5.

[38] M. Scaltriti *et al.*, “Expression of p95HER2, a Truncated Form of the HER2 Receptor, and Response to Anti-HER2 Therapies in Breast Cancer,” *JNCI Journal of the National Cancer Institute*, vol. 99, no. 8, pp. 628–638, Apr. 2007, doi: 10.1093/jnci/djk134.

[39] M. A. Molina *et al.*, “NH 2-terminal Truncated HER-2 Protein but not Full-Length Receptor Is Associated with Nodal Metastasis in Human Breast Cancer 1”, Accessed: Oct. 26, 2023. [Online]. Available: http://aacrjournals.org/clincancerres/article-pdf/8/2/347/2081625/df0202000347.pdf?casa_token=QAmM4cTAt5gAAAAA:k-zboY1FjQ9-3x5CH3D0vNia3PJWTtBx2b6p5kezgJHjyRGEgo8mKoc816KVVidbWp1WaA

[40] D. J. Slamon *et al.*, “Use of Chemotherapy plus a Monoclonal Antibody against HER2 for Metastatic Breast Cancer That Overexpresses HER2,” *New England Journal of Medicine*, vol. 344, no. 11, pp. 783–792, Mar. 2001, doi: 10.1056/NEJM200103153441101.

[41] E. C. Keen, “A century of phage research: Bacteriophages and the shaping of modern biology,” *BioEssays*, vol. 37, no. 1, pp. 6–9, Jan. 2015, doi: 10.1002/bies.201400152.

[42] B. Loh, V. S. Gondil, P. Manohar, F. M. Khan, H. Yang, and S. Leptihn, “Encapsulation and Delivery of Therapeutic Phages,” *Appl Environ Microbiol*, vol. 87, no. 5, Feb. 2021, doi: 10.1128/AEM.01979-20.

[43] G. Guihard, P. Boulanger, H. Bbnbdettis, R. Lloubbss, M. Besnard, and L. Letellierl, “THE JOURNAL OF BIOLOGICAL CHEMISTRY Colicin A and the To1 Proteins Involved in Its Translocation Are Preferentially Located in the Contact Sites between the Inner and Outer Membranes of Escherichia coli Cells*,” vol. 269, no. 8, pp. 5874–5880, 1994.

[44] I. Stengele, P. Bross, X. Garces, J. Giray, and I. Rasched, “Dissection of functional domains in phage fd adsorption protein,” *J Mol Biol*, vol. 212, no. 1, pp. 143–149, Mar. 1990, doi: 10.1016/0022-2836(90)90311-9.

[45] K. Arnold, L. Bordoli, J. Kopp, and T. Schwede, “The SWISS-MODEL workspace: a web-based environment for protein structure homology modelling,” *Bioinformatics*, vol. 22, no. 2, pp. 195–201, Jan. 2006, doi: 10.1093/BIOINFORMATICS/BTI770.

[46] G. P. Smith and J. K. Scott, “[15] Libraries of peptides and proteins displayed on filamentous phage,” 1993, pp. 228–257. doi: 10.1016/0076-6879(93)17065-D.

[47] K. T. O’Neil and R. H. Hoess, “Phage display: protein engineering by directed evolution,” *Curr Opin Struct Biol*, vol. 5, no. 4, pp. 443–449, Aug. 1995, doi: 10.1016/0959-440X(95)80027-1.

[48] R. Chakravarty, S. Goel, and W. Cai, “Nanobody: The ‘Magic Bullet’ for Molecular Imaging?,” *Theranostics*, vol. 4, no. 4, pp. 386–398, 2014, doi: 10.7150/thno.8006.

[49] S. Steeland, R. E. Vandenbroucke, and C. Libert, “Nanobodies as therapeutics: big opportunities for small antibodies,” *Drug Discov Today*, vol. 21, no. 7, 2016, doi: 10.1016/j.drudis.2016.04.003.

[50] M. Hamzeh-Mivehroud, A. Mahmoudpour, and S. Dastmalchi, “Identification of New Peptide Ligands for Epidermal Growth Factor Receptor Using Phage Display and Computationally Modeling their Mode of Binding,” *Chem Biol Drug Des*, vol. 79, no. 3, pp. 246–259, Mar. 2012, doi: 10.1111/j.1747-0285.2011.01282.x.

[51] L. Ulfo *et al.*, “Orthogonal nanoarchitectonics of M13 phage for receptor targeted anticancer photodynamic therapy,” *Nanoscale*, vol. 14, no. 3, 2022, doi: 10.1039/d1nr06053h.

[52] B. Bortot *et al.*, “Advanced photodynamic therapy with an engineered M13 phage targeting EGFR: Mitochondrial localization and autophagy induction in ovarian cancer cell lines,” *Free Radic Biol Med*, vol. 179, 2022, doi: 10.1016/j.freeradbiomed.2021.11.019.

[53] S. Demartis, A. Obinu, E. Gavini, P. Giunchedi, G. Rassu, and P. Program, “Nanotechnology-based rose Bengal: A broad-spectrum biomedical tool,” *Dyes and Pigments*, vol. 188, p. 109236, 2021, doi: 10.1016/j.dyepig.2021.109236.

[54] A. Cantelli, F. Piro, P. Pecchini, M. Di Giosia, A. Danielli, and M. Calvaresi, “Concanavalin A-Rose Bengal bioconjugate for targeted Gram-negative antimicrobial photodynamic therapy,” *J Photochem Photobiol B*, vol. 206, p. 111852, May 2020, doi: 10.1016/J.JPHOTOBIOL.2020.111852.

[55] H. Huh, S. Wong, J. St Jean, and R. Slavcev, “Bacteriophage interactions with mammalian tissue: Therapeutic applications,” 2019, doi: 10.1016/j.addr.2019.01.003.

[56] R. Heukers, P. M. van Bergen en Henegouwen, and S. Oliveira, “Nanobody-photosensitizer conjugates for targeted photodynamic therapy,” 2014, doi: 10.1016/j.nano.2013.12.007.

[57] U. B. Rasmussen, V. Schreiber, H. Schultz, F. Mischler, and K. Schughart, “Tumor cell-targeting by phage-displayed peptides,”

Cancer Gene Ther, vol. 9, no. 7, pp. 606–612, Jul. 2002, doi: 10.1038/sj.cgt.7700476.

[58] A. R. P. Hinson, R. Jones, L. E. Lisa, B. C. Belyea, F. G. Barr, and C. M. Linardic, “Human Rhabdomyosarcoma Cell Lines for Rhabdomyosarcoma Research: Utility and Pitfalls,” *Front Oncol*, vol. 3, 2013, doi: 10.3389/FONC.2013.00183.

[59] M. D’Huyvetter *et al.*, “Targeted Radionuclide Therapy with A ^{177} Lu-labeled Anti-HER2 Nanobody,” *Theranostics*, vol. 4, no. 7, pp. 708–720, 2014, doi: 10.7150/thno.8156.

[60] K. A. Kelly and D. A. Jones, “Isolation of a Colon Tumor Specific Binding Peptide Using Phage Display Selection,” 2003, Accessed: Oct. 26, 2023. [Online]. Available: www.neoplasia.com

[61] C. F. Schierle, M. Berkmen, D. Huber, C. Kumamoto, D. Boyd, and J. Beckwith, “The DsbA Signal Sequence Directs Efficient, Cotranslational Export of Passenger Proteins to the Escherichia coli Periplasm via the Signal Recognition Particle Pathway,” *J Bacteriol*, vol. 185, no. 19, pp. 5706–5713, 2003, doi: 10.1128/JB.185.19.5706-5713.2003.

[62] P. Passaretti, I. Khan, T. R. Dafforn, and P. Goldberg Oppenheimer, “Improvements in the production of purified M13 bacteriophage bio-nanoparticle,” *Scientific Reports* |, vol. 10, p. 18538, 123AD, doi: 10.1038/s41598-020-75205-3.

[63] G. Zuccheri, A. Scipioni, V. Cavaliere, G. Gargiulo, P. De Santis, and B. Samorı`, “Mapping the intrinsic curvature and flexibility along the DNA chain”, Accessed: Oct. 26, 2023. [Online]. Available: www.pnas.orgcgidoi10.1073pnas.051631198

[64] B. Sampaolese, A. Bergia, A. Scipioni, G. Zuccheri, M. Savino, and B. Samorı`, “Recognition of the DNA sequence by an inorganic crystal surface”, Accessed: Oct. 26, 2023. [Online]. Available: https://www.pnas.org